SMC Bulletin

A Publication of the Society for Materials Chemistry

SOCIETY FOR MATERIALS CHEMISTRY

Society for Materials Chemistry

Society for Materials Chemistry was mooted in 2007 with following aims and objectives:

(a) to help the advancement, dissemination and application of the knowledge in the field of materials chemistry,

(b) to promote active interaction among all material scientists, bodies, institutions and industries interested in achieving the advancement, dissemination and application of the knowledge of materials chemistry,

(c) to disseminate information in the field of materials chemistry by publication of bulletins, reports, newsletters, journals.

(d) to provide a common platform to young researchers and active scientists by arranging seminars, lectures, workshops, conferences on current research topics in the area of materials chemistry,

(e) to provide financial and other assistance to needy deserving researchers for participation to present their work in symposia, conference, etc.

(f) to provide an incentive by way of cash awards to researchers for best thesis, best paper published in journal/national/international conferences for the advancement of materials chemistry,

(g) to undertake and execute all other acts as mentioned in the constitution of SMC.

Executive Committee

President
Dr. V. K. Jain
Bhabha Atomic Research Centre
Trombay, Mumbai, 400 085
jainvk@barc.gov.in

Vice-Presidents
Dr. A. K. Tyagi
Bhabha Atomic Research Centre
Trombay, Mumbai, 400 085
aktyagi@barc.gov.in

Dr. C. S. Sundar
J.C. Bose Fellow & Sr. Professor, HBNI
Materials Science Group
Indira Gandhi Centre for Atomic
Research, Kalpakkam, 603102
css@igcar.gov.in

Secretary
Dr. P. A. Hassan
Bhabha Atomic Research Centre
Trombay, Mumbai, 400 085
hassan@barc.gov.in

Treasurer
Dr. Sandeep Nigam
Bhabha Atomic Research Centre
Trombay, Mumbai, 400 085
snigam@barc.gov.in

Members
Dr. K. C. Barick
Bhabha Atomic Research Centre
Trombay, Mumbai-400085

Dr. S. Kannan
Bhabha Atomic Research Centre
Trombay, Mumbai-400085

Shri. R. K. Mishra
Bhabha Atomic Research Centre
Trombay, Mumbai-400085

Dr. Ratikant Mishra
Bhabha Atomic Research Centre
Trombay, Mumbai-400085

Dr. G. Mugesh
Indian Institute of Science, Bangalore-560012

Dr. (Smt.) Mrinal Pai
Bhabha Atomic Research Centre
Trombay, Mumbai-400085

Dr. Vivek Polshettiwar
Tata Institute Atomic Research Centre
Colaba, Mumbai-400005

Dr. S. K. Sarkar
Raja Ramanna Fellow, Bhabha Atomic
Research Centre, Trombay, Mumbai-400085

Dr. A. K. Tripathi
Bhabha Atomic Research Centre
Trombay, Mumbai-400085

Dr. R. K. Vatsa
Bhabha Atomic Research Centre
Trombay, Mumbai-400085

Dr. V. Venugopal
Raja Ramanna Fellow
Bhabha Atomic Research Centre
Trombay, Mumbai-400085

Co-opted Members
Prof. Anshu Dandia
University of Rajasthan
Jaipur-302004

Dr. D. Das
Raja Ramanna Fellow
Bhabha Atomic Research Centre
Trombay, Mumbai-400085

Prof. A. K. Ganguli
Institute of Nano Science and Technology
Mohali, Punjab - 160062

Dr. K. M. Parida
Institute of Technical Education &
Research Siksha 'O' Anusandhan
University Bhubaneswar-751030

Dr. V. Sudarsan
Bhabha Atomic Research Centre
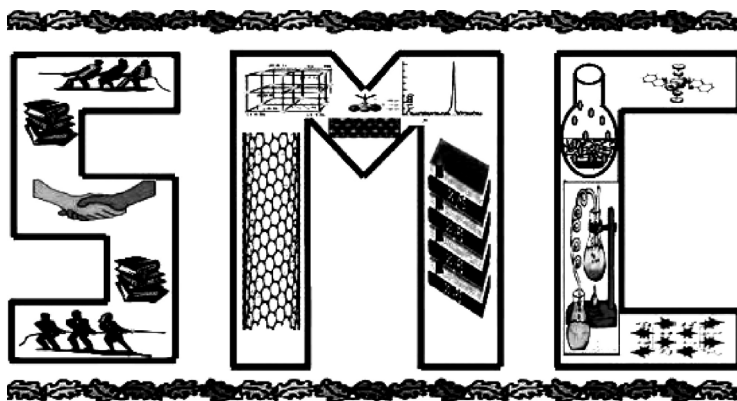Trombay, Mumbai-400085

SMC Bulletin

A Publication of the Society for Materials Chemistry

Volume 8   No. 1   April 2017

SOCIETY FOR MATERIALS CHEMISTRY

SMC Bulletin

Please note that the authors of the paper are alone responsible for the technical contents of papers and references cited therein.
Front cover shows FESEM images of indium sulphide nanoparticles synthesized using different ionic liquids.

Editorial Note

This issue of SMC bulletin includes five articles dealing with (a) material processing by lasers for variety of applications like cutting, drilling, welding, marking, engraving etc., (b) synthesis of energy efficient materials using ionic liquids, (c) sugar based gel chemistry, (d) physicochemical processes in Dye sensitized solar cell and photoelectrochemical solar cells and (e) unique non-Debye relaxation processes.

We hope that readers, especially SMC members will find the articles informative and useful. SMC members are again invited to submit their research work in the bulletin.

Editors

From the desks of the President and Secretary
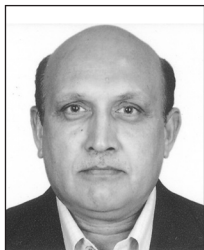
Dr. V.K. Jain
President

Dr. P. A. Hassan
Secretary

Dear Colleagues,

Greetings from the Executive Council of Society for Materials Chemistry (SMC).

We are happy to let you know that SMC has taken the lead in co-organising the Symposium on Selenium Chemistry and Biology, during November 9-11, 2017. The event was held at DAE Convention Centre, Anushaktinagar, Mumbai. Dr. Ratan Kumar Sinha, DAE Homi Bhabha Chair Professor and Former Chariman, Atomic Energy Comission and Secretary DAE delivered the inaugural address. The Symposium was attended by a large number delegates from India and abroad. We are gearing for the National Workshop on Materials Chemistry (NWMC-2017) to be held during December 15-16, 2017 at MU-DAE Centre for Excellence in Basic Sciences, University of Mumbai.

SMC has been regularly publishing invited articles in SMC Bulletin, under different themes of national and international importance. To strengthen the dissemination of knowledge in frontier areas of materials chemistry, for the first time SMC Bulletin has been made open to submissions from all researchers in materials science. We are bringing out the first such series though this bulletin. In this issue, we bring together a compilation of articles in diverse fields ranging from materials processing to low molecular weight gelators, novel solvents, impedance and dielectric spectroscopy.

The advancement in laser based methods for production/ processing of materials and its applications in biology has been reviewed in the lead article by Dr. S. K. Sarkar. The advent of ionic liquids as a green alternative to conventional solvents and its emergence as a powerful media for materials production has been reviewed. The rationale design of sugar based organogelators through non-covalent interactions has been demonstrated. The importance of impedance spectroscopy in identifying the structure-property relationship in dye sensitised solar cells and photo electrochemical materials were also discussed. The role of dielectric spectroscopy in identifying structural relaxation in polymeric materials and other condensed matter systems have been reviewed. Overall, this compilation provides an excellent collection of articles highlighting recent advances in materials science and characterisation. We thank all authors for their sincere efforts towards contributing to SMC Bulletin. We are grateful to the Editorial Staff and Reviewers for their timely input.

We extend our sincere gratitude to all our members of the society for their continued cooperation and active participation in SMC activities. We urge all members to submit their recent research articles to SMC Bulletin.

CONTENTS

Material Processing by Laser: Shifting Landscape

Sisir K. Sarkar

National Centre for Free Radical Research, Department of Chemistry,
Savitribai Phule Pune University, Pune-411007
E-mail: sarkarsk@barc.gov.in / sisirchhaya@gmail.com

Abstract

The laser is a central technology within photonics having great economic impact. Laser material processing has blossomed into a full-scale discipline and interest is growing at an amazing rate. The successful application of laser material processing relies on proper choice of the laser system as well as on a good understanding of the science behind the process. The present article is conceptual and exemplary in nature and not meant as a wide coverage review. In this we first explore some conventional segments of the industry, namely lasers in cutting, drilling, marking, engraving etc. Then follow it up with further developments, such as laser shock peening, laser forming, and laser surface treatment. In recent times the market is witnessing a paradigm shift buoyed by advances in additive materials deposition, the proliferation of laser annealing for thin films, and the evolution of 3D printing for rapid prototyping. The advent of ultrashort lasers and their commercial availability has opened up novel applications in processing industry. Finally moving from materials to live tissues we present a flavor of how the laser technology has revolutionized the biological and medical applications as well. In brief laser material processing have become indispensable engineering solutions for a large number of applications. High initial capital cost was one of the major obstacles in choosing the laser material processing. However, the appearance of new applications and markets for lasers has created strong incentives for further investment in innovation in lasers. All of this feedback and self-reinforcing dynamics are classic features of general-purpose technologies.

1. Introduction

In 1917 a theoretical foundation for a multibillion dollar industry was made. A paper on the theory of quantum and radiation, written by Albert Einstein an effect was described, which is now known as stimulated emission of radiation. This process is the origin of laser light and even is included in the name of the laser itself because LASER is an acronym of the following expression: Light Amplification by Stimulated Emission of Radiation.

It took further 43 years to realize the theoretical know how when the first laser was "born" on May 16, 1960. Theodore H. Maiman, a physicist at Hughes Research Laboratories, USA constructed the first laser with a ruby crystal, producing red light pulses at 693.4 nm. In 1967 the first industrial applications appeared, drilling a hole into diamond with a ruby laser and cutting 1 mm thick stainless steel with a 300W CO_2 laser. The drilling process into diamond with 4.7 mm in diameter and 2mm in deep was carried out in 15 minutes, which was a great improvement at that time because a typical application took about 24 hours.

The laser is a central technology within photonics having great economic impact. The laser exhibits many of the characteristics of a "general-purpose technology" in that laser technology itself has been transformed by a series of important innovations, with numerous new types of lasers developed over the past 57 years. Innovations in lasers have broadened the applications of this technology, many of which have produced dramatic improvements in the performance of technologies incorporating lasers. It has revolutionized medicine, opened up communication via the internet, and continues to be central to linking cultural, economic and political aspects of the global society. Raising global awareness about light-based technologies can further provide solutions to challenges in energy, education, agriculture, health care and security.

Laser material processing has blossomed into a full-scale discipline and interest is growing at an amazing rate. So much so, that presently we must restrict our attention to the most important ideas, methods, and experimental results. The successful application of laser material processing relies on proper choice of the laser system as well as on a good understanding of the science behind the process.

The present article is conceptual and exemplary in nature and not meant as a wide coverage review, which would require a very large space. In this we will first explore some conventional segments of the industry, namely lasers in cutting, drilling, marking, engraving etc. We will follow it up with further developments, such as laser shock peening, laser forming, and laser surface treatment. In recent times the market is witnessing a paradigm shift buoyed by advances in additive materials deposition, the proliferation of laser annealing for thin films, and the

evolution of 3D printing for rapid prototyping. The advent of ultrashort lasers and their commercial availability has opened up novel applications in processing industry. Finally moving from materials to live tissues we present a flavor of how the laser technology has revolutionized the biological and medical applications as well.

2. Back to the Basics

Lasers are photon energy sources with unique properties. As illustrated in Fig.1, a basic laser system includes the laser medium, the resonator optics, the pumping system, and the cooling system. The energy level of the lasing medium decides the basic wavelength of the output beam. The lasing mediums, such as crystals or gas mixtures, are pumped by various methods such as flash lamp, electrical discharge or diode laser stack. Population inversion occurs when the lasing medium is properly pumped, and photons are generated in the optical resonator due to stimulated emission. The design of the optical resonator determines the photon energy to a very narrow range, and only photons within this range and along the optical axis of the resonator can be continuously amplified. The front mirror lets part of laser energy out as laser output. The output beam may pass through further optics to be adapted to specific applications such as polarizer, beam expander and lens, and beam scanner etc. Nonlinear optics may be used to change the wavelength, for example, the basic optical frequency of the neodymium-doped yttrium aluminum garnet (Nd:YAG) laser at 1.06 µm wavelength may be doubled or tripled by inserting nonlinear crystals in the resonator cavity, generating the wavelengths of 532 nm and 355 nm.
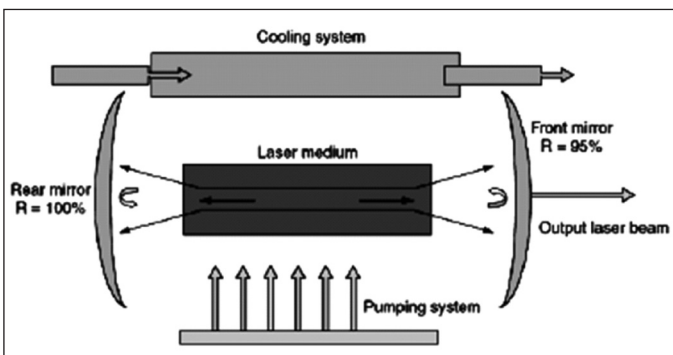

Fig.1: Illustration of a basic laser system.

Understanding the physics in laser material interaction is important for realizing the capabilities and limitations of these processes. When a laser beam strikes on the target material, part of the energy is reflected, part of the energy is transmitted and part of it is absorbed. The absorbed energy may heat up or dissociate the target materials. From a microscopic point of view the laser energy is absorbed by

free electrons first, the absorbed energy propagates through the electron subsystem, and then is transferred to the lattice ions. In this way laser energy is transferred to the ambient target material, as illustrated by Fig.2.
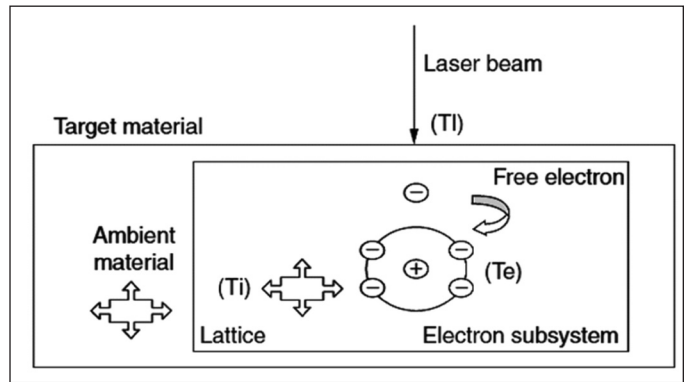
Fig. 2: Laser energy absorption by target material.

At high enough laser intensities the surface temperature of the target material quickly rises up beyond the melting and vaporization temperature, and at the same time heat is dissipated into the target through thermal conduction. Thus the target is melted and vaporized. At even higher intensities, the vaporized materials lose their electrons and become a cloud of ions and electrons, and in this way plasma is formed. Accompanying the thermal effects, strong shock waves can be generated due to the fast expansion of the vapor/plasma above the target.

Given the laser pulse duration, one can estimate the depth of heat penetration, which is the distance that heat can be transferred to during the laser pulse: $D = [4 \times \alpha \times t_p]^{1/2}$ where D is the depth of heat penetration, α is the diffusivity of materials, and t_p is the pulse duration. Laser energy transmission in target material is governed by Lambert's law:

$$I(z) = I_0 . [\exp(-a . z)$$

where I is laser intensity, I_0 is the laser intensity at the top surface, z is the distance from the surface, and a is the absorption coefficient that is wavelength dependent. Metals are nontransparent to almost all laser wavelengths and a is about 100,000 cm⁻¹, which implies that within a depth of 0.1 µm, laser energy has decayed to 1/e of the energy at the surface. Many nonmetals such as glasses and liquids have very different a values. Laser-material interaction thus can be surface phenomena when the laser pulse duration is short and when the material has rich free electrons. Laser energy may also be absorbed over a much larger distance in nonmetals than in metals during its transmission.

When considering the laser power in material processing, the effective energy is the portion of energy actually absorbed by the target. A simple relation for surface absorption of laser energy is: A = 1 - R - T where A is the surface absorptivity, R is reflection, and T is transmission. For opaque material, T = 0, then A = 1 - R

It's important to understand that reflection and absorption are dependent on surface condition, wavelength, and temperature. For example, copper has an absorptivity of 2 percent for CO_2 lasers at 10.6 µm, but it has much higher absorptivity of about 60 percent for UV lasers. Absorption usually increases at elevated temperatures because there are more free electrons at higher temperatures.

3. Analysis of Material Processing System

Laser material interaction can be very complex, involving melting, vaporization, plasma and shock wave formation, thermal conduction, and fluid dynamics. Modeling gives the in-depth understanding of the physics in the study of laser material processing. Without going into the modeling, but as a manager or process engineer, one can get a relatively complete picture following the four-factors analysis: time, spatial, frequency and magnitude.

Time attribute: Laser energy may be continuous (CW) or pulsed, and laser energy can be modulated or synchronized with motion. For CW lasers, the average laser power covers a wide range, from several watts to over tens of kilowatts, but their peak power may be lower than pulsed lasers. CW lasers may be modulated such as ramping up or ramping down the power, shaping the power, or synchronizing the on/off of the shutter with the motion control of the system. For a CW laser one should understand its capability of power modulations, focusing control, and energy-motion synchronization.

There are many types of pulsed lasers. The common range of pulse duration is in the ms range, and the smallest pulse duration is normally larger than 1 µs. The major purpose of pulsating the laser energy in laser material processing is to produce high peak laser power and to reduce thermal diffusion in processing. Taking Q-switched solid-state lasers for example, lasing condition of the cavity is purposely degraded for some time to accumulate much higher levels of population inversion than continuous mode, and the accumulated energy is then released in a very short period - from several tens to hundreds of nanosecond (10^{-9} s). Even shorter pulse durations can be achieved with other techniques and their application will be discussed later. Pulsed lasers have wide range of pulse energies, from several nJ to over 100 J. These pulses can be repeated in certain frequencies called the repetition rate.

For pulsed lasers, basic parameters are the pulse duration, pulse energy, and repetition rate. From these parameters, peak power and average power can be calculated. Similar to CW lasers, one should also understand the capability of power modulations, focusing control, and energy motion synchronization for pulsed lasers. Peak laser intensity is the pulse energy divided by pulse duration and spot irradiation-area. Due to several orders of pulse duration difference, pulsed laser can achieve peak laser intensities $>>10^8$ W/cm^2, while CW lasers normally generate laser intensities $<10^8$ W/cm^2.

Spatial attribute: Laser beam out of a cavity may have one or several modes, which are called *transverse electromagnetic mode* (TEM). For laser material processing, we are concerned with the spatial distribution of the beam that affects the thermal field on the target. Laser intensity usually has a Gaussian beam distribution. For Gaussian beam with beam radius r and for a material with absorption A = 1 - R, where R is the reflectivity and P(t) is the time dependent laser power, the spatial distribution of absorbed laser intensity on the target surface is:

$$I(x, y, t) = (1 - R) I_0(t) \exp [- (x^2 + y^2) / r^2]$$

Where $I_0(t) = 2P(t) / \pi r^2$, is the average laser intensity. Laser energy distribution may take other shapes, such as flat-hat shape, in which the laser intensity at the center is uniform. In general, the formula for laser energy transmitted to the material at depth z is:

$$I(x, y, z, t) = A \times I_0(t) \times \exp (-az) SP(x, y)$$

where A = fraction of laser energy absorbed by the material at the surface, $I_0(t)$ = temporal distribution of laser intensity a = absorption coefficient and SP = spatial distribution of laser intensity. Special optics can be used to change the beam shape and spatial distribution. For example, the beam can be changed from circular to square and uniform.

Laser beam radius is normally defined as the distance from the beam center within which 86.4% or ($1 - 1/e^2$) of total energy is included. Beam radius at the focus is called the *focused spot size*. For lower intensities, laser energy profiler can be used to directly measure the intensity distribution. The laser beam size close to the focus is usually difficult to measure directly, especially for cases when the focused spot size is below tens of microns or when the laser power is high. One solution for high-power lasers is to measure the diameter of laser burnt holes in suitable thin sheet material. For a Gaussian beam, a more accurate solution is to combine experimental measurements with optical calculations. The spot size at large defocus can be measured either by the profiler or the knife-edge method.

More than three measurements at different locations are measured to obtain (Z_n, D_n), n = 1, 2, 3… where D_n is the beam size at location Z_n. The propagation of laser beams in air satisfies the following equation:

$$D_n^2 = D_0^2 + [4M^2\lambda / \pi]^2 [(Z_n - Z_0)^2 / D_0^2]\ ;\ n = 1,2,3…$$

Where D_0 is the beam waist, Z_0 is the beam waist location, and M^2 is the beam quality parameter. Knowing (Z_n, D_n), D_0, Z_0, and M^2 can be determined. Then one can calculate the spot size at any location along the optical axis. Knowing M^2, one can also calculate the beam divergence and depth of focus (DOF). Depth of focus is the range of distance over which the spot size changed from the focused spot size by 5 percent. Fig.3 illustrates the propagation, the beam waist, and the DOF of laser beam.

Laser material processing is claimed to be noncontact because the highest intensity is at the focus while laser optics are some distance away from the target. It is not always convenient to change the focus in processing. The limited depth of focus limits laser machining to relatively thin materials (usually < 15 mm). In material processing, one can move the beam while keeping the part fixed, or move the part on a stage while keep the beam fixed, or move both of them. An XY or XYZ motorized stage is commonly used. Laser beams can be quickly scanned across specified locations by computer controlled reflection optics. This makes high-speed marking or drilling possible. The spatial resolution of laser material processing is influenced by the focused spot size. Shorter wavelength lasers are thus used for precision machining tasks.
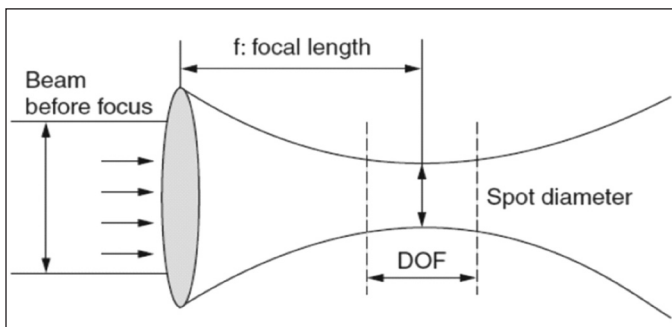

Fig. 3: *The DOF of laser light*

Frequency attribute: The characteristic frequency of energy field is important because materials may respond very differently to energy fields at different frequencies. The frequency decides the individual photon energy of the laser beam. Lasers usually have very narrow spectral width, while other energy sources typically have broad and complex spectral distributions. The diffraction limited spot size is proportional to wavelength and for circular beams, the focal spot size is: $D_{min} = 2.44\ f \times \lambda / D$, where f is the focus length, λ is wavelength, and D is the unfocused beam diameter. Thus for high-precision applications, shorter wavelength lasers are preferred. UV laser ablation of organic polymers can be very different in mechanism compared to infrared or visible laser ablation. The infrared and visible laser ablation is mainly photothermal degradation, while UV laser ablation may involve direct photo-chemical dissociation of the chemical bonds.

Materials show very different absorption properties at different wavelengths. Metals tend to have low absorption at far infrared (CO_2 laser 10.6 µm) while absorption increases with decreasing wavelength. Nonmetals such as ceramics and liquids have strong absorption at far infrared, much lower absorption at visible wavelengths, and increased absorption at UV. At deep UV, almost any material has very strong absorption. That's why different materials may need to use lasers at different wavelengths for efficient energy coupling. Absorption also depends on temperature, purity, and surface condition. Defects or impurity in a transparent media may strongly absorb laser energy and thus create a local thermal point and finally break down the transparent condition. At high enough laser intensity, multiphoton absorption may occur, material reacts nonlinearly to the irradiation. Once the surface temperature rises, absorption tends to increase, which forms a positive feedback. In this meaning, very high laser intensity may be regarded as wavelength-independent material processing.

Magnitude attribute: Major magnitude parameters of laser energy are power (watt), pulse energy (Joule), and intensity (unit: W/m^2 or W/cm^2). The average power of laser is relatively low compared to other energy sources: over 1 kW is regarded as high-power, and a pulsed laser normally has an average power < 100 W. The characteristics of laser radiation is that it can have very high local energy intensity, and this intensity can be well controlled in time, space, and magnitude. When the interaction between laser and target is not continuous, energy intensity is usually the deciding factor. Depending on the laser type, laser pulse energy can be varied from below 10^{-9} J to well above 1 J, the spot size can be varied from sub-microns to over 10 mm, and pulse duration can be varied from several femtosecond (fs = 10^{-15} s) to over 1 s. For pulsed lasers, the laser intensity is equal to $E_0 / (t_p \times \pi r^2)$ where E_0 is pulse energy, t_p is pulse duration, and r is beam radius. For laser pulse energy of 0.1 J, if the pulse repetition rate can vary in the range from 1 Hz - 4 kHz, then the average power is 0.1 - 400 W. Let's vary the pulse length and the acting area and compute the peak intensity. With r = 0.5 µm, peak intensity of a 10 fs pulse is 10^{22} W/cm^2, the intensity of a µs pulse is 10^7 W/

Table 1: Applications of Lasers in Material Processing

| Applications	Intensity (W/cm²) and laser material interaction
Laser surface transformation hardening, laser forming, laser assisted machining, etc.	$<10^5$ W/cm², target heated below melting temperature, phase transformation may occur that can harden the material, elevated temperature can soften the material. Pulse duration $>10^{-3}$ s, CW lasers are used
Laser welding, laser cladding and alloying, rapid tooling, and laser machining	From 10^6 W/cm² to 10^8 W/cm², material melts, some vaporization and plasma formation possible. Pulse duration $>10^{-3}$ s, CW lasers are used
Higher intensity laser machining like marking, grooving, drilling, and cutting	From 10^7 W/cm² to 10^9 W/cm², material melts and strong vaporization occurs, shock wave and plasma formation possible. Pulse duration normally $<10^{-3}$ s, 10^{-9} to 10^{-6} s pulse duration are common, while for micromachining even shorter pulses are used. CW lasers or pulsed lasers are used.
Laser shock processing, laser surface cleaning	Intensity $> 10^9$ W/cm² and pulse duration $<10^{-7}$ s, very intense surface vaporization induces strong shock pressure toward the target.
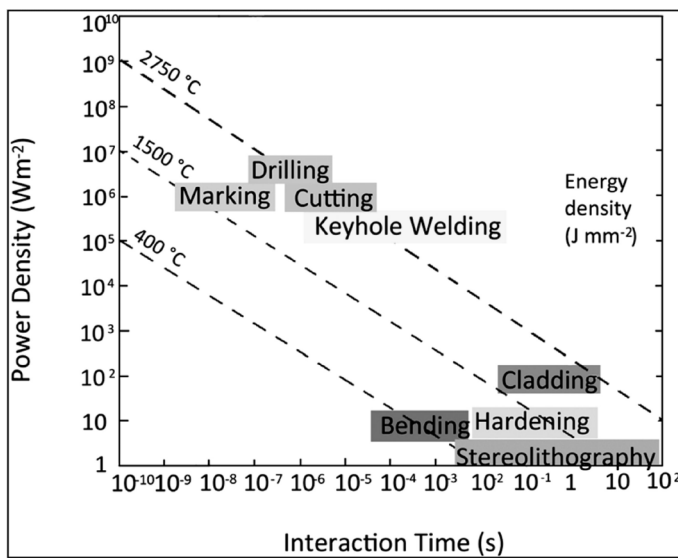
Fig. 4: Processing map based on power density and interaction time

cm² and the intensity of a ms pulse is only 10^4 W/cm². It is clear that laser intensity can be flexibly controlled over very wide range.

Depending on the absorbed laser intensity, different physical phenomena are involved. Applications at various laser intensities and deposition times are briefly shown in Fig. 4 and Table 1

Many material properties such as thermal conductivity and reflectivity vary with material temperature and state, which are further decided by the magnitude of energy input. We tacitly assume that only one photon is absorbed by one electron at a specific time at normal laser intensities, but when the laser intensity is extremely high as in the case of ultrafast lasers (pulse duration $<10^{-12}$ s), more than one photon can be absorbed by one electron simultaneously. This is termed as multiphoton absorption. Material optical property is then highly nonlinear and is very different from single photon absorption. Material can act as if it

were irradiated by a frequency doubled or tripled laser source. In this meaning, we can say that extremely high magnitude of laser intensity can be equivalent to shorter wavelengths. From the above discussion it is seen that four attributes analysis is quite useful. However, caution should be used when collecting the material properties from literature. In laser material processing, material properties are highly temperature, wavelength, geometry, and intensity dependent.

4. Application areas

A laser material processing system consists of the laser source, the beam delivery system, the motion and material handling system, and the process control system. Some systems may integrate the sensing unit to improve process quality. The individual laser material interaction for specific jobs are discussed below (Fig. 5).
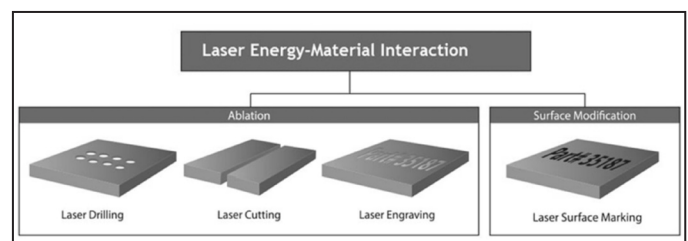
Fig. 5: Various application areas

4.1 Laser Drilling

Laser drilling is one of the oldest applications of laser machining processes. It is a process by which holes are formed by the removal of material through laser-material interaction. Graduating from drilling hole in diamonds, nowadays, it has found successful applications in automobile, aerospace, electronic, medical, and consumer goods industries. A well-known example of laser drilling is the drilling of airfoil cooling holes of aircraft engines.

Lasers used for drilling require higher laser intensities than in laser cutting. With finite pulse energy, high laser intensity can be achieved by tight focus and by short pulse duration. Normally pulsed Nd:YAG lasers or pulsed CO2 lasers are used. Similar to laser cutting, CO2 lasers are better fit for nonmetals and Nd:YAG lasers are better suited for metals. The laser pulse duration is normally less than 1 ms. Average power of the laser may not be as high as that used in laser cutting, but the achievable laser intensity is higher than laser cutting due to shorter pulse duration and smaller spot size. Lasers can be used to drill very small holes with high accuracy and high repeatability. The diameters of holes range from several microns to about 1 mm. For extremely small diameter holes, tighter focus is needed and green or UV lasers, such as frequency doubled or tripled Q-switched Nd:YAG lasers, are used. When the pulse duration is short and the pulse repetition rate is high, laser can drill when the part is moving. Thus very high drilling speed is possible.

4.2 Laser Cutting

Important process parameters in laser cutting are: power, spot size, stand-off distance, focus position, scanning speed, gas pressure, gas flow rate and direction, and gas composition. The quality of laser cutting depends on both the material and the laser. With suitable control of the process parameters, high quality cutting can be achieved.

The lasers used in laser cutting are mainly CO2, Nd:YAG, and excimer lasers. Industrial lasers for cutting typically have power levels from 50 W to 5 kW, although higher powers are used to cut thick sections. Because CO2 lasers have higher average powers with cheaper cost-per-watt and they also have an early history of success in industrial laser cutting, today the majority of cutting operations are carried out by CO2 lasers, especially for nonmetals which have better absorption at far infrared wavelength. Nd:YAG laser has shorter wavelength, smaller focused spot size, and is better absorbed by metals than CO2 lasers. Multikilowatt YAG lasers are commercially available and they usually are delivered by fibers. All these factors lead to the increasing popularity of YAG lasers in industrial laser cutting, especially for metals. Excimer lasers emitting in the ultra-violet (193 nm: ArF, 248 nm :KrF or 308 nm: XeCl) lasers are strongly absorbed by both metals and nonmetals, the spatial resolution are higher than visible and infrared lasers, and thus they are mainly used for high-precision laser cutting, especially for polymers and semiconductors. Recently, conventional lasers using diode pumping and direct diode lasers are reducing their size and increasing their average power

quickly, which may change the dominant role of bulky conventional lasers in industrial laser cutting.

In laser micromachining, a much wider variety of lasers with short pulse durations and high pulse repetition rates are used, such as frequency doubled (Green 532 nm) and tripled (UV 355 nm) Nd:YAG laser, copper vapor lasers, ultrashort pulsed lasers, and excimer lasers. The shorter wavelength and shorter pulse duration helps to increase spatial resolution and reduce the heat affected zone in laser cutting. The higher pulse repetition rate at smaller pulse energy makes it easier to get a smoother machined edge. But the average power of these systems is much lower than industrial lasers, typically < 50 W. High-power industrial lasers are commonly used to cut through larger thickness parts with sufficient speed while micromachining lasers are used to generate small features with high precision.

4.3 Laser Marking and Engraving

Laser marking is a thermal process that creates permanent contrasting marks in target materials by scanning or projecting intense laser energy onto the material. In some cases, the a shallow layer from the target is removed to make the marks, while in other cases, strong laser irradiation can create a color contrasting from non-irradiated area. Lasers are also used to engrave features into materials such as wood or stone products. Laser marking holds around 20% market share of all laser applications and represents the largest number of installations among all laser applications. Lasers can mark almost any kind of material and used for showing production information, imprinting complex logos, gemstone identification, engraving artistic features etc. Lasers used for marking and engraving are mainly pulsed Nd:YAG, CO_2 and excimer lasers.

In general, there are two fundamental marking schemes: one is marking through beam scanning or direct writing, and the other is marking through mask projection. In beam scanning or direct writing method, the focused laser beam is scanned across the target, and material is ablated as discrete dots or continuous curves. In the mask projection method, a mask with desired features is put into the laser beam path. Laser energy is thus modulated when it passes through the mask and a feature is created on the target. The mask can contact the target directly or can be away from the target and be projected onto the target by optics. This method has been used in IT industry to produce very minute and complex features with the assistance of chemical etching. Beam scanning marking has more flexibility than mask projection marking while mask projection marking can be much faster than beam scanning marking.

5. More Applications

We have seen already that laser energy is flexible, accurate, easy to control, and has a wide range of freedom in spatial, temporal, magnitude, and frequency of laser. In this section, we will present some important applications other than the more well-known processes like cutting, drilling etc. described already.

5.1 Laser Forming

When a laser beam scans over the surface of the metal sheet and controls the surface temperature to be below the melting temperature of the target, laser heating can induce thermal plastic deformation of the sheet metal after cooling down without degrading the integrity of the material. Depending on target thickness, beam spot size and laser scanning speed, three forming mechanisms or a mixture of the mechanisms can occur. The three mechanisms are the temperature gradient mechanism, the buckling mechanism, and the upsetting mechanism. Lasers used in laser forming are high-power CO_2, Nd:YAG and direct diode lasers.

Laser forming (LF) of sheet metal components and tubes requires no hard tooling and external forces and therefore is suited for die-less rapid prototyping and low-volume, high-variety production of sheet metal and tube components. It has potential applications in automobile, shipbuilding, aerospace and other industries. It can also be used for correcting and repairing sheet metal components such as pre-welding "fit-up" and post-welding "tweaking." Laser tube bending involves no wall thinning, little ovality and annealing effects, which makes it easier to work on high work-hardening materials such as titanium and nickel super-alloys. LF offers the only promising die-less rapid prototyping method for sheet metal and tubes.

5.2 Laser Hardening

In laser hardening, a laser beam scanning across the metal surface can quickly heat up a thin top layer of the metal during laser irradiation without melting, and after the irradiation it quickly cools down due to heat conduction into the bulk material. This is equivalent to the quenching process in conventional thermal treatment. When favorable phase transformation occurs in this laser quenching process, such as in the case of carbon steels, the top surface hardness increases strikingly. Multi-kilowatt CO_2 lasers, Nd:YAG lasers, and diode lasers are commonly used. The hardened depth can be varied up to 1.5 mm and the surface hardness can be improved by more than 50%. Laser hardening can selectively harden the target, such as the cutting edges, guide tracks, grooves, interior surfaces, dot hardening at naps, and blind holes. The neighboring area remain uninfluenced during laser hardening. By suitable overlapping, a larger area can be treated.

5.3 Laser Glazing

In laser glazing, the laser beam scans over the surface to produce a thin melt layer while the interior of the work piece remains cold. Re-solidification occurs very rapidly once the laser beam passes by, thus the surface is quickly quenched. As a result, a surface with special microstructure is produced that may be useful for improved performance such as increased resistance to corrosion. The surface layer usually has finer grains and may even be amorphous. Laser glazing of cast iron and aluminum bronze has demonstrated much enhanced corrosion resistance.

5.4 Laser Cladding

Laser cladding normally involves covering a relatively low performance material with a high-performance material in order to increase the wear resistance and corrosion. In laser cladding, the overlay material is spread over the substrate or continuously fed to the target surface. Laser beam melts a thin surface layer and bonds with the overlay material metallurgically. The difference with laser alloying is that the overlay material doesn't intermix with substrate. Cladding allows the bulk of the part to be made with low cost material and coat it with a suitable material to gain desired properties and good surface finish. Compared to conventional cladding processes, such as plasma spraying, laser cladding has the advantage of low porosity, better uniformity, good dimensional control, and minimal dilution of the cladding alloy.

5.5 Laser Shock Peening

High intensity ($> GW/cm^2$) laser ablation of materials generates plasma that has high temperature and high pressure. In open air, this pressure can be as high as sub GPa and the expansion of such high-pressure plasma imparts shock waves into the surrounding media. With the assistance of a fluid layer which confines the expansion of the plasma, 5 to 10 times stronger shock pressure can be induced. This multi-GPa shock pressure can be imparted on to the target material and the target is thus called laser shock peened (LSP).

Laser shock processing can harden the metal surface and induce in plane compressive residual stress distribution. The compressive residual stress refrains from crack propagation and greatly increases the fatigue life of treated parts. Compared to mechanical shot peening, LSP offers a deeper layer of compressive residual stress and is more flexible, especially for irregular shapes. It has been shown that LSP can improve fatigue life of aluminum alloy by over

30 times and increase its hardness by 80%. Materials such as aluminum and aluminum alloys, iron and steel, copper, and nickel have been successfully treated. Laser shock processing has become the specified process to increase the fatigue lives of aircraft engine blades.

Conventional laser shock processing requires laser systems that can deliver high pulse energy (~50 J) with very short pulse duration (~50 ns) with a Q-switched Nd:YAG laser. Such laser systems are expensive and the repetition rate is low (several pulses per minute). This situation is improving with more cheaper high-power systems becoming commercially available. On the other hand, this technique can be extended to low pulse energy lasers with short pulse duration and tight focus. Two key requirements for a successful processing are laser intensity > GW/cm^2 and short enough pulse duration (< 50 ns). It is shown that the copper sample treated by a UV laser with 50 ns pulse can be increased by more than 300 percent efficiency.

5.6 Recent Applications

There are many other laser material processing applications in which difficult problems are solved by lasers, such as laser assisted machining of super-alloys and ceramics, laser assisted etching, laser surface cleaning, and laser coating removal. In laser assisted machining, laser is used to locally heat the work material prior to the cutting tool in an attempt to improve machinability of difficult-to-machine materials such as supper alloys and ceramics. It has been experimentally shown that laser assisted machining can extend the tool life, increase the removal rate, and also improve the surface quality of the machined surface.

Etching rate is sensitive to temperature, thus laser beam can be used to enhance etching rate locally. This is in fact one way of direct writing. With the combination of laser heating and chemical etching, semiconductor devices can be etched 10 to 100 times faster than conventional procedures. Laser induced shock wave can be used to clean very minute particles on a silicon wafer, and laser ablation has also been used to remove rust or peel-off coatings by affecting a very thin surface layer.

6. Shifting of Landscape

Buoyed by advances in additive materials deposition, the proliferation of laser annealing for thin films, and the evolution of 3D printing for rapid prototyping, the laser materials processing market in recent times is undergoing seismic change - not only in Europe but in APAC countries such as India, Japan, South Korea and China. Fig 6 shows the materials processing accounts for a significant share of
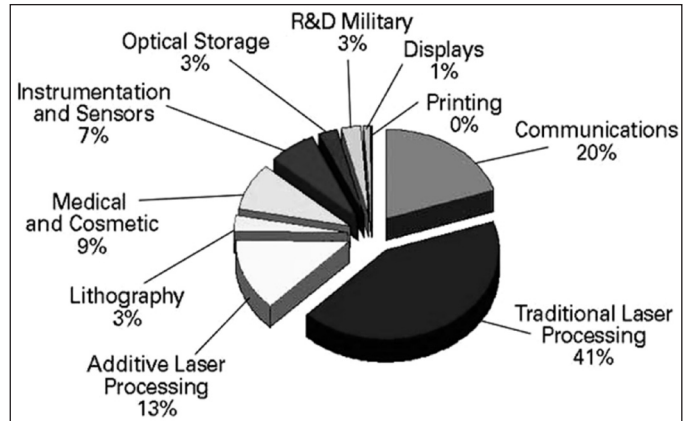

Fig. 6: Materials processing accounts in the total laser market

the total laser market in research compiled by European Photonics Industry Consortium (EPIC).

High-power lasers dominate the materials processing sector. The umbrella of mature power is broad and complex – nanosecond, picosecond or femtosecond; ultraviolet, green or infrared; CO_2, diode-pumped solid-state (DPSS) lasers and fiber lasers. Now the criical question is if there is a key laser that can be customized to cover many applications or if there is only a laser suitable for each of the applications. There's no easy answer; it's basically a combination of choosing the right laser and right application-specific customization.

In essence, laser materials processing has consisted traditionally of the subtractive: that is, materials are removed from the work piece. Laser additive processing, otherwise known as 3D printing, is a complement to these operations. For a number of years, laser additive processing was regarded as an artistic curiosity. However, according to internal market research done by EPIC, it is now an important contributor to the laser systems market, and generated 13% of total revenues in 2014. Furthermore, laser additive processing has grown 20% per year for several years. It is estimated that it will contribute 30% of laser system revenues by 2020.

6.1 Rapid prototyping and additive manufacturing

Rapid prototyping is used in applications where design prototypes or a low volume of complex parts are required to be fabricated quickly without the need of complex tooling. The process is differentiated between stereo-lithography (SLA) using an epoxy polymer and selective laser melting (SLM) using metal or ceramic powder. In both the SLA and SLM processes, a 3D CAD model is sliced into many layers like a stack of cards, then transferred to the SLA or SLM tool. The laser beam is steered by a galvanometric scanner head and builds up the part layer by layer. After each layer is processed, polymer or powder is then deposited on

top of the part and the next laser processing step begins. SLA typically uses a low-power UV wavelength laser to selectively harden a photosensitive epoxy polymer in a bath to form a part. SLM builds up a part from polymer or metal powder by using a sealed- off CO_2 laser or a 1-μm fiber laser. The scope of EPIC is to keep communicating to potential users in the automotive, avionics, consumer electronics, medical, jewelry and many more sectors. It is through addressing the unmet needs of those applications that the technology can develop.

7. Ultrafast laser processing of materials

Ultrafast lasers have been developed for quite some time and are becoming more user-friendly and cost-effective. While laser researchers continue to advance beyond the attosecond (1 as = 10^{-18} s) regime presently, the lasers in the femtosecond, picosecond and nanosecond time regimes have been used to interact with and characterize hosts of different materials. Compared with longer pulse widths, ultrafast pulses are unique in that they are characterized by incredibly high peak intensities and interact with materials on a timescale faster than lattice disorder and heat diffusion. These two features allow ultrafast lasers to control and manipulate the states of materials very precisely.

Ultrafast lasers in micromachining have been expanding exponentially due to their flexibility, speed, and precision. Picosecond and femtosecond lasers are now widely used for applications where conventional solid-state lasers cannot be appropriately applied, such as micro scale surface texturing, cladding, and selective material removal. These novel processing methods are being utilized to manufacture everything from energy-production devices to state-of-the-art electronics.

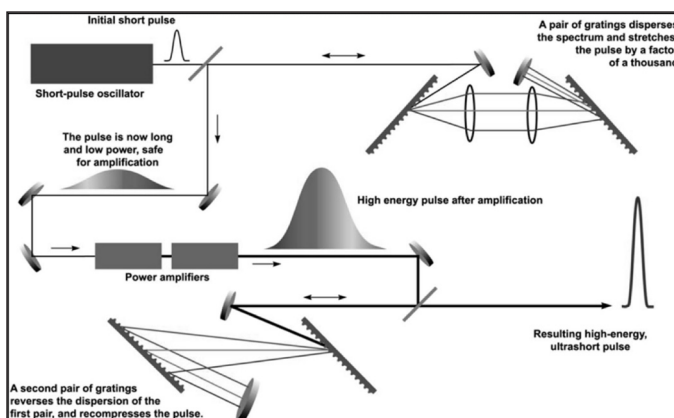Fig 7 shows the schematic of beam stretching, amplifying, and compressing system used in chirped

Fig.7: Schematic of ultrashort pulse laser

pulse amplification. This process is one of the breakthroughs that enabled the creation of ultrafast lasers.

The fs-pulse dictate the kinetics of melting and re-solidification of material. Upon fs-pulse irradiation, the semiconductor experiences several regimes of excitation and relaxation, before returning to its original equilibrium state. The four regimes are (i) carrier excitation, (ii) thermalization (iii) carrier removal, and (iv) thermal and structural effects. Due to the nature of ultrafast pulses, let us have a look at the resulting differences when compared to shorter, ns laser pulses. The fs-laser pulses generate large peak electric fields, which are orders of magnitude larger than the 10^9 V/m coulomb fields that bind electrons to atoms. Large peak pulse energies cause nonlinear absorption in short absorption depths from the irradiated surface, which limits the focal volume where laser energy is deposited.

The dynamics of sub-ps-pulse interactions with semiconductors are unique in two ways. First, the pulse delivers energy to the material on a timescale shorter than the electron–phonon coupling relaxation time. The incident pulse only delivers energy to the electrons, leaving the ions completely "cold." Thermal energy transfer to the lattice only takes place once the pulse is turned off. Thus, decoupled optical absorption and lattice thermalization processes uniquely characterize sub-ps pulse-semiconductor interactions. Second, extremely short pulse widths in time translate to very high peak intensities that can drive nonlinear and multiphoton absorption processes.

Nanosecond pulses excite electrons in a distinctly different process as discussed earlier. When a ns pulse delivers energy to a material, excited electrons transfer energy to the lattice during the time of the electron excitation. Electrons and the lattice thus remain in equilibrium throughout the excitation process. The ns laser heats the solid to its melting temperature during the length of the laser pulse. The ns absorption processes are linear with a much larger absorption length than fs absorption. Linear absorption can lead to deeper melt depths. Compared to the fs-laser case, the ns-induced temperature gradient between the molten layer and the solid substrate is smaller and distributed over a longer distance. Consequently, the melt duration is longer, and the re-solidification front speed is slower, which for silicon typically yields a crystalline structure. If the laser wavelength is transparent to the material, absorption is induced by multiphoton absorption for both ultrafast and ns lasers. Then the ns laser will have a longer penetration

depth due to a smaller absorption cross section as compared with an ultrafast laser.

In contrast, for the opaque materials, the penetration depth is determined by the absorption coefficient due to single-photon absorption for both lasers. In the case of a small absorption coefficient, a shorter penetration depth of the ultrafast laser may be obtained due to a combination of linear and nonlinear absorption. The longer ns-pulse widths translate to lower peak powers compared to fs lasers. Operating at lower peak powers, ns lasers ablate materials by a thermal process. This thermal ablation causes a large heat-affected zone that may induce melt re-deposition and shockwaves, leaving behind thermally induced defects such as cracks and chipping. It should be mentioned that fs lasers are also used as material characterization tools, and many other studies detail their uses in fs pump-probe spectroscopy, laser-induced breakdown spectroscopy (LIBS), and surface-enhanced Raman spectroscopy (SERS).

8. Interaction of the laser with living tissue

Now we will shift our attention from materials to live tissues and in this section we will present a flavor of the phenomenal growth of biological and medical applications of laser. Lasers have been seen as potentially useful light sources for medical applications, because they have three characteristics which distinguish them from conventional light sources: their directivity, the ability to use them in pulsed mode, and their monochromaticity. Directivity allows the transmission of light with the aid of an optical fibre of small diameter (50 to 600 µm). Pulsed mode operation from milliseconds to femtoseconds (10^{-3} to 10^{-15} s) deliver extremely high instantaneous power (10^9 W) with different tissue effects than one obtains with continuous exposures.

8.1 Thermal effects of a laser beam

The thermal effect of lasers on biological tissue is a complex process resulting from three distinct phenomena; conversion of light to heat, transfer of heat and the tissue reaction, which is related to the temperature and the heating time (Fig. 8). This interaction leads to denaturation or to the destruction of a volume of tissue. The important factors are the laser parameters (wavelength, power, time and mode of emission, beam profile and spot size) and the tissue being treated (optical coefficients, thermal parameters and coefficients of the reaction of thermal denaturation). Depending on the intertwining interaction following are the various effects of lasers on tissues:
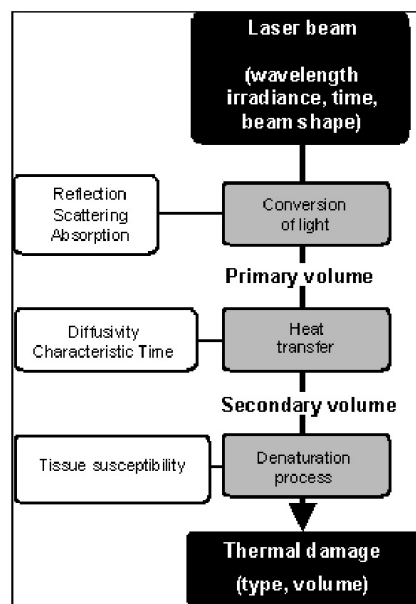

Fig. 8: The three distinct phenomena of thermal effects

(i) Creation of the heat source

The source of heat results from conversion of laser light to heat. The optical reflection determines what proportion of the beam will effectively penetrate the tissue. Precise knowledge of the tissue reflectivity is important because it can reach high levels (30 to 50% reflection of Ar^+- laser beam by the skin). However, for wavelengths longer than the visible range, reflectivity is considerably reduced.

Optical scattering is an interaction of light as it passes through matter, in which the direction of the incident rays is changed by molecules or small particles present in the medium. Scattering plays an important role in the spatial distribution of absorbed energy. At the longer wavelengths (red and near infra-red) where the light is absorbed less, the beam is more penetrating (ignoring scattering effects).

Chromophores are light-absorbing substances within tissue and the absorption is a function of wavelength and chromophore (Fig. 9). Most organic molecules exhibit strong absorption in the ultraviolet region, and so penetration in the UV is very weak (a few microns). In the visible (blue, green and yellow), absorption is principally due to hemoglobin and melanin. Red and near infra-red (600 to 1200 nm) wavelengths are weakly absorbed and penetrate deeply into the tissue (this penetration is, however, limited by optical scattering). In the near and far infra-red, it is water which absorbs intensely, and laser light then has very superficial effects. It is the conversion of light absorbed to heat which produces what we may call "primary" heat.
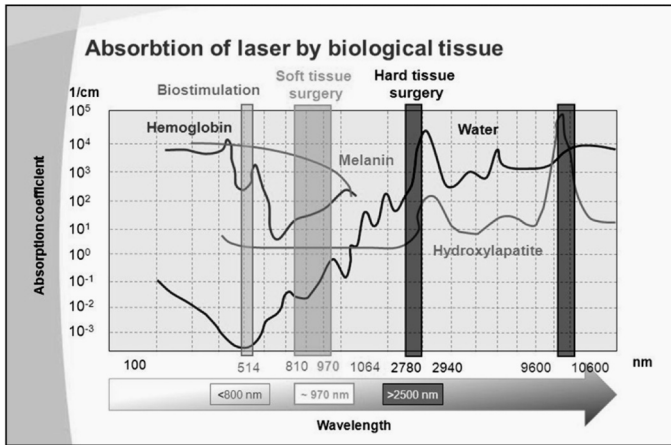
contains a high percentage of water (around 70%), it has a major impact for ablating soft tissue with a laser. The absorption in water is: 3% for 810 nm; 15% for 1064 nm; 35% for 980 nm Absorption in hemoglobin is imperative for good coagulation and successful hemostasis. Table 2 lists various endogenous (naturally occurring) and exogenous (added from outside) chromophores, and their main absorption wavelengths which are of importance in photo medicine.

(ii) Heat transfer mechanisms

The transfer of heat through tissues will tend to enlarge the volume of this source of "primary" heat. This transfer is essentially produced by the mechanism of conduction; the influence of blood circulation (transport by convection) is negligible. Conduction may be considered to be like a transfer of energy by interaction with tissue particles. This transfer occurs randomly between the more and the less energetic particles and results in a "secondary" heated volume which is bigger than the "primary" source which is based only on the

Fig. 9: Absorption spectrum of the main chromophores in tissues

It has been found that laser light at 970 nm is important in biological / medical applications. A laser's wavelength determines many of its properties and capabilities because different wavelengths are absorbed by tissue at varying rates. Since tissue composition (amongst others) is water-hemoglobin-melanin and soft tissue

Table 2: Absorption features of various endogenous and exogenous chromophores

Endogenous	Wavelength	Exogenous	Wavelength
Nucleic acid	260-280 nm	Psoralens	340-370 nm
Protein	280-300 nm	India ink	400-800 nm
Hemoglobin	400, 542, 554, 576 nm	Indocyanine green	805 nm
Melanin	400-800 nm	Porphyrins	400, 630 nm
Water	1400-10000 nm	Chlorins	650-690 nm
Lipid		Bacteriochlorins	720-780 nm
Flavins	420-500 nm	Phthalocyanines	670-740 nm
Porphyrins	400, 630 nm	Methylene blue	660 nm
Cytochrome c oxidase	620-900 nm	Rose Bengal	540 nm

conversion of light to heat. It is this "secondary" heated volume which should be considered when studying the denaturation of tissue.

(iii) Mechanism of tissue denaturation

Denaturation of tissue is the final result of thermal action on tissue. Knowledge of the kinetics of this transformation is necessary to describe the process of denaturation. These kinetics depend on the temperature in the tissue, on the heating time and on the susceptibility of the tissue to thermal damage.

(iv) Thermal action of a laser

Thermal action of a laser beam can be described as one of three types, depending on the degree and the duration of tissue heating:

Hyperthermia: meaning a moderate rise in temperature of several ^{o}C, corresponding to temperatures of 41to 44°C for some tens of minutes and resulting in cell death due to changes in enzymatic processes. This is a difficult procedure to control and so it is little used in practice.

Coagulation: refers to an irreversible necrosis without immediate tissue destruction. The temperature reached (50 to 100° C) for around a second, produces desiccation, blanching, and a shrinking of the tissues by denaturation of proteins and collagen.

Volatilization: means a loss of material. The various constituents of tissue disappear at above 100°C, in a relatively short time of around one tenth of a second. At the edges of the volatilization zone there is a region of coagulation necrosis which is a gradual transition between the volatilization and healthy zones. The haeomstatic effect is due to this region of coagulation necrosis. If the volatilized zone has a large area of a few mm in diameter, it is possible to destroy tumours bigger than those treated by a simple coagulation. If the volatilized region is narrow, a cutting effect is then obtained.

It also emphasizes to the development of several ideas:

8.2 Photoablative effect

This effect is defined as a pure ablation of material without thermal lesions at the margins, such as one would get with a scalpel which occurs due to dissociation. With very short wavelengths (190 to 300 nm), the electric field associated with the light is higher than the binding energy between molecules. The molecular bonds are broken and the tissue components are vaporized, without generation of any heat at the edges. This effect is obtained with excimer lasers emitting in the ultra-violet (193 nm: ArF, 248 nm :KrF or 308 nm: XeCl). The action is very superficial, only over several microns, because light at these wavelengths is very strongly absorbed by tissue.

The photablative effect may also be obtained by lasers emitting in the infra-red such as the Erbium:YAG at 2900 nm. Since 2900 nm is at a peak of absorption in water, the absorption in tissue is so intense that the vaporization is immediate and superficial. Additionally, the very short duration of the pulse (a few hundred microseconds) avoids the phenomenon of thermal diffusion.

The photoablative effect offers no practical advantage for making incisions or for ablating vascular tissues because they will bleed in the same way as with a scalpel. It can only be used on tissues which will not bleed. It is in fact difficult to imitate the action of the scalpel because one must take into account not only the direction and the speed of cutting, but also the pressure applied to the tissue. Lasers are suitable for this application because of the reproducibility of their effects which can be modelled, and because of the absence of mechanical contact with the tissue. By this way, excimer lasers have found application in ophthalmology for photorefractive keratoplasty. Fig. 10 depicts the spectral absorption of different eye media and eye transmission up to the retina.

This procedure is for patients presenting with refraction problems. In myopia, the image is focused in front of the retina while in case of hypermetropia, it is the opposite. The laser technique is used to change the curvature of the cornea in order to correct the difficulty of focusing an image on to the retina. Similarly, various corneal pathologies can be treated: for example, the after-effects of keratitis, dystrophy or keratinisation. A preliminary analysis of the corneal topography allows specification of the correction required and to control the laser treatment parameters.

The laser used is an ArF excimer laser (193 nm) which is immediately stopped by the superficial layers of the cornea, resulting in a photoablation of the surface. The depth of photoablation can be varied from several tens to about 150 microns; typically one dioptre of myopia corresponds to about 10 microns of photoablation.

The treatment can be on an out-patient basis after a contact corneal anaesthetic. It is important that the patient does not move his eye during the treatment, which may last for several seconds. The laser beam is adjusted either by a diaphragm or by a mask. The operation is not painless, and blurring of the vision lasts for several weeks, while it becomes progressively clearer. The complications of photorefractive keratoplasty are: regression of the correction, dazzle, and astigmatism due to possible decentring of the laser beam.
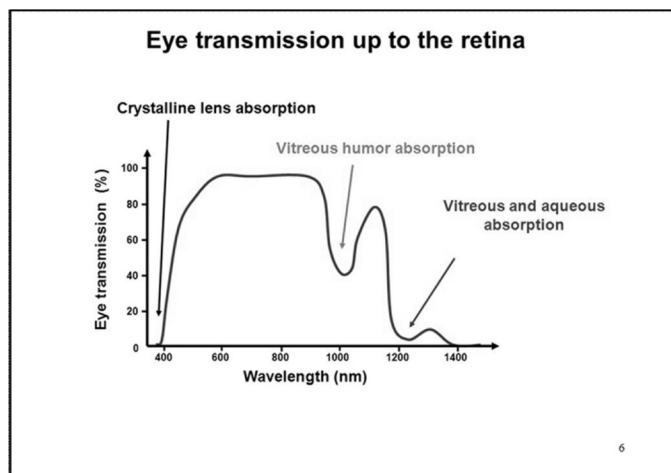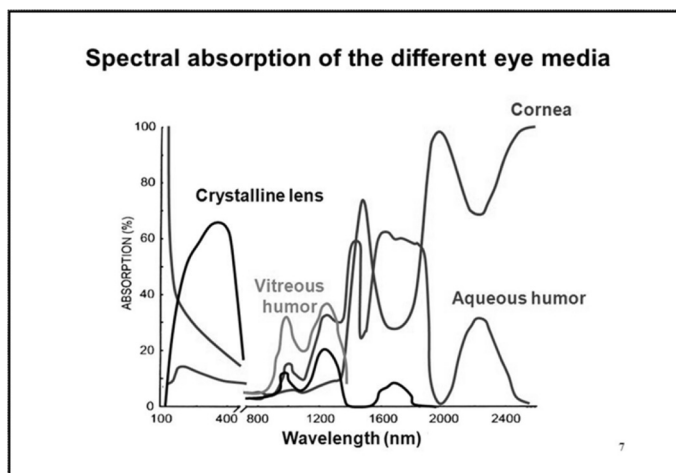
Fig. 10: Spectral absorption of different eye media and eye transmission up to the retina.

8.3 Photodynamic effect

Photodynamic therapy (PDT) involves the relatively selective uptake of a photosensitizing drug and subsequent irradiation with light of a suitable wavelength. In the presence of oxygen, singlet oxygen is produced with the induction of a cytotoxic action. Illumination is required at a wavelength corresponding to the peak absorption of the drug. Localization of the effect in the target tissue is most commonly achieved by intravenous injection of the photosensitizer. It can also be administered topically, by spraying the surface of the organ, or orally. It may be noted that the photosensitizing drugs are not toxic at the dose levels used.

The illumination is delivered at a time between several hours to several days after the administration of the photosensitizer. The wavelength is chosen judiciously which can be absorbed well by the drug and suits the depth of the desired effect in tissue. Light in the green region of the spectrum is used for superficial effects and in the red for deeper effects. Laser light is delivered using a fibre optic for endoscopic treatments. While only a laser beam can currently deliver power levels of around one watt at the end of a fibre in the green or red regions, non-laser light sources are also being developed. Usually, dye lasers pumped by a blue or green laser (doubled Nd:YAG or argon ion) are used. Diode lasers emitting in the red region are attracting interest because of their convenient portability.

The phototoxic action of the drug on the target cells is well understood. The drug after being excited by photon absorption finally returns to its ground state and while doing so transfers its energy to ambient oxygen producing singlet oxygen. This singlet oxygen is an extremely reactive substance which oxidizes all the tissue constituents coming into contact and the effect is therefore very localized. In contrast to thermal effects, photochemical effects need only low power densities, several tens of watts / cm^2, so as not to degrade the drug by thermal effects, and long exposure times (typically ten minutes). The only photosensitizing drug currently authorised for the market is photofrin, a hematoporphyrin derivative. The drug focuses on recurring bronchial and oesophageal cancers. Various other applications are presently being researched.

The potential applications of PDT are principally in oncology; for example palliative treatments for obstructive cancers in the airway or esophagus. Treatment may be curative for small cancers in these sites and in multi-centred cancers such as those in the bladder. In dermatology, the quality of the cosmetic result may justify this technique for skin cancers. There are also indications in neurosurgery, ophthalmology, gynecology, ENT, etc. PDT can also be applied to pre-cancerous lesions such as dysplasia of the lower esophagus. Finally, there appear to be potential applications outside oncology with viral lesions (e.g. HPV, herpes), psoriasis, and in vitro, the inactivation of HIV during blood transfusion as well as changing immune status by altering lymphocyte activity.

9. Concluding Remarks

In this brief overview we found that laser material processing have become indispensable engineering solutions for a large number of applications. High initial capital cost was one of the major obstacles in choosing the laser material processing. Moreover, the appearance of new applications and markets for lasers has created strong incentives for further investment in innovation in lasers. All of this feedback and self-reinforcing dynamics are classic features of general-purpose technologies. The global market for laser systems for materials processing

increased by 6.8% in last year and reached the new record volume of $ 12.6 billion. The increase was mainly due to China, Europe, North America and Japan. Laser macro processing systems, used for cutting, welding, marking, and additive manufacturing, account for 75% of the total market volume. Still, the automotive industry is a major driver with substantial investments into high-power laser welding and cutting equipment. Medical and cosmetic applications have a share of about 10% which is a very healthy indication.

The market for laser systems for microelectronics processing accounts for 25% share and this segment expanded by 15% last year mainly due to the increased use of laser processes for the manufacturing of mobile electronic devices and their components such as displays and semiconductors. Fiber lasers now hold a 40% market share, ahead of gas lasers, represented by CO_2 and excimer lasers (35%), and bulk solid state and diode lasers (25%). The demand for fiber lasers grew by 15% last year to $1.3 billion. Their major applications are cutting, welding, marking, and additive manufacturing. The market volume for bulk solid state lasers grew in the ultrashort-pulsed segment. Fiber lasers continued to take away market share from high-power CO_2 lasers as well as bulk solid state lasers. In the meantime, CO_2 lasers are finding their major applications in marking and the processing of non-metals. Excimer lasers are mainly used for microlithography and in flat panel display manufacturing.

Judging from the development since the days of drilling hole in diamond, it is quite clear that laser material processing is a dynamic field and even today new and interesting technology is being pursued throughout the world. Therefore, assessment of evolving technology must also be a continuing activity, not only to recognize the impact of the scientific achievements themselves, but also to keep the entire processing endeavor in step with a changing world-wide economic and political environment.

Acknowledgement

Suggested Reading

1. Laser Material Processing : W. M. Steen (Springer, London, 1991); Laser material processing-an overview : W M Steen; Appl. Opt.5 (2003) S3–S7

2. Principles of Laser Materials Processing : Elijah Kannatey-Asibu, Jr.; April (2009) Wiley ISBN: 978-0-470-45919-5

3. Lasers in refractive surgery: history, present, and future : L.J. Kugler and Ming X. Wang ; Appl. Opt.49 (2010) F1-F9

4. Ultrafast laser processing of materials: a review : K. C. Phillips, H. H. Gandhi, E. Mazur and S. K. Sundaram; Advances in Optics and Photonics, 7 (4) 684 (2015)

Dr. Sisir K. Sarkar, *Outstanding Scientist of DAE served as Director, Chemistry Group and Head, Radiation & Photochemistry Division, Bhabha Atomic Research Centre. He did his post-doctoral work in the area of chemical dynamics at Columbia University, USA.He has been to various laboratories in USA, Russia, Europe and Japan as visiting scientist and worked with various laser systems including Free Electron Laser. He has more than 400 papers in International journals, symposia and conferences to his credit. He is Fellow of Maharashtra Academy of Sciences. He served as President of Indian Laser Association (ILA) and Society for Material Chemistry (SMC) and Vice-President of Indian Society of Radiation & Photochemical Sciences (ISRAPS). He has been passionately involved till date in Radiation and Photochemical research using lasers and accelerators. Presently he is Raja Ramanna Fellow of DAE associated with National Centre for Free Radical Research (NCFRR), Pune and Hon. Professor in the Chemistry Department of Savitribai Phule Pune University.*

Ionic Liquid Based Synthesis of Energy Efficient Nanomaterials

Rahul Kumar Sharma, Yogendra Nath Chouryal, Pushpal Ghosh*

School of Chemical Science and Technology, Department of Chemistry,
Dr. Harisingh Gour University (A Central University), Sagar-470003, M.P. India
* E-mail: pushpalghosh27@gmail.com

Abstract

Ionic liquid based "green'" syntheses are currently receiving the highest attention for preparing efficient materials. This feature article aims providing and introduction to the two very important fields. First is the synthesis of rare-earth doped materials using ILs and their several photonic and biophotonic applications and second is the synthesis of semiconducting nanomaterials and their potential catalytic/ photocatalytic applications. Different photoluminescence mechanism like upconversion and down conversion which has immense potential for environmentally benign and energy efficient lighting including solar cell applications are explained first. In addition several other biophotonic applications like photodynamic therapy, FRET (Förster Resonance Energy Transfer) based biological detections are explained. In the following, semiconducting nanomaterials using ILs with tunable properties are discussed followed by their photocatalytic applications useful for removal of toxic dyes. Last but not the least, in this article, it is shown how ILs can not only act as a solvent, capping or templating agent but also it can tune the crystal phase, morphology of the host materials which eventually tune the photophysical properties of the dopant rare-earth ions and optoelectronic properties of semiconducting nanomaterials.

1. Introduction

Designing of nanomaterials with desired properties/ property combinations for the several applications such as magnetic, optoelectronic, scintillator, electroluminescence, bio-imaging, bio-medical application etc. is one of the most emerging topic of present time [1-3]. Amongst many, synthesis of energy efficient materials useful for solar light conversion, designing of environmentally benign lighting, catalytic/photocatalytic degradation of toxic pollutants are utmost important. Normally, light emitting or light harvesting nanomaterials, can be categorized into three groups, semiconducting, rare-earth (RE) based and organic based nanomaterials. Among them, semiconductors and organic nanomaterials exhibit size-dependent optical property due to quantum confinement effect [2,4]. On the other hand, rare-earth doped nanomaterials show size independent optical property as *f-f* electronic transitions are substantially shielded by high energy $5s$ and $5p$ orbitals. However, crystal phase, morphology, core-shell formation, lattice strain and most importantly by judicious selection of host matrix, dopant ion combination,optical properties of RE based nanoparticles can be effectively tuned [1,2,4-6]

Optimizing synthesis protocols is one of the important steps for obtaining the nanomaterials with desired properties like particle size, crystal phase, morphology etc. Obviously, judicious choice of solvent, surfactants, reactant precursors is very crucial [1,2,7-9]. Numerous hazardous organic solvent and surfactant are being used so far for the synthesis and tuning the properties of nanoparticles.

And, exploration of environment-friendly synthesis protocol is need of the hour. Different synthesis methods ranging from solvothermal, hydrothermal, chemical vapor deposition, sol-gel method, micro-emulsion, epitaxial method, thermal decomposition methods, combustion, microwave assisted etc. have been developed so far [1,2]. Currently, ionic liquids (ILs) started to draw a special attention both in industries and academia. ILs are generally the organic salt comprised of cation and anion and exist as a liquid at ambient conditions [7-9]. Physical and chemical properties of ILs make them much superior than other organic solvents due to their wide liquidus range, large electrochemical window, negligible vapour pressure, non-flammability, high thermal stability, high viscosity etc. leading to several applications in different fields such as organic solvent, *f*-element separation, catalysis, electrolytes etc. [7-9]. However their role in synthesis of nanomaterials is still in its infancy. Intriguing properties like tunability in proper cation and anion combination, in changing the alkyl chain length, concentrations, viscosity etc. helps IL to be termed as "*green and designer*" solvent and can be very effective tool for nanomaterials synthesis. Some reports have already shown how ILs can be used as a capping and templating agent for tuning the crystal phase, size, and morphology of the nanoparticle [2,3,10-17]

Herein, the role of ILs for the synthesis of energy efficient nanoparticles is discussed in detail. In this article, the whole discussion is divided into two categories: rare-earth doped materials which have different photonic
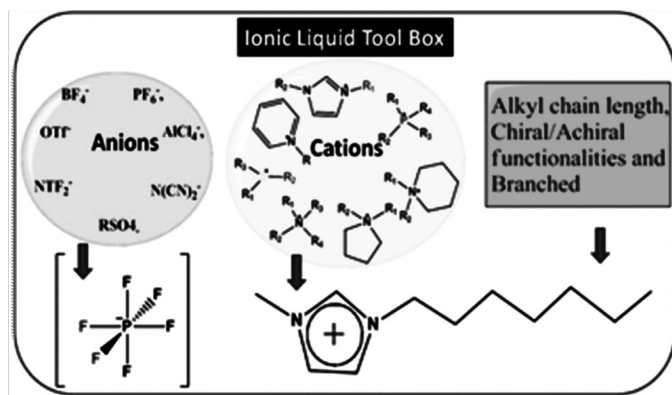
Fig. 1: Tool box for the synthesis of numerous ILs via judicious selection of cation and anion.

and biophotonic applications and semiconductors based materials useful for catalytic/photocatalytic degradation of dyes etc (Figure 2). It is envisaged how the tunable features of the IL can be explored for tuning the structural and physical properties of host materials (both rare-earth based and semiconducting) and then eventually tunes the optoelectronic properties of the nanoparticles. A special emphasis is given on how ILs can be used as capping and templating agent for tuning the size, shape, crystal phase and lattice strain of nanoparticles. Upconverting and down converting nanoparticles useful for increasing the efficiency of the solar cell along with other applications like biological detections etc. will be discussed. In addition, synthesis of semiconducting nanoparticles in ionic liquid medium and their catalytic/photocatalytic effect will be highlighted.
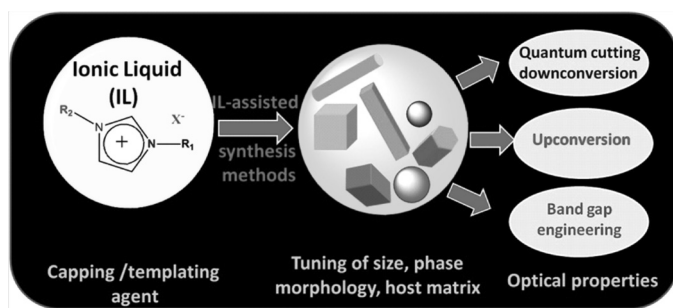

Fig. 2: A general scheme depicting IL based synthesis of materials.

2. Rare-earth (RE) based light emitting nanomaterials

2.1 Synthesis of IL assisted RE-doped nanoparticles

To prepare efficient rare-earth doped materials, it is very important to choose a good host material. Normally host materials are chosen on the basis of high chemical and thermal stability, refractive index and low phonon energy [1-3,6,15-17] In general, oxides, phosphates, vanadate and fluorides are well-known as a host material for doping of the RE ions [1,2]. Amongst them, due to lower phonon energy and tunability in crystal phase, different binary

and ternary fluorides are explored recently [1-3,6]. Several synthesis methods have been developed so far, however, room temperature ionic liquid (RTIL) assisted synthesis of the host materials is currently attracting a remarkable attention. Not only, IL acts as capping and templating agent, reaction solvent etc. however it also acts as reaction partner especially for synthesis of fluorides based host materials. Thus the judicious selection of the IL for the synthesis of host materials is very significant [11-18]. For example, Lorbeer et al. used different ILs in which $[C_4mim]^+$, $[C_2mim]^+$, $[C_4mim]^+$, $[Cholin]^+$, $[P_{66614}]^+$and $[C_4py]^+$ participate as a cation and BF_4^- and PF_6^- as counter ions (anion) [12]. They have used all these ionic liquids to prepare binary fluorides for example quantum cutting Eu^{3+} doped GdF_3 where ILs are not only act as a solvent, templating agent but also act as a fluorine source on hydrolysis of the counter anion BF_4^- and PF_6^- [12] Due to presence of large cation and anion and high polarizability, IL can absorb microwave efficiently and same group, again used the IL ($C_4mimBF_4^-$) as reaction partner (source of fluoride) for the preparation of BaF_2: Eu^{3+} nanomaterials [3,13]. Same IL ($C_4mimBF_4^-$) was used again for the preparation of green emitting quantum cutting $NaGdF_4$: RE (Er/Tb) nanoparticles [14]. On the other hand, Ghosh et al. employed different ILs assisted solvothermal method for synthesizing the quantum cutting Eu^{3+} doped $NaGdF_4$ nanophosphors [11]. Judicious choice of reaction temperature, effect of IL and ratio of Gd:F (1:8) were noticed as central factors for selective synthesis of hexagonal $NaGdF_4$:Eu^{3+} nanoparticles. In an another work, Ghosh et al. [15] reported synthesis of oxygen-free Eu^{3+}-doped $NaGdF_4$ nanocrystals using imidazolium-based ILs at room temperature and using only water as solvent under normal stirring. Selective tuning of the shape, morphology and, most importantly, the crystal phase of the host lattice is achieved by changing the alkyl side length, the H-bonding capabilities and the concentration of 1-alkyl-3-methylimidazolium bromide ILs, $[C_nmim]Br$. When $[C_2mim]Br$ IL is used, hexagonal $NaGdF_4$ nanoparticles are obtained. In the case of ILs with longer pendant alkyl chains such as butyl (C4), octyl (C8) or decyl (C10), extremely small nanoparticles of the cubic polymorph form, which then convert even at room temperature (RT) to the thermodynamically favored hexagonal modification. The hexagonal nanomaterial shows a substantial quantum cutting effciency (154%) whilst in the cubic material, the effect is negligible (107%) [15]. It is revealed that $[C_2mim]^+$ ions anchor to the (110) plane of the primary nuclei, leading to reduced reaction rates and formation of the thermodynamically stable hexagonal phase through an imperfect oriented attachment mechanism. However, cubic polymorph which is less thermodynamically stable

is obtained for ILs with higher alkyl chain lengths. As initially extremely small particles with an extraordinarily high surface energy form, the crystal phase completely changes to the hexagonal form spontaneously over an extended time at room temperature [15].

2.2 Optical properties RE ion/s doped nanoparticles

The common electronic configuration of RE^{3+} ion can be represented as [Xe] $4f^n$, where n is the number of electron present in the *f*-orbitals. The 4f orbitals are well shielded by the filled $5s^2 5p^6$ sub-shells. As a result, the energies of the electronic levels are not greatly influenced by the chemical environment in which the rare-earth ions are located resulting observation of sharp inner-shell *f-f* transitions at well defined energies [1,2,4]. The origin of photoluminescence property in RE^{3+} ion is predominated intraconfigurational *f-f* electronic transitions and their number of allowed excited states can be determined by 14!/(14-n)!n!, where n is the number of electrons situated in the *f*-orbitals in III oxidation state (RE^{3+})[2,4].

On the basis of a thoughtful combination of trivalent RE^{3+} ions, they exhibit various photophysical processes such as normal direct excitation, charge transfer, energy transfer, quantum cutting downconversion and upconversion. Often, quantum cutting downconverted and upconverted nanomaterials are substantially synthesized for the widespread applications both in photonic and biophotonic. Herein, a brief overview about the trivalent RE-doped quantum cutting downconversion and upconversion nanomaterials is given [1,2].

2.2.1 Quantum cutting downconversion nanomaterials

Quantum cutting downconversion is a process in which one high energy photon is converted by a material into more than one low energy photons. Figure **3** shows the mechanism of the quantum cutting downconversion and this can be understood as two types of RE^{3+} ions are doped in a host matrix, one is called sensitizer which absorbs an incident photon of VUV region and via two successive energy transfer processes it is donated to another dopant ion called activator which emits the two low energy visible photons [1,2]. So the selection of dopant ion is very crucial to get such kind of materials and the most commonly used dopant ions for getting the quantum cutting downconversion nanomaterials are Gd^{3+} and Eu^{3+} as sensitizer and activator respectively. For example, Lorbeer et al. found high quantum cutting efficiency (194 and 197%) which is very close to the maximum possible theoretical limit in the trigonal sub-10 nm GdF_3:Eu^{3+} nanoparticles.[12] However, phase dependent quantum cutting efficiency was depicted by Ghosh et al.[11] They observed that 187%

and 127% quantum cutting efficiency were found in the hexagonal and cubic phase of $NaGdF_4$: Eu^{3+} nanoparticles respectively [11]. The same group again reported the phase dependent (hexagonal~154% and cubic~107%) high quantum efficiency of oxygen free-Eu^{3+}-doped $NaGdF_4$ nanoparticles at low temperature using the several ionic liquids [15]. Mudring and co-workers illustrated that alkali co-doping along with the rare-earth ions in alkaline host matrices not only increases the quantum cutting efficiency through charge compensation but also enhances homogeneity, crystallinity for improving the quantum cutting efficiency near to the maximum possible theoretical limit (199%) [13]
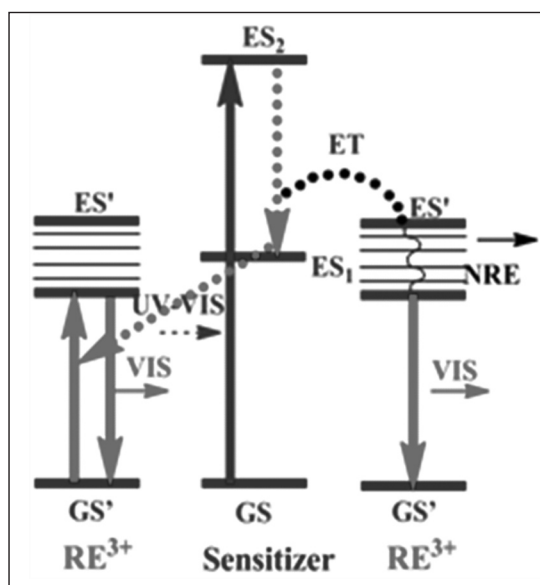

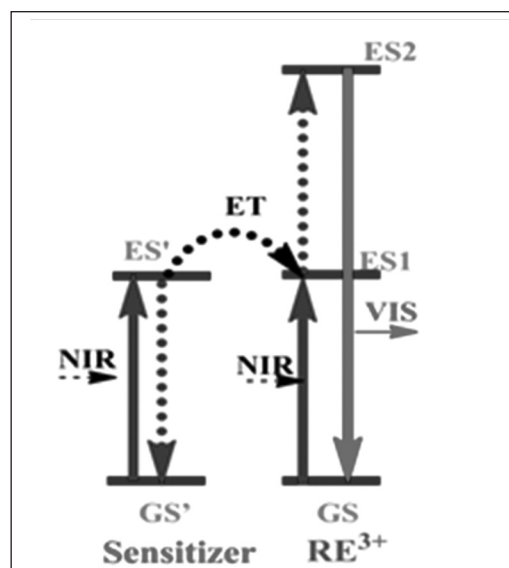*Fig. 3: A schematic diagram of quantum cutting downconversion process.*

Fig.4: A schematic diagram of energy transfer upconversion process

2.2.2 Upconversion (UC) nanomaterials

Contrary to quantum cutting downconversion process, upconversion is a photo-physical process in which two low energy pumped photons (preferably of NIR regime) are absorbed first and then converted into one high energy photon of visible light. In other words, it is one of the most studied nonlinear optical process after second harmonic generation and two photons absorption and it was independently discovered by Auzel as well as Ovsyankin and Feofilov in 1960s [1,2].

Upconversion photo-physical process can be further classified into five categories such as a) energy transfer upconversion (b), excited state absorption, (c) mediated photon-avalanche effect, (d) co-operative energy transfer upconversion and (e) energy migration upconversion. Although, energy transfer upconversion is the most studied photo-physical process (as shown in Fig. 4) [1,2]. In this process, sensitizer and activator simultaneously absorb pumped photons of NIR region, after that sensitizer is relaxed to GS by transferring its absorbed energy to the activator. Then activator is excited from the metastable state to the excited state. When activator relaxed from excited to GS, it emits visible region of light. There are numerous examples in which ILs are employed for synthesizing the upconversion nanomaterials. $[C_4mim]BF_4$ IL is extensively used for the synthesis of $NaYF_4$ doped with RE^{3+} ions as upconverting nanomaterials. Here, $[C_4mim]BF_4$ and $[C_4mim]PF_6$ have played a vital role as solvent, reaction partner (releases fluoride ion on hydrolysis) and templating agent in nanomaterials synthesis[16-19]. First time Liu et al. employed ionothermal method to prepare water soluble, upconverting and hexagonal $NaYF_4:Yb^{3+},Er^{3+}/Tm^{3+}$ nanophosphors, where IL, $[C_4mim]BF_4$ was used as solvent, fluorine source and templating agent [16].

Chen et al. prepared wide range (200-430 nm) of spherical RE^{3+} (Yb /Er /Tm) doped with $NaYF_4$ nanoclusters and nanoparticles using the $[C_4mim]BF_4$ and $[C_4mim]PF_6$ respectively as a source of fluoride ion via microwave-assisted synthesis method and interestingly they noticed excellent upconversion properties [17]. Similar synthesis method was also employed for the preparation of $NaYF_4$ using the$[C_4mim]BF_4$ as a reaction partner by other group [18,19].

2.2.3 Applications of RE^{3+} ion/s doped nanophosphors materials

Rare-earth ion doped nanophosphors materials have an enormous range of applications but majorly we classified them into two parts a) photonic and b)
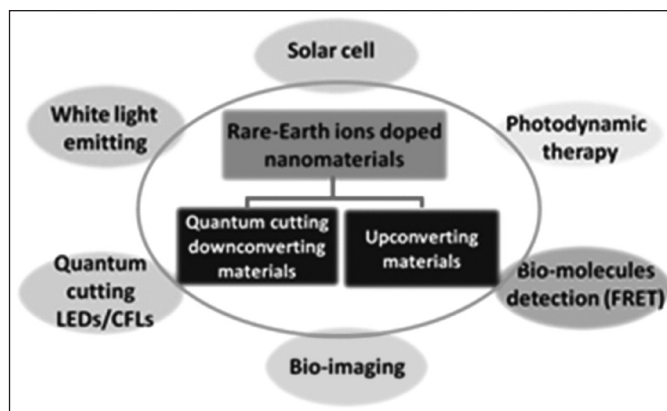

Fig. 5: *Applications of RE³⁺ ions doped nanomaterials*

biophotonic applications, which will be discussed here briefly (Fig. 5).

2.2.3.1 Photonic applications

White light emitting materials:

Currently, the environment-friendly and cost effective production of energy efficient nanophosphor materials for the generation of white light is an important research topic. To achieve this, there are two practices are being employed such as a combination of three color LEDs in a single device like blue, a green and a red and phosphor-converted LEDs (pcLEDs) to get the white light. The second concept relies on phosphor converted LEDs, which bear good similarities to compact fluorescent lamps (CFLs). A phosphor material converts the blue or UV light emitted by the diode to white light. This can be achieved in a blue LED by combination with a yellow phosphor, where the transparency of the phosphor layer controls the final light colour [20], or with the combination of a near UV LED and a judiciously chosen phosphor materials, which themselves create white light emission [21]. By doping proper concentration of Ce^{3+}, Tb^{3+} and Eu^{3+}/Sm^{3+} in any host of low phonon energy like fluorides etc. white light may also be obtained. For example, upon exciting the allowed 4f-5d transition Ce^{3+} excitation, energy transfer occurs from Ce^{3+} to Tb^{3+} and then to Eu^{3+} or Sm^{3+}. This kind of energy transfer may results in white light comprised of blue light from Ce^{3+} ions, green light from Tb^{3+} ions and red light from Eu^{3+} ions.

Energy efficient and environmentally benign lighting:

There are two worldwide accepted problems: efficient and effective utilization of energy resources and removal of conventional light emitting materials in which toxic element such as mercury (Hg) is used as discharge medium. It is widely accepted that solar energy is the one of the cheapest source for any form of energy (heat, light and electricity) but the efficient utilization of whole spectrum

range of solar light is still a challenge. Upconversion and quantum cutting nanomaterials can be effectively used to enhancing the solar cell efficiency and removing the old light emitting sources. Normally spectral mismatch occurs resulting in the energy loss in the conversion of solar energy to electricity as the photons of lower or lesser the band gap energy are not absorbed by a solar cell and in this regard, upconverted material can help. An upconverting phosphor material absorbs the transmitted sub-band-gap photons by sequential ground state absorption/excited state absorption followed by the creation of an excited state in the up-converting phosphor from which high energy photons are emitted. Then these photons can be absorbed in the solar cell to create electron-hole pairs. Shalav and co-workers used $NaYF_4$:Er^{3+} upconverted phosphor for enhanced NIR silicon solar cell response.[22] An UPC layer was placed on the rear of bifacial buried contact silicon solar cell and it was verified that solar cell response in the NIR region was enhanced. Similarly quantum cutting materials can be useful for increasing the solar cell efficiency. Photons of the solar spectrum that have higher energy than the band gap of the semiconducting material overshoots the band gap and the excess energy is lost. So, suitable quantum-cutting phosphors can cut this energy in two photons of lower energy those are able to cross the band gap of the solar cell material. By this, the efficiency of the solar cell can be improved beyond the Shockley-Queisser limit [23].

Energy-saving lighting is a very important topic. Developed countries have already or are currently planning to replace conventional incandescent lamps which consume very high energy and these lamps are now being replaced by more environmentally benign light sources like compact fluorescent lamps (CFLs). However, the commercial CFLs also contain mercury (Hg) which certainly generates some environmental and health issues after their disposal. Possible alternatives in which Hg can be replaced by an environmentally benign noble gases like Xe depends on new materials which have quantum yield more than 100% . This can be achieved through quantum-cutting [15].

2.2.3.2 Bio-photonic applications

Rare-earth ions doped nanophosphors can be used to understand the molecular level biological system. RE ions doped nanomaterials are much superior to the organic and semiconductors based nanoparticles for biological applications due to their (semiconducting + organic) high energy excitation, low tissue penetration and inherent toxicity. There are numerous applications of trivalent RE ions doped nanomaterials in biological systems especially

upconverting nanomaterials. Herein, we have discussed major applications such as photodynamic therapy, detection of other biological species via FRET and biological imaging under in vivo and vitro conditions [1,2].

Photodynamic therapy:

Currently, photodynamic therapy (PDT) is substantially practiced for the killing of infected cells in which the infected cells are irradiated with high energy radiation to generate the highly reactive species (O· free radical from O_2 molecules) from biological surrounding (Fig. 6). Later, this reactive species (O·) can interact with the infected cells to kill them [1,2]. This PDT technique consisted of three parts: light source, photosensitizers and reactive species. Judicious selection of all these three component of PDT is vital. For example, $NaYF_4$: Yb with co-doped RE^{3+} (Er/Tm) ions and combination with other nanomaterials is used now[1,2,4].

FRET-based biological sensing:

FRET (Förster Resonance Energy Transfer or Fluorescence Resonance Energy Transfer) is another method to get the information of the biological system. Using this, molecular distance between the donor and acceptor molecules is determined and typically, it is taken place when the distance between acceptor and donor distance is less than 10A°. In other word, it can be said that it is "nanoscopic ruler" to measure the separation between acceptor and donor molecules. The efficiency of FRET is inversely dependent on the sixth power of separation between acceptor and donor and can be expressed as [24]:

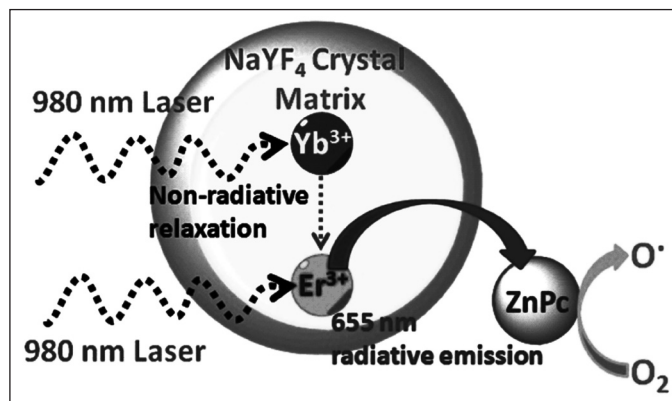$$K_{(T)}(r) = \frac{1}{\tau_d}\left(\frac{R_o}{r}\right)^6 \tag{1}$$

Fig. 6: *PDT application of RE^{3+} ions doped nanomaterials*

Where, r is the distance between acceptor and donor, $K_{(T)}$ (r) is rate of energy transfer, τ(d) is the life time of donor without acceptor and R_o is Förster distance which is typically in the range of 20-60Aº. This nanoscale level process occured due to dipole-dipole interactions between the donor and acceptor and overlapping of emission energy of donor and aborption energy of acceptor and size of nanoparticles [25]. FRET is applied for studying the wide range of nanoparticles including the dye-labelled bio-molecules, dyes and quantum dots (QDs). Coupling with other nanoparticles such as gold (plasmonic material) and Fe_2O_3 (magnetic material), UC nanoparticles have been accepted as good candidate as FRET based bio-sensor [1,2,4]. For instances, Xu *et al.* prepared FRET biosensor using the PEI modified $NaYF_4$:Yb^{3+}/Tm UCNPs as donor and CdTe quantum dots (QDs) capped with thioglycolic acid (TGA) as an acceptor to detect the lead (Pb^{2+}) in the human serum [26]. On other hand, cubic $NaYF_4$:Ce/Tb biotinylated nanocrystals was used as TR-FRET (Time-Resolved Fluorescence Resonance Energy Transfer) probes to detect the trace amount of avidin in the detection limit of 5nM [27].

In vivo and in vitro bio-imaging:

In vivo is fundamentally concerned to study the effect of biological entities (cells, tissues, antibodie, peptides etc.) in natural or within the living system while in vitro, biological entities are studied in simulated eniviroment in which all the essential components are available for the growth of that biological entities. Usually upconvereting RE^{3+} ions doped nanoparticles are considered as a good candidate for applications in *in vivo* and *in vitro* bio-imaging [1-2,4].This is due to the sharp emission-band, large anti-stokes shift, chemically stable, and resistant to photobleaching etc. However, the major issue is they are water insoluble. Therefore, to increase the water solubility and biocompatibility, upconconevrsion nanoparticles surfaces are funtiontionlized with silica coating (Stober's method). For instance, Zhan et al. used the 915 nm laser for exciting the upconverting nanoparticles (UCNPs) $NaYF_4$:Yb^{3+} doped with Tm/ Er/ Ho [28] and studied the both *in vitro* and *in vivo* bio-imaging. First, for in vitro imaging, functionalized UCNPs was conjugate with antibodies and then incubated into the HeLa cancer cell line. On the other hand, in vivo imaging , being hydrophilic, biocompatible and stable the UCNPs was coated with DSPE-mPEG-5000 molecules [28].

3. Semiconducting nanomaterials and their application as catalyst/photocatalyst

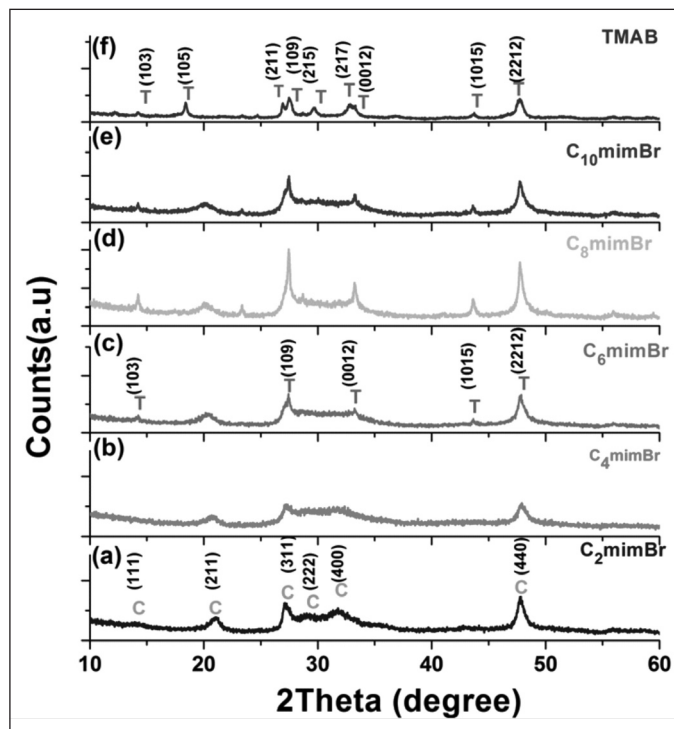**3.1. Influence of ionic liquid on the size, morphology and phase of the semiconducting nanomaterials**

Fig. 7: PXRD patterns of the as-prepared indium sulphide nanocrystals using different ionic liquid a) [C_2mim] Br, b) [C_4mim]Br, c) [C_6mim] Br, d) [C_8mim]Br, e) [$C_{10}mim$]Br, and f) TMAB

As ILs can act as templating and capping agent and in addition, it has tunable physical properties like solubility, concentration, polrarity, viscosity, varied cation/anion combinations; ILs can be effectively used to prepare semiconducting materials which have several applications in optoelectronic, magnetic, photocatalysis, solar cell etc. [29-39].

Recently Ghosh and co-workers elucidated the role of imidazolium based ILs ([C_nmim] Br, n=2, 4, 6, 8, and 10 and Tetramethyl ammonium bromide (TMAB)) in the crystal phase tuning from cubic to tetragonal form of indium sulphide nanoparticles synthesized through ILs assited solvothermal method [10]. On changing the pendant alkyl chain length of imidazolium-based ILs, different phases of In_2S_3 nanoparticles were evolved under same experimental conditions (as shown in Fig. 7). For short alkyl chain length (n=2 and 4) pure cubic phase is appeared (Fig. 7a and 7b). However, on increasing the alkyl chain length (n= 6, 8 and 10) tetragonal phase appeared (Fig. 7c, 7d, and 7e). In addition, pure tetragonal phase was noticed on using the TMAB IL (as shown in Fig. 7f) which devoids of aromaticity. Normally, ILs can be attached at the particular site of nucleation and can govern the crystal growth by three probable ways: **a)** by π-π interaction between aromatic ring systems **b)** hydrogen bonding between the initial nuclei facets and the H atom in C(2) position of [C_nmim]$^+$ and **c)**

steric crowding due to the alkyl chain length of the ILs on either of nitrogen in imidazolium ring system. Analysis of this particular case reveals that the evolution of the phase is not affected by H-bonding rather $[C_2mim]^+$ ions are anchored on a particular plane via the π-system.[10] It is laso seen that by tuning the alkyl chain length of imidazolium-based IL different morphologies are observed (as shown in figure 8a-f).[10] It is found that the formation and assembly of the nanoflakes are different for different ILs employed for the synthesis of indium sulphide nanoparticles. For the ILs with small alkyl chain length ($[C_2mim]Br$ and $[C_4mim]Br$), nanoflakes are assembled in form of spherical structure. However, nano-sheet like structure was found in the IL having longer alkyl chain length ($[C_6mim]Br$, $[C_8mim]Br$, $[C_{10}mim]Br$) [10].

Moreover, rutile and rutile-anatase phases of TiO_2 were tuned by employing $[C_2mim]Br$ IL and it was noticed that the evolution of pure phase was dependent on the content of IL [31]. In addition, capping nature of IL was nicely supported when different size (anatase nanoparticles was 4-6 nm and rutile nanorods was found of 3-6 nm in diameter and 20-60 nm in length) and

shape of nanoparticles were originated [31]. Wang *et al.* found that change in morphology from nanoparticles to nanorods and then to nanowire for ZnO nanoparticles was dependent on alkyl chain length (C-1) and proton at C-2 position of imidazolium ILs ($[C_2mim]BF_4$, $[C_4mim]BF_4$ and $[C_2dmim]BF_4$) [32]. Additionally, Qi et al. used the $[C_3mim]$ Br IL as stabilizing agent and template for the synthesis of the ring-ZnO nanoparticles via hydrothermal method [33]. However Lian et al. prepared the α-Fe_2O_3 nanoparticles with various morphologies (mesoporous hollow microspheres, microcubes, and porous nanorods) using the [bmim]Cl [34].

3.2. Optical property of semiconductors nanomaterials

It is well known that optical property of the semiconductor nanomaterials is very much dependent on the size of nanomaterials due to quantum confinement (Fig. 9). In other words, on changing the size of the semiconducting nanomaterials using the ILs, band gap can be effectively tuned [35,36]. By irradiation of the materials of particular wavelength, after absorbing the energy, electron is excited from the valance band (VB) to conduction band (CB) and the hole is lef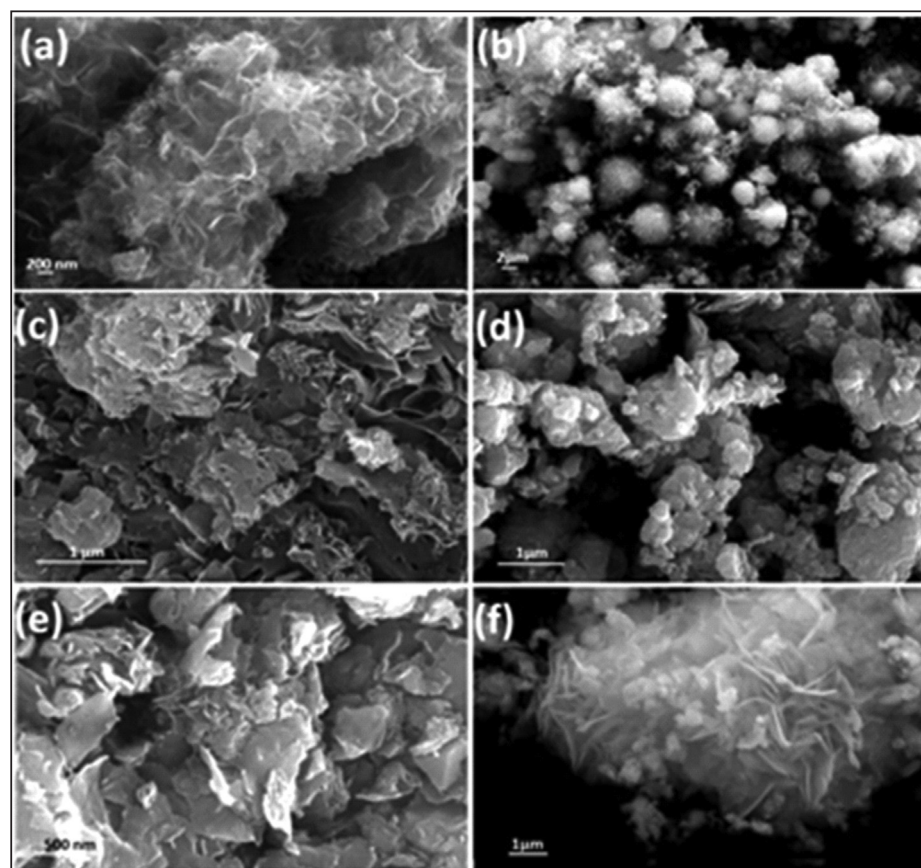t into the VB. When electron and hole is again recombined together, emission of energy either in form of light is taken place [35,36]. Wang et al. obtained the various morphologies (nanoparticles, nanorods and shorter nanorods) using the different ILs and reaction conditions. Subsequently, morphology dependent luminescence property in ZnO was noticed [32]. It was found that on excitation of ZnO at 325 nm, strong and broad green emission peak appeared about 555 nm due to the recombination of electron and photo-excited holes. Further, this green emission was observed stronger for the nanoparticles than the nanorods and shorter nanorods of ZnO [32]. On the other hand, morphology (discs, rings and tubes) dependent tuning of photoluminescence property of ZnO was also reported by Qi et al. in which morphology was tuned by varying the concentration of IL ($[C_3mim]$ Br) [33]. Here, intensity of photoluminescence was observed higher in ring ZnO nanoparticles than the tubes and discs. This was attributed to the increase in the intrinsic defect such as oxygen
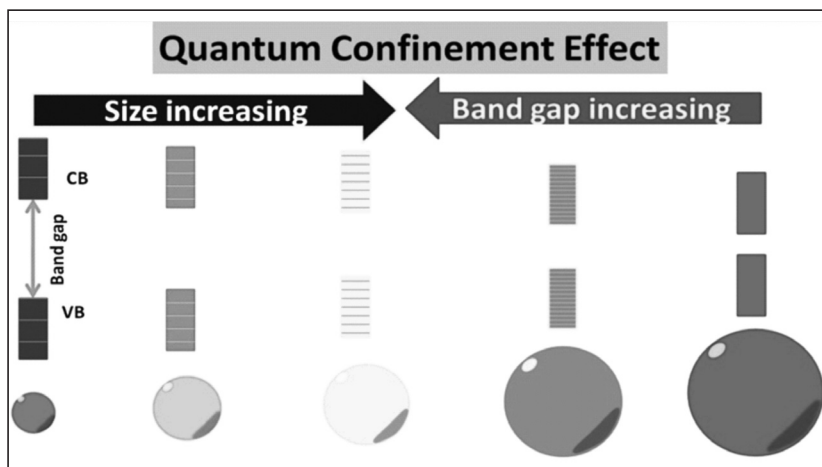

Fig. 8*: FESEM images of indium sulphide nanoparticles synthesized using the different ionic liquids: a) [C₂mim]Br, b) [C₄mim]Br, c) [C₆mim]Br, d) [C₈mim]Br, e) [C₁₀mim]Br and f) TMAB.*

Fig. 9: Schematic representation of size dependent change in band gap of semiconductors

vacancies and/or zinc deficiency [33]. Sharma et al. [10] illustrated the tuning of band gap (2.01 -2.41 eV) of the In_2S_3 by varying the alkyl side chain length of the imidazolium based ILs. Indium sulphide nanoparticles synthesized using the smaller alkyl chain IL ([C_2mim]Br, [C_2dmim]Br, and [C_4mim]Br have shown high band gap as compared to the nanoparticles synthesized using longer alkyl chain containing ILs ([C_8mim]Br and [C_{10}mim]Br) [10].

3.3 Semiconducting nanomaterials as catalysis/ photocatalysis

Recently, applications of semiconductor nanomaterials as catalyst/photocatalyst draw a huge attention. Photocatalysis using semiconducting materials are discussed below in brief [10,29,37-39]
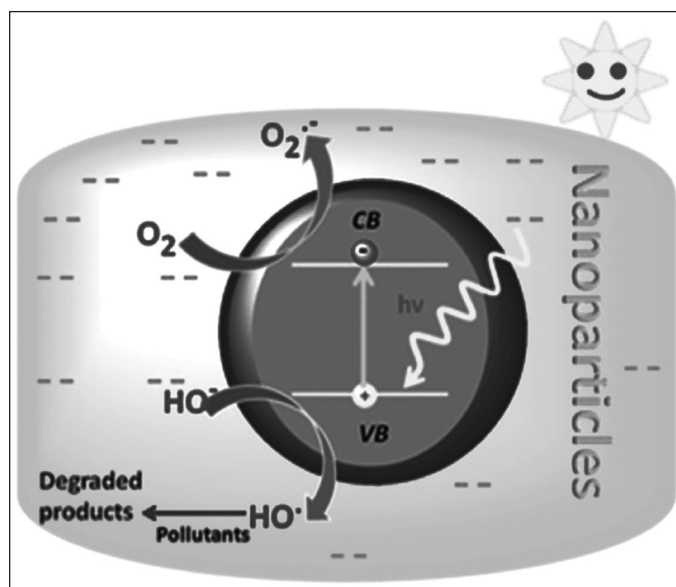

Fig. 10: Schematic representation of photocatalysis of pollutants by nanoparticles.

3.3.1 Mechanism of photocatalysis

Photocatalysis, in general, is the process in which reaction is catalyzed in the presence of light. But the major utility of this process relies on degradation of the organic pollutant especially organic dyes from the water bodies either in the presence of ordinary light or sunlight and phtotcatalytic hydrogen-evolution activity [10,37]. Organic dyes (methyl orange, methylene blue, rhodamine, crystal violet etc.) which are extensively used in the textile, paper, food, etc. as a coloring agent, are directly discarded into the water resources such as ponds, lakes, rivers etc. leading to the severe pollution of these resources which cause serious diseases. Normally in photocatalysis, upon irradiating light onto the nanoparticle, electron is excited from the valance band (VB) to the higher energy level conduction band (CB); hydroxyl ion (OH-) of water donate the excess electron to the VB and being converted into reactive hydroxyl free radical (OH.) which on further reaction with pollutant leading to degradation into the organic pollutant (Figure 10). On the other hand, dissolved O_2 accept the electron from the CB to transform into superoxide free radical (O_2.) [10, 29].

3.3.2 Some examples of photocatalysis using semiconductors

Now-a-days, semiconductors based nanomaterials are extensively used as a photo-catalysts such as ZnO, In_2S_3, CdS, Cu_2S etc. Amongst them, TiO_2 is one of the highly prominent photo-catalyst to date. Although, there are various factors that govern the photocatalytic activity of semiconductor-based nanomaterials, most common factors are specific surface area, morphology, band gap and dye-photocatalyst interaction [29,10, 32,38]

Alammar et al. depicted that efficient photodegradtion (95%) of methyl orange using ZnO nanoparticles synthesized by [C_{10}mim][Tf_2N] [38]. Same group also studied the phase dependent degradation of methyl orange in the presence of TiO_2 nanoparticles synthesized using the different ILs (such as [N_{1888}][Tf_2N], [C_4mim][Tf_2N] [P_{66614}][Tf_2N], [C_3mimOH][Tf_2N] and [C_4Py][Tf_2N]) [39]. They found that mixed phase (anatase+brookite) TiO_2 nanoparticles obtained by ([N_{1888}][Tf_2N], [C_4mim][Tf_2N] [P_{66614}][Tf_2N] shows better photocatalytic activity (>98%) than that of pure phase (anatase phase) TiO_2 nanoparticles ([C_3mimOH][Tf_2N] and [C_4Py][Tf_2N]) under the similar experimental conditions. It can be attributed to the surface area of the TiO_2 nanoparticles [39]. Morphology dependent photocatalytic degradation of rhodamine B was observed with ZnO nanomaterials. It is noticed that uniform grain

size and homogenously long, thin 1D ZnO nanoparticles were showing the better photocatalytic activity.[32] In addition, Sharma et al. [10] illustrated the adsorption controlled photocatalysis of crystal violet dye using In_2S_3 nanoparticles synthesized by different ionic liquids. In_2S_3 nanoparticles synthesized by TMAB (teramethyl ammonium bromide) ILs have shown the maximum photocatalytic efficiency (94.8 %) and it was attributed to highest adsorption of dye which occurred in dark [10].

4. Conclusion

In conclusion, IL based synthesis has tremendous potential in materials synthesis due to their superior properties compared to normal organic solvent and templating agents like long chain amines etc. As there exists 10 [18] possible cation/anion combination for ILs, ILs can be designed in such a way that not only 12 basic principles of "green chemistry" will be followed but also these can act as "designer" solvents for the synthesis of nanoparticles. By tuning the basic properties of ILs like alkyl side chain length, counter ions, concentration, viscosity etc. basic properties of the host materials (both for rare-earth doping and semiconductor itself) like crystal phase, morphology, lattice strain, size can be tuned which eventually tune the optoelectronic properties of the materials.

Acknowledgement

References

1. S. Gai,C. Li,P. Yang, J. Lin, *Chem. Rev.,* **2014**, *114* , 2343.

2. R. K. Sharma, A.-V. Mudring, P. Ghosh, *J. Lumin.*, **2017**,*189*, 44.

3. C. Lorbeer, J. Cybinska, E. Zych, A.-V. Mudring, *Opt. Mater.*, **2011**, *34* 336.

4. J.-C. G. Bünzli, *Chem. Rev.*,**2010**,*110,* 2729.

5. P. Ghosh, R. K. Sharma, **Y.** N. Chouryal, A.-V. Mudring, *RSC Adv.,* **2017,** 7, 33467.

6. P. Ghosh, A. Patra, *J. Phys. Chem. C*, **2008**, *112*, 19283.

7. J. A. Dahl, B. L. S. Maddux, J. E. Hutchison, *Chem. Rev.*, **2007**, *107*, 2228.

8. T. Welton, *Chem. Rev.*, **1999**, *99*, 2071.

9. P. Bonhoˆte, A.-P. Dias, N. Papageorgiou, K. Kalyanasundaram, M.Gratzel, *Inorg. Chem.*,**1996**, *35*, 1168.

10. R. K. Sharma,Y. N. Chouryal,S. Chaudhari,J. Saravanakumar, S.R. Dey, P. Ghosh, *ACS Appl. Mater. Interfaces*, **2017**, *9*, 11651.

11. P. Ghosh, S. Tang, A.-V. Mudring, *J. Mater. Chem.*,**2011**, *21*, 8640.

12. C. Lorbeer, J. Cybinska, A.-V. Mudring, *J. Mater. Chem. C*, **2014**, 2,1862

13. C. Lorbeer, F. Behrends, J. Cybinska, H. Eckertbd, A.-V. Mudring, *J. Mater. Chem.C*, **2014**, 2, 9439.

14. C. Lorbeera, A.-V. Mudring, *Chem. Commun.,* **2014**, 50, 13282-13284

15. P. Ghosh, A.-V. Mudring, *Nanoscale*, **2016**, *8*, 8160.

16. X. Liu, J. Zhao, Y. Sun, K. Song, Y. Yu, C. Du, X. Kong, H. Zhang, *Chem. Commun.*,**2009**, 6628.

17. C. Chen, L-D. Sun, Z-X. Li, L-L.Li, J. Zhang, Y-W. Zhang, C-H. Yan, *Langmuir*,**2010**, *26*,8797.

18. C. Mi, Z. Tian, C. Cao, Z. Wang, C. Mao, S. Xu, *Langmuir*,**2011**, *27*, 14632.

19. J. Chen, C. Guo, M. Wang, L. Huang, L. Wang, C. Mi, J. Li, X.Fang, C. Mao, S. Xu, *J. Mater. Chem.*,**2011**, *21*, 2632.

20. S. Nishiura, S. Tanabe, K. Fujioka, Y. Fujimoto, *Opt. Mater.*,**2011**, *33*, 688.

21. A. Kitai, Luminescent Materials and Application, John Wiley & Sons Ltd., West Sussex, England, **2008**.

22. A. Shalav, B.S. Richards, T. Truppe, K.W. Krämer, H.U. Güdel, *Appl. Phys. Lett.*,**2005**, *86* 013505.

23. G. Chen, H. Ågren, T.Y. Ohulchanskyy, P.N. Prasad, *Chem. Soc. Rev.*,**2015**, *44*, 1680.

24. P. Mahata,S. K. Mondal, D. K. Singha, P. Maje, *Dalton Trans.*, **2017**, 46, 301.

25. V. Muhr, C. Würth, M. Kraft, Markus Buchner, Antje J. Baeumner, Ute Resch-Genger, T. Hirsch *Anal. Chem.*, **2017**, *89* , 4868.

26. S. Xu, S. Xu, Y. Zhu, W.Xu, P. Zhou, C. Zhou, B. Dong, H. Song, *Nanoscale*, **2014**,*6*, 12573.

27. D. Tu, L. Liu, Q. Ju, Y.Liu, H. Zhu, R. Li, X. Chen, *Angew. Chem. Int. Ed.*,**2011**, *50*, 6306.

28. Q. Zhan, J. Qian, H. Liang, G.Somesfalean, D. Wang, S. He, Z. Zhang, S. Andersson-Engels, *ACS Nano*, **2011**,*5*, 3744

29. A. B. Djuriˇsi´c, Y. H. Leunga, A. M. C. Ng, *Mater. Horiz.*,**2014**, *1*, 400.

30. M. Antonietti, D. Kuang, B. Smarsly, Y. Zhou, *Angew. Chem. Int. Ed.*,**2004**, *43*, 4988.

31. W. Zheng, X. Liu, Z. Yan, L. Zhu, *ACS Nano*, **2009**, 3, 115.

32. L. Wang, L. Chang, B. Zhao, Z. Yuan, G. Shao, W. Zheng, *Inorg. Chem.*, **2008**, *47*, 1443.

33. K. Qi, J.Yang, J.Fu, G. Wang, L. Zhu, G. Liu, W. Zheng, *CrystEngComm*, **2013**, 15, 6729.

34. J. Lian, X. Duan, J. Ma, P. Peng, T. Kim, W. Zheng, *ACS Nano*, **2009**, 3,3749.

35. A. P. Alivisatos, *Science*, **1996**, *271*,933.

36. H.Yu, J. Li, R. A. Loomis, L.-W. Wang , W. E. Buhro, *Nat. Mater.*, **2003**,*2*,517.

37. V. W-h. Lau, L. G. A. van de Water, A. F. Masters,T. Maschmeyer, *Chem. Eur. J.*, **2012**, *18*, 2923.

38. T. Alamar, A.-V. Mudring, *ChemSusChem,***2011**, *4*, 1796.

39. T. Alamar, H. Noei, Y. Wang, A.-V. Mudring, *Nanoscale*, **2013**, *5*, 8045.

	Mr. Rahul Kumar Sharma *is currently pursuing his PhD in the Department of Chemistry, Dr. Harisingh Gour Central University, Sagar, Madhya Pradesh after completing his M.Sc in Chemistry from Jiwaji University Gwalior, Madhya Pradesh. His area of interest is to design the semiconducting, rare-earth doped and graphene based optoelectronic nanomaterials using Ionic Liquids (ILs).*
	Yogendra Nath Chouryal *has joined as a Junior Research Fellow on SERB-DST Project in Dr. Harisingh Gour Central University Sagar, Madhya Pradesh in the year 2015 after completing his M.Sc. from the same institute. He is working on Optoelectronic nanomaterials by using different kinds of task specific Ionic Liquids (ILs).*
	Dr. Pushpal Ghosh *has done Ph.D at Indian Association for the Cultivation of Science, Kolkata (Degree given by Jadavpur University), M.Sc. from Presidency College, Kolkata (University of Calcutta) and B.Sc with Honours in Chemistry from Ramkrishna Mission Residential College Narendrapur, Kolkata (University of Calcutta). He is a recipient of prestigious Alexander von Humboldt Fellowship (AvH) given by Alexander von Humboldt Foundation, Germany and worked in Ruhr University Bochum, Germany from December 2009 to October 2013. Then he joined as an Assistant Professor in Dr. H.S. Gour Central University Sagar, Madhya Pradesh. Currently he is leading a research group funded by UGC Start-Up grant, SERB-DST (Young Scientist) award and BRNS. His interest is to explore new generation optoelectronic nanomaterials using ionic liquid based green synthesis.*

Simple Perspectives of Sugar Based Gel Chemistry

Rathinam Periyasamy, Kamalakannan Soundarajan and Thangamuthu Mohan Das*
Department of Chemistry, School of Basic and Applied Sciences, Central University of Tamil Nadu,
Neelakudi campus, Thiruvarur-610 005, India
* E-mail: tmohandas@cutn.ac.in.

Abstract

This review is aimed at bringing the most fundamental aspects of sugar based gel chemistry, at an elementary level, that can serve the needs of the researcher who are working in this area of gel chemistry. Therefore, this article is conveniently divided into five broad sections. Thus the first section deals with some introductory aspects such as What is a gel?, weak interactions responsible for gelation and importance of gel chemistry. On other hand, the section two deals with the rational design of gelators which gives some basic idea to the researchers while designing gelators. The third section, on the other hand deals with the available advanced characterization techniques such as XRD, SEM and TEM for gels. The fourth section consists of the synthesis, morphology of the self-assembly and their material applications of different sugar based gelators reported from our laboratory. The fifth section describes the future perspectives in this area of research.

1. Introduction

Nowadays the gels and their derivatives are found to be attractive candidates for a variety of applications such as, the design and synthesis of biomaterials, nano-materials, stimuliresponsive materials, sensors, and templating components for inorganic and organic nanostructures, and catalysis [1]. LMWGs can remediate unwanted pollutants from the environment including: immobilisation of oil spills, removal of dyes and the detection or removal of chemical weapons. Selective gelation mediated oil removal process involves solidification of the oil in form of gel by gelator followed by removal of the oil swollen gel through physical process such as filtration. From this, it is clear that LMWGs have genuine potential for oil spill remediation [2]. Therefore, this article is conveniently divided into five broad sections. Thus the first section deals with some introductory aspects such as What is a gel?, weak interactions responsible for gelation and importance of gel chemistry. On other hand, the section two deals with the rational design of gelators which gives some basic idea to the researchers while designing gelators. The third section, on the other hand deals with the available advanced characterization techniques such as XRD, SEM and TEM for gels. The fourth section consists of the synthesis, morphology of the self-assembly and their material applications of different sugar based gelators reported from our laboratory. The fifth section describes the future perspectives in this area of research.

2. Gels

In general, gel is a substantially diluted system which exhibits no steady state flow [3]. Based on the combined microscopic and macroscopic properties, a substance can be classified as a gel, if it: (i) has a continuous microscopic structure with macroscopic dimensions that is permanent on the time scale of an analytical technique and (ii) is solid-like in its rheological behavior despite being mostly liquid [4]. Molecular self-assembly is a very common phenomenon present in nature, and is also whispered to play a vital role in several events such as the emergence, conservation, and encroachment of life [5]. While the several of the researchers are mainly focusing on molecular self-assembly which centers around the biomacromolecules (proteins, nucleic acids, and polysaccharides). However, the self-assembly of small molecules in water or an organic solvent also has insightful inferences from fundamental science to practical applications [6]. A subclass of these small molecules is called "gelators" because one usual and also important consequence of the self-assembly of such small molecules is the formation of a gel or gelation. Depending upon the nature of the solvents in which it forms gel, these small molecules are further classified as hydrogelators (water as the liquid phase) and organogelators (organic solvent as the liquid phase) [7]. Thus the gelators self-assemble in solvents to form three-dimensional supramolecular networks that encapsulate a large amount of solvents to afford a gel [8]. Unlike the conventional polymeric gels that are mainly based on covalently crosslinked networks of polymers (i.e., gellant), the networks in supramolecular gels are formed due to noncovalent interactions

---

This Article is dedicated to Prof. C. P. Rao, Department of Chemistry, Indian Institute of Technology Bombay, Mumbai-400 076, India.

(**Figure 1**) between the gelators such as hydrogen bonds, π–π stacking, van der Waals interaction, solvophobic effects, metal–ligand coordination, charge-transfer interactions ionic, and hydrophobic interactions, to form athixotropic matrix [9].
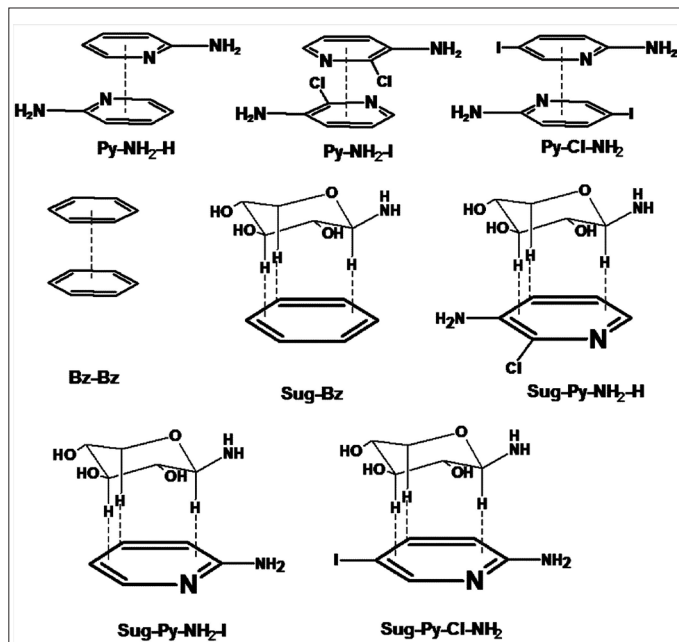

Fig. 1: Various possible noncovalent interactions between the gelators[10].

2.1 Sugar based gels

Sugars are one major class of biological macromolecules that serve organisms as energy sources particularly through glucose which is a monosaccharide. Due to biodegradable, non-toxic and eco-friendly nature, the self-assembly of sugar-derived Low Molecular Weight Gelators (LMWGs) has received more attention and this makes them perfect building blocks for the regeneration of several bio species such as, tissues and organs [11]. In general the precursors for the synthesis of sugar-derived

LMWGs are inexpensive and also commercially available. They may be derived from several abundant renewable resources. Significant amount of established synthetic strategies are known in the literature to construct various building blocks made of biocompatible monosaccharides, disaccharides or polysaccharides for gelation [12]. Thus, with the available literature, one can have broad classes of LMWGs derived from these carbohydrates. Comparison between the completely protected sugars with that of simple unprotected sugar reveals that the former has more of hydrophobic nature while the latter has more hydrophilic character **(Table 1)**.

The chemical structures of partially protected **1**, unprotected **2** and fully protected **3** sugars are given in the Fig. 2. Due to these extremely only one characteristics, self-assembly is not possible in these cases. While my research group is working on synthesis of partially protected sugar, we have observed a selective protection of two hydroxyl groups results in the balanced amount of both hydrophobic and hydrophilic characteristics. Out of the several partially protected monosaccharide derivatives, our research group observed a significant amount of self-assembly with the 4- and 6- protected monosaccharides and it has become reported in the literature [13].

3. Rational design of gelators

Although the chemical structure of many of the gelators that are reported in the literature looks rather simple, it is very difficult to predict the gelating ability based on structure. In most of the cases, the research findings were serendipity in nature. So, the information obtained from a variety of diverse types of gelators helped us to rationalize the structural requirements for molecules to act as gelators. Though several research groups made attempts to rationalize the structure of gelator molecules, still the rational design of small molecular gelators has remained elusive [14]. It has been proven that the presence

Table 1: Comparison of properties of partially protected 1, unprotected 2 and fully protected 3 sugars.

| Properties	Parially protected Saccharide	Saccharide	Fully protected Saccharide
Hydrophilicity	Partially hydrophilic & partially hydrophobic	Hydrophilic	Hydrophobic
Solubility	Sparingly soluable or insoluable	Soluable in water	Soluable in organic Solvents
Noncovalent interactions	Hydrogen bonding, van der Waals, pi-pi interactions etc.,	Hydogen bonding interactions	Not hydrogen bonding Interactions
Slf-assembly behaviour	Self assemble easily	No self assembly	No self assembly
Gel forming capacity	Forms gel	Does not form gel	Does not form gel (depending upon R group)
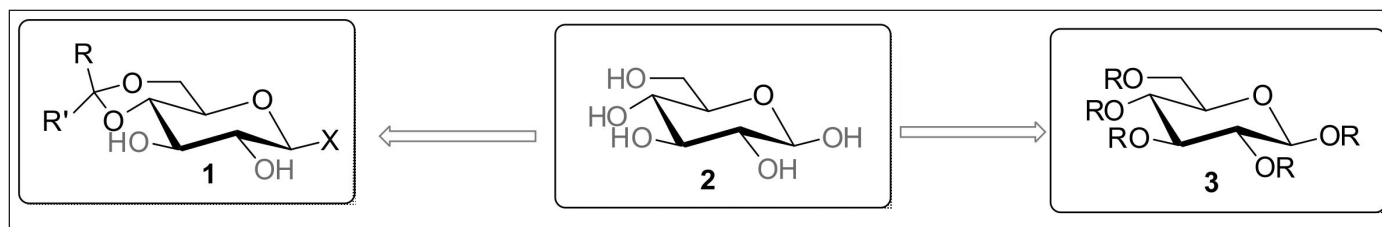
*Fig. 2: Structures of partially protected **1**, unprotected **2** and fully protected **3** sugars.*

of functional groups which are capable of forming hydrogen bonds such as amide, carboxylic acid, urea and hydroxyl are crucial for gelators [15]. In addition to these, the directionality, specificity and rigidity of multiple hydrogen bonding interactions is expected to help spatial arrangement of functional chromophores in achieving efficient gelation. It is also observed that the functional groups such as, amino acids, cholesterol, peptides, sugar, cyclohexyl amine, oligoethylene chains who are found to increase the gelating ability in a variety of solvents [16] and in these cases, hydrophobic interactions plays a vital role, some of the weak interactions such as, pi-pi, van der Waals forces of interactions are also play important role in the self-assembly [17]. Molecules that enable donor−acceptor and dipole−dipole interactions can also lead to the gelation of solvents [18]. The presence of long hydrocarbon chains with a certain ideal chain length is also an important structural requirement because the alkyl chains facilitates van der Waals interaction of gelator molecules [19]. In most of the cases, more than one structural requirement is needed for the design of gelator molecules, but exceptions are also available in the literature. We also made an attempt to rationalize the design of sugar based gelator and it is given in the **Figure 3a**. Chemical structures of some Structures of urea [20] based **4**, amino acid [21] based **5** and azobenzene [22] based **6** gelators which have been reported in the literature are given in the **Figure 3b**. The presence of difference segments which are capable of forming hydrogen bonding, π−π stacking and dipole-dipole interactions is an important factors for the gelators reported from our group. In another case, we have proved that the presence of halogen-halogen interaction resulted in gelaton [23].

4. Advanced Characterization Techniques for Gels

The amplified number of gelators and the necessity of more information on supramolecular gels at both the nanoscale and molecular levels need more accurate
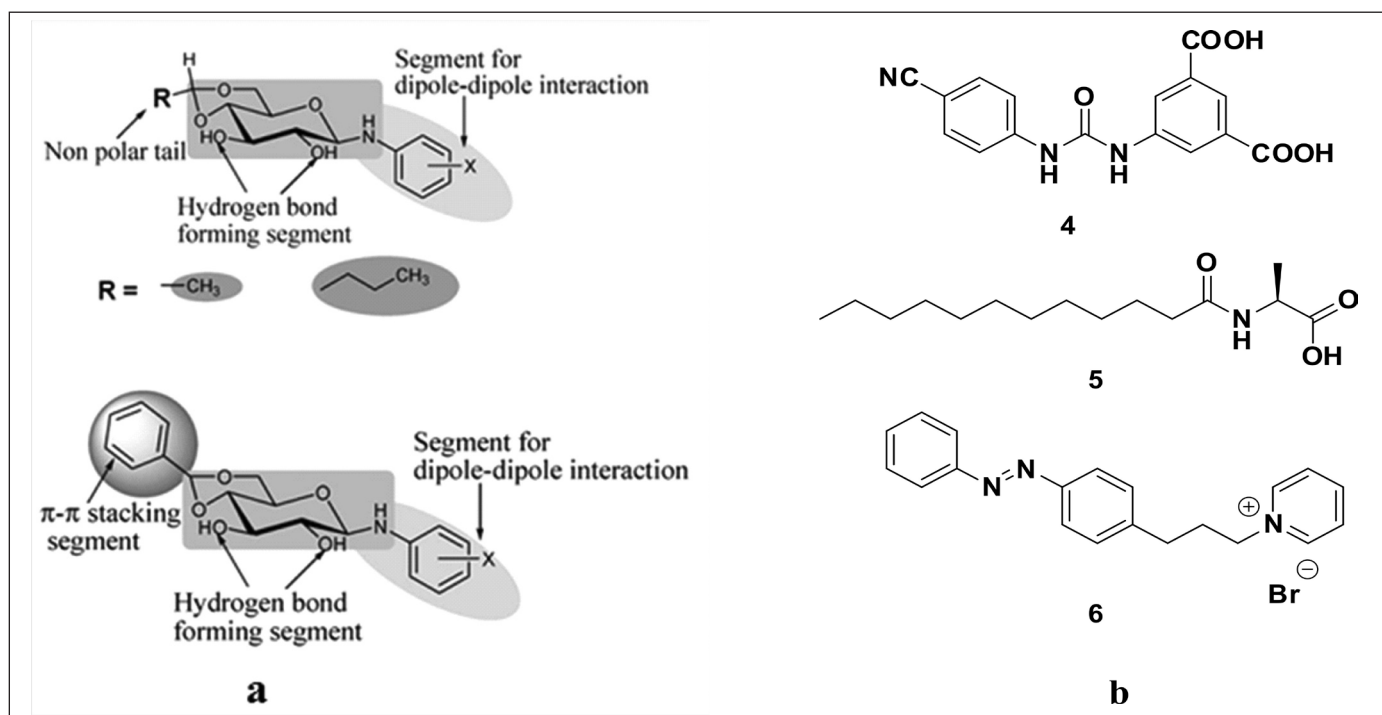

*Fig. 3: (a) Rationalization of different groups responsible for gelation in different N-glycosylamines [11]; (b) Structures of gelators based on urea [20] **4**, amino acid [21] **5** and azobenzene [22] **6** gelators reported in the literature.*

analysis and characterization of the gels. There are numerous techniques available to do these tasks. These techniques vary from very simple "naked eye" technique to highly sophisticated microscopic techniques and they have been classified into five types are visual inspection, microscopy techniques, rheometry and Differential Scanning Calorimetry(DSC), X-ray diffraction and. spectroscopic methods [12]. From these available techniques, suitable and sufficient characterization methods can be carefully employed, by understanding the gelation mechanisms and influencing factors of gels, to make full use of their respective advantages and better investigation of these materials.

5. Sugar based derivatives as gelators

Several of the sugar derivatives such as, are shown to form gelation in variety of solvents. Details about the molecular structures (Fig.4) gelation and gels are given below.

A novel class of N2-/N3-(β-D-glucopyranosyl)-2-/3-aminoquinoline derivatives **7** have been done and reported from our research group [24]. The gelation test has showed that these derivatives form gel with a wide range of polar and nonpolar solvents. Morphology of these amphiphilic gels were studied using SEM, HR-TEM microscopic techniques. DSC and powder XRD analysis have been done to understand thermal and structural properties. The microscopic studies confirm the formation of fibrous structures by the self-assembly behavior of these molecules and it is due to the influence of organic solvents. It is clear that hydrogen bonding and van der Waals interactions are playing an important role in the self-assembled structure.

In another report our research group has reported synthesis of a novel class of six different triaryl pyridine *N*-glycosylamine amphiphiles **8** and their characterization based on different spectral techniques [25]. Gelation properties in different aromatic and aliphatic solvents have been studied and gelation was witnessed predominantly in aliphatic solvents with CGC of 0.5% (w/v). FE-SEM and powder XRD techniques revealed fibrous entanglement of the molecules in the gel state with intermolecular spaces of 3.62 nm and 0.43 nm.

Simple aldol condensation of β-C-glycosylketones with rhodamine core molecule containing aldehyde group under ambient reaction conditions yielded the corresponding β-C-glycosides **9** in good yields and the product formation was confirmed through different spectral techniques [26]. Gelation properties of these compounds were examined and their self-assembled nanostructures were analysed by HRTEM, FESEM, DSC, rheological and powder XRD techniques.

Reaction between rhodamine and different sugar derivatives, resulted in the formation of rhodamine based *N*-glycosylamines **10** [27]. All the compounds were characterized by using different spectral techniques and by their physico-chemical properties. These molecules self-assemble into different nanostructures in different solvents.

Fluorescence derivatives find lot of applications in the sensor chemistry. Recently, we have reported the synthesis of fluorescein based β-amino glycosyl ketones in the literature. Reaction between fluorescein-monaldehyde and 4,6-*O*-protected-*C*-glycoside in presence of potassium carbonate resulted in the formation of the corresponding glycoside **11** and it is a one-pot synthesis [28]. By using HRTEM, DSC and powder XRD techniques the gelation properties of the compounds were analyzed.

Several β-C-glycosidic ketones **12** were shown to act as amphiphilic in nature [29]. The gelation test disclosed that the mono alkylated β-C-glycosides synthesized were capable of forming gels in the presence of a wide range of solvents at critical gelator concentrations (CGCs) as low as 0.3%. The FE-SEM, TEM and powder XRD analysis showed that the fiber structure obtained on the self-assembly of these compound were transformed into suspension rods under the influence of water. The fibers and the rod-shaped self-assembles formed by these glycosidic ketones have been utilized as templates for the synthesis of mesoporous silica materials.

In general chalcone derivatives are used in the synthesis of several organic molecules. Sugar chalcone derivatives **13** was synthesized from the aldol condensation of various β-*C*-glycosidic ketones with aromatic aldehydes under the basic condition [30]. The corresponding olefinic reduced product was also obtained using Zn-mediated reduction of sugar-chalcone. Few of the sugar-chalcone derivatives were found to be gelators for different solvents, and their morphology was studied using FESEM and HRTEM. From the morphological studies it was found that the nano structures formed by the chalcone derivatives are fibrous network.

A series of α,β-unsaturated-β-*C*-glycosidic ketones **14** were synthesized starting from D-glucose in three steps [31]. Heteroaromatic aldehydes undergoes aldol condensation with 4,6-*O*-butylidene-β-*C*-glycosidic ketones in the presence of a suitable organocatalyst which leads to the formation of glycosydic ketones in stereoselective manner. Hydrogen bonding and π–π stacking of the

reported derivatives were established by single-crystal XRD. It was determined that the soft material derived from this method had a diameter of 10–200 nm with a three-dimensional network by using SEM and HR-TEM.

In one another report alkyl-benzimidazole-carbazole based *N*-glycosylamines **15** were synthesized, confirmed using ^{1}H and ^{13}C NMR spectral techniques and MALDI-TOF and EI-mass analysis [32]. From the ^{1}H NMR analysis of *N*-glycosylamines, the existence of the anomeric proton in *β*-configuration was identified and it was further supported by ^{1}H–^{1}H COSY and 2D-ROESY NMR analysis. All the *N*-glycosylamines were found to be good gelators for aliphatic rather than aromatic solvents. Out of six gelators reported five were recognized as supergelators, since their Critical Gelation Concentration (CGC) is less than 1%. Microscopic analysis proved that *N*-glycosylamines self-assemble into nanofibers.

Benzimidazole based partially protected *N*-glycosylamine amphiphiles **16** possessing different alkyl chains were synthesized in good yield [33]. The identities of the synthesized *N*-glycosylamines were confirmed using ^{1}H and ^{13}C NMR and the molecular mass of representative

samples was confirmed using MALDI-TOF mass analysis. All the benzimidazole based *N*-glycosylamines were found to exist in β-anomeric form, which was confirmed by ^{1}H NMR analysis. Gelation studies proved that these compounds can gelate both aromatic and aliphatic solvents, at a lower CGC of 0.8%. From SEM and TEM microscopic studies the nanostructure of self-assembly was found as nanofibers. This nanofiber structure was converted to nanospheres upon the addition of Cu^{2+} ions.

A sugar-based photoresponsive supergelator, *N*-glycosylazobenzene **17** that shows selective gelation of aromatic solvents is described in another report [34]. The *trans-cis* isomerization of the azobenzene moiety permits photoinduced axing of the entangled gel fibers to short fibers, resulting in controlled fiber length and gel–sol transition. The gelator is found to be useful for the selective removal of toxic aromatic solvents from water.

By applying "Click reaction" a facile regioselective synthesis of bis-triazologlycolipids **18**, a class of organogelators, has been reported from our research group [35]. The morphology and self-assembly nature of the gelators were inspected by FESEM and HRTEM analysis. From these analysis it is confirmed that both

Table 2: General characteristics of the representative examples of sugar based gelators category reported from our research group.

Compound Number	Nature of the solvent used for gelation		Critical Gelation Concentration (w/v %)	Morphology of the gel*	Reference number
7	Polar	Aliphatic	1.0	Fibrous like aggregates	24
8	Polar, Nonpolar	Aliphatic, Aromatic	1.0	Fibrous network	25
9	Nonpolar	Aromatic	1.0	Fibrous network	26
10	Polar	Aliphatic	1.0	Cross-linked nanofibrous	27
11	Polar, Nonpolar	Aliphatic, Aromatic	1.0	Twisted rod	28
12	Polar, Nonpolar	Aliphatic, Aromatic	0.3	Fibers and rods	29
13	Polar	Aliphatic	1.5	Lamellar	30
14	Polar	Aliphatic	0.75	Fibrous and lamellar	31
15	Polar, Nonpolar	Aliphatic, Aromatic	≤1	Nanofibers	32
16	Polar, Nonpolar	Aliphatic, Aromatic	1.0	Nanofibers changed into nanorods on addition of copper ions	33
17	Nonpolar	Aromatic	0.1	Nanofiber networks	34
18	Polar mixture of solvents	Aliphatic	1.0	Fibrous and lamellar	35
19	Nonpolar	Aromatic	1.0	3D fibrous network	23
20	Polar, Nonpolar	Aliphatic, Aromatic	≤1	Nanorods and textured spheroids	36

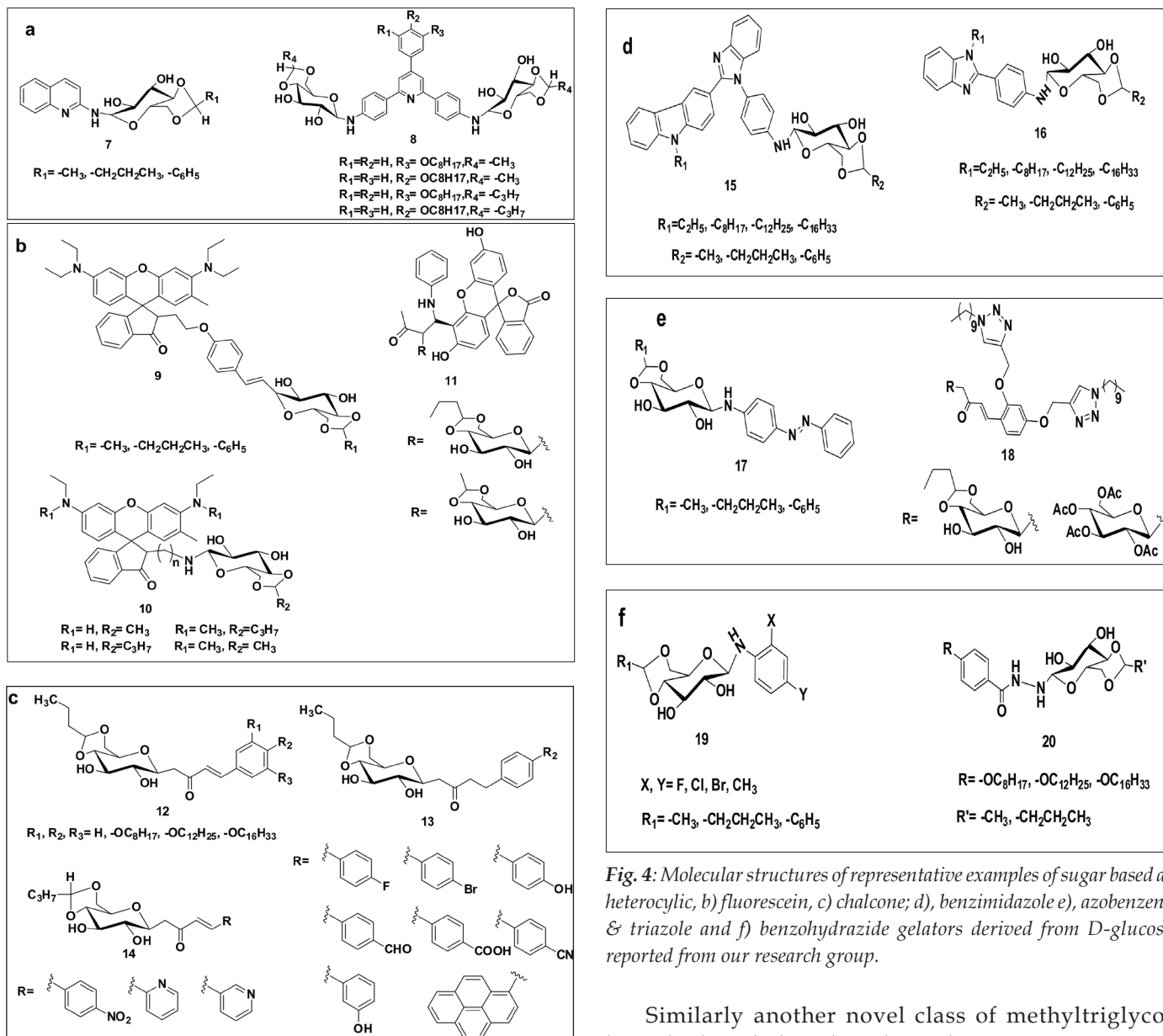**- Identified from the SEM and TEM techniques*

Fig. 4: Molecular structures of representative examples of sugar based a) heterocylic, b) fluorescein, c) chalcone; d), benzimidazole e), azobenzene & triazole and f) benzohydrazide gelators derived from D-glucose reported from our research group.

fibrous and lamellar structures were obtained for the bistriazole derivatives.

A series of *N*-glycosylamine based organogelators **19** were synthesised from three different 4,6-*O*-protected saccharides and corresponding amines [23]. The effect of substituents present in the *N*-glycosylamines on gelation was studied from NMR and computational studies. Among the eighteen different gelators studied, the compound bearing fluorine as a substituent, was observed to gelate at very low concentrations (CGC: 1%). Further, it also revealed that dipole–dipole interactions play an important role in the case of *N*-glycosylamine-based gelators. The presence of π–π stacking and H-bonding, as inferred from the reported X-ray diffraction data, are responsible for the gelation.

Similarly another novel class of methyltriglycol benzohydrazide based *N*-glycosylamines **20** containing long alkyl chain derivatives have been reported in the literature and characterization was carried out by using NMR (^{1}H and ^{13}C) spectral analysis [36]. The gelation test showed that these derivatives form gels with a wide range of polar (1,2-dichlorobenzene, chloroform) and non-polar (1,2-dichloroethane, toluene, benzene) solvents even with lower CGC (1.0%). Morphologies of these amphiphilic glycosidic gels were studied using FE-SEM, TEM and powder XRD analysis. These experiments confirm the formation of 3D self-assembled spherical and rod structures because of the influence of organic solvents.

A correlative table has also been prepared and shown as Table 2 which comprises of different sugar based gelators, their Critical Gelation Concentration (CGC), morphology of the gels and their respective reference numbers.

6. Conclusion

In this review, we have made a journey across various areas of sugar-derived LMWGs studied from our research group, uncovering the rational design of gelators, characterization techniques and beneficial applications, ranging from sensing to their uses as tissue culture media. Easy commercial availability, biodegradability, non-toxic nature and eco-friendly behavior are the most important advantages of using sugar derivatives as a platform of gelation. We have also systematically explored how one may utilize various non-covalent forces to endow the sugar-based LMWGs system with desirable properties. Furthermore, light responsive azobenzene moiety is incorporated in the sugar-derived gelators to develop fascinating stimuli-responsive soft materials and unveil the secrets of various biological phenomena. The gelation ability of sugar-based LMWGs at a reasonably low concentration and their significantly high mechanical strength have proven them to be promising candidates for phase selective gelation.

7. Future perspectives

Since, sugar based glators often lead to the formation of transparent gels with high transmittance in the visible region and glass-like refractive indices, they have promising potential to become glass substitutes as well. The supramolecular gel matrix has been extensively utilized as template for the synthesis and stabilization of different kinds of nanomaterials in order to develop novel nanocomposites with interesting properties but, this field has not adequately explored with sugar-derived gels. One of the promising applications of sugar based gelators is in organic electronics which area needs considerable attention. We believe that this review will become a very useful source for such future design and innovation.

Acknowledgements

References

1. G. Yu, X. Yan, C. Han and F. Huang, *Chem. Soc. Rev.*, **2013**, *42*, 6697-6722.
2. B. O. Okesolaa and D. K. Smith, *Chem. Soc. Rev.*, **2016**, *45*, 4226-4251.
3. S. Z. D. Cheng, S. K. Lee, J. S. Barley, S. L. C. Hsu and F. W. Harris, *Macromolecules*, **1991**, *24*, 1883-1889.
4. R. G. Weiss and P. Te´rech, in Molecular Gels: Materials with Self-Assembled Fibrillar Networks, ed. R. G. Weiss and P. Te´rech, Springer, Dordrecht, The Netherlands, **2006**, 1–12.
5. J. M. Lehn, *Angew. Chem., Int. Ed.*, **1990**, *29*, 1304-1319.
6. X. Du, J. Zhou, J. Shi and B. Xu, *Chem. Rev.*, **2015**, *115*, 13165–13307.
7. P. Terech and R. G. Weiss, *Chem. Rev.*, **1997**, *97*, 3133-3159.
8. Z. Yang and B. Xu, *Adv. Mater.,* **2006**, *18*, 3043-3046.
9. Y. Lan, M. G. Corradini, R. G. Weiss, S. R. Raghavanc and M. A. Rogers, *Chem. Soc. Rev.*, **2015**, *44*, 6035-6058.
10. K. Karthik Kumar, M. Elango, V. Subramanian and T. Mohan Das, *New. J. Chem.*, **2009**, *33*, 1570-1577.
11. J. B. Matson and S. I. Stupp, *Chem. Commun.*, **2012**, *48*, 26-33.
12. S. Dattaa and S. Bhattacharya, *Chem. Soc. Rev.*, **2015**, *44*, 5596-5637.
13. T. Mohan Das, C. P. Rao and E. Kolehmainen, *Carbohydr. Res.*, **2001**, *334*, 261-269.
14. S. S. Babu, V. K. Praveen and A. Ajayaghosh, *Chem. Rev.*, **2014**, *114*, 1973−2129.
15. M. R. Rao and S. S. Sun, *Langmuir*, **2013**, *29*, 15146-15158.
16. M. Suzuki and K. Hanabusa, *Chem. Soc. Rev.*, **2009**, *38*, 967-975.
17. A. Ajayaghosh and S. J. George, *J. Am. Chem. Soc.*, **2001**, *123*, 5148-5149.
18. D. B. Amabilino, D. K. Smith and J. W. Steedc, *Chem. Soc. Rev.*, **2017**, *46*, 2404-2420.
19. S. Miljanić, L. Frkanec, Z. Meić and M. Žinić, *Eur. J. Org. Chem.*, **2006**, 1323-1334.
20. F. Rodrı´guez-Llansola, B. Escuder, J. F. Miravet, D. Hermida-Merino, I. W. Hamley, C. J. Cardin and W. Hayes, *Chem. Commun.*, **2010**, *46*, 7960–7962.
21. S. Bhattacharya and Y. Krishnan-Ghosh, *Chem. Commun.*, **2001**, *0*, 185–186.
22. F. Xie, L. Qin and M. H. Liu, *Chem. Commun.*, **2016**, *52*, 930–933.
23. S. Nagarajan, P. Ravinder, V. Subramanian and T. Mohan Das, *New J. Chem.*, **2010**, *34*, 123-131.
24. K. Soundarajan, R. Periyasamy, P. Muthuvel and T. Mohan Das, *Trends in Carbohydr. Res.*, **2017**, *9*, 44-51.
25. M. K. Dhinakaran and T. Mohan Das, *Org. Biomol. Chem.*, **2012**, *10*, 2077-2083.
26. M. Rajasekar and T. Mohan Das, *Trends in Carbohydr. Res.*, **2016**, *8*, 1-10.
27. M. Rajasekar and T. Mohan Das, *RSC. Adv.*, **2014**, *4*, 30976-30983.
28. M. Rajasekar and T. Mohan Das, *RSC. Adv.*, **2014**, *4*, 42538-42545.
29. M. K. Dhinakaran, K. Soundarajan and T. Mohan Das, *Trends in Carbohydr. Res.*, **2015**, *7*, 68-76.
30. A. Hemamalini and T. Mohan Das, *RSC. Adv.*, **2014**, *4*, 41010-41016.
31. S. Nagarajan, T. Mohan Das, P. Arjun and N. Raaman, *J. Mater. Chem.,* **2009**, *19*, 4587-4596.

32. M. K. Dhinakaran, K. Soundarajan and T. Mohan Das, *New J. Chem.*, **2014**, *38*, 4371-4379.

33. M. K. Dhinakaran, K. Soundarajan and T. Mohan Das, *New J. Chem.*, **2014**, *38*, 2874-2883.

34. R. Rajaganesh, A. Gopal, T. Mohan Das and A. Ajayaghosh, *Org. Lett.*, **2012**, *14*, 748-751.

35. A. Hemamalini and T. Mohan Das, *New J. Chem.*, **2014**, *38*, 3015-3021.

36. K. Soundarajan, R. Periyasamy and T. Mohan Das, *RSC. Adv.*, **2016**, *6*, 81838-81846.

	Rathinam Periyasamy *is currently doing research under the guidance of Dr. T. Mohan Das in the Department of Chemistry, Central University of Tamil Nadu (CUTN), Thiruvarur. He completed his B.Sc (Chemistry) from St. Joseph's College, Tiruchirappalli and M.Sc (Chemistry) from Bharathidasan University, Tiruchirappalli in 2010 and 2012, respectively. His current research interest is to investigate self-healing sugar based organogelators with multi stimuli responsive nature for environmental and drug delivery applications. He has published two research articles in the international journals.*
	Kamalakannan Soundarajan *is currently doing research under the guidance of Dr. T. Mohan Das in the Department of Chemistry, Central University of Tamil Nadu (CUTN), Thiruvarur. He has completed bachelor degree from Pachayappa's Collage for Men, Kanchipuram in 2006-2009 and master degree from University of Madras, Guindy campus, Chennai-25 in 2011. He is Currently working on synthesis of saccharide based Low Molecular Weight Organogelatar derivatives and also sugar based natural products. These derivatives are expected to have various applications in the field of materials and biology. He has published five research articles in well reputed international journals.*
	Dr. T. Mohan Das *received his Ph.D. from the Indian Institute of Technology Bombay (IITB) in Mumbai (India) under the supervision of Professor C. P. Rao in the field of carbohydrate chemistry. In 2002, he joined the group of Prof. D. –H. Chin at the National Chung Hsing University (NCHU), (Taichung, TAIWAN) as a post-doctoral fellow to work on the anticancer Neocarzinostatin (NCS) protein. Later he moved to National Tsing Hua University (NTHU), (Hsinchu, TAIWAN) and worked with Prof. J. R. Hwu in the area of silicon chemistry. In the year 2004, he started his independent professional carrier as an assistant professor in Department of Organic Chemistry, University of Madras, India which is an old and prestigious institute in the country. In the University of Madras, he started his independent research in the area of carbohydrate chemistry. Later on, in 2013, he moved to Central University of Tamil Nadu, Thiruvarur, Tamil Nadu, India as an associate professor. The principle interests of Mohan Das's research group are, (a) Development of novel synthetic methods, (b) Synthesis of sugar based gelator molecules and glyco-hybrids. His scientific work has been published in 50 original international publications with high profile journals, two review articles and one Indian patent. One of the article published in New Journal of Chemistry was awarded top ten article. He has successfully completed seven research projects sponsored by different funding agencies of Government of India. He was awarded Outstanding Young Scientist Scheme (2007), Dr. HC Srivastava Young Scientist Award (2015). He has guided eight and guiding four PhD students.*

Discrimination of the Physicochemical Processes in Dye Sensitized Solar Cell and Photoelectrochemical Solar Cells via Electrochemical Impedance Spectroscopy

Maurya Gyanprakash[1] and Raj Ganesh S Pala[1,2*]
[1]*Department of Chemical Engineering, Indian Institute of Technology Kanpur*
[2]*Material Science Programme, Indian Institute of Technology Kanpur*
Email: rpala@iitk.ac.in

Abstract

Illuminated Dye Sensitized Solar cells (DSSC) and Photoelectrochemical solar cells (PEC) involve convolution of physicochemical processes like electron-hole generation, separation and recombination, and trap recombination at the surface of the semiconductor electrode. In this article, we explore these processes using the Electrochemical Impedance Spectroscopy (EIS) wherein an equivalent circuit is posited from the current response of the system subjected to an AC superimposed on DC potential bias. The bulk and interfacial transport of electrons and holes under irradiation and electron-hole recombination governs the equivalent circuit at the SC/electrode interface and these processes can be dynamically separated via EIS. In DSSC, the presence of Gerischer type impedance at low frequency shows that the charge transport through interface is higher than the charge transport through the diffusion inside the SC electrode, while the presence of Resistance-Capacitance type impedance at low frequency shows charge transport through the interface is lower than the charge transport through diffusion. In PEC water splitting reaction, theoretical EIS modeling provides the equivalent circuit at SC/electrolyte interface, by taking trapping/detrapping, charge transfer through trap state and valance band into consideration. In PEC, there is competition of charge transfer from the valance band and the trap states. The low frequency capacitance can be used as a parameter for discrimination of these events. Here we demonstrate that using such electrical parameters, we can discriminate of physicochemical processes at DSSC and PEC, considering hematite and hetrostructured electrodes as specific case studies.

1. Introduction

Solar energy is preferred over non-renewable energy sources as it does not involve limited emission of green-house gases and because of its abundance. To extract the solar energy into usable energy/work/fuels, different methods of harvesting like photovoltaic [1], photocatalytic [2] and photoelectrochemical method[3] are used. Prerequisite to these methods are appropriate semiconductor (SC) electrodes and a convolution of many physichochemical steps like excitation of electrons-holes and separation of electron-hole pairs result in the generation of electrode potential from the solar light [4]. Increase in electron hole recombination, poor generation of electron hole pairs, low band-gap, low diffusion length results in decrease of potential extracted from the solar radiation [5]. The band gap of the given SC material depends on the position of conduction- and valence- band, and the states within the band gap are known as trap states [6]. The band gap of the given SC material must be optimum so as to absorb significant solar radiation, electron-hole pairs must be easily separable and recombination should be low [7].

In DSSC[8], dye molecules gets excited on irradiation ((a)-(b) in Fig.1, these excited molecules transfer the electrons to conduction band(CB) of SC and gets converted to S⁺((b) to (c) in Fig.1). The CB electrons have multiple routes to complete the circuit. Ideally it must go to the counter electrodes via the load (to extract the maximum potential generated into the useful work) to regenerate the redox couple (I^-/I_3^-), but the electrons can recombine via electronic states in the dye that are of low energy or recombine to regenerate the redox couple (I^-/I_3^-) and these recombination resistances are shown in fig.1. In DSSC, the aim is to decrease the recombination process to extract the maximum amount of the power available at the surface of the dye. To better understand these phenomena, it is critical to first deconvolute them and EIS facilitates this [9-11].

A schematic of PEC and associated electrochemical reactions are shown in Fig.2. In the water splitting reaction, oxygen evolution reaction (OER) occurs at the positive electrode and hydrogen evolution reaction (HER) occurs at the negative electrode [3]. The minimum thermodynamic potential required for the water splitting is 1.23V, but due
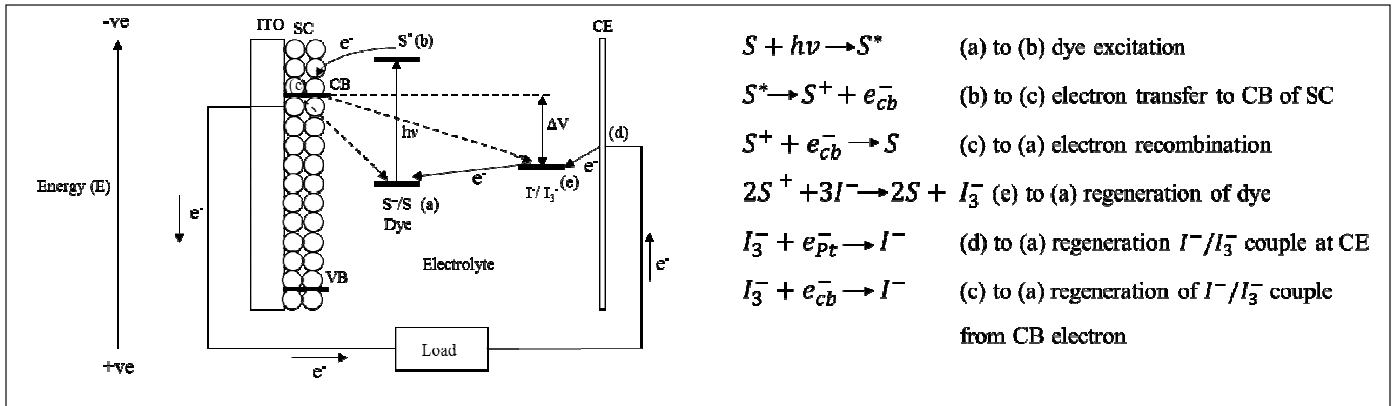
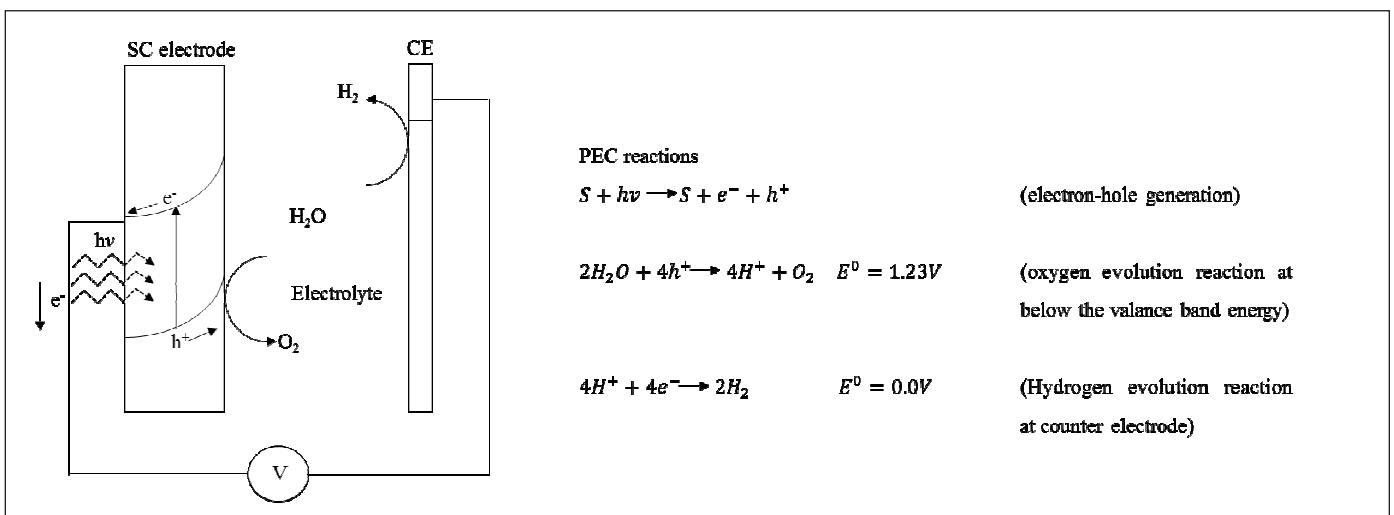*Fig.1:* *Schematic of DSSC with electrochemical reactions at dye and SC surface.*

Fig.2: *Schematic of PEC with electrochemical reactions at SC/electrolyte and Counter Electrode(CE)/electrolyte interface.*

to many activated processes (like electron-transfer at the electrodes, ion-transfer in the electrolyte), the on-set of finite reactivity occurs at around 1.6V and the potential over and above the minimum thermodynamic potential is called the overpotential. By employing the irradiated SC electrode in PEC, the externally applied DC potential for water splitting can be brought down [3, 12]. For OER at the SC electrode, the valence band energy must be below the OER redox potential plus overpotential. However, in most SC, the valance band energy is always above the redox potential of water plus overpotential, and to make it lower, an external bias and irradiation is applied [2, 3]. With SC electrode, the extraction of energy available at the surface is crucial and this is critically dependent on the extent of band bending at the surface and these can be analyzed by EIS [13, 14].

In Electrochemical Impedance Spectroscopy(EIS) [15], a DC (Direct Current) voltage with small AC (Alternating Current) voltage with varying frequency is applied at the interface, and output current is recorded. The ratio between input voltage to output current is the impedance, which consists of two parts, viz. real part and imaginary part. The impedance data is presented typically via a Nyquist plot or via a Bode plot. The Nyquist plot is between the imaginary and real part of the impedance, whereas the Bode plot depicts the variation of amplitude and phase of impedance with frequency. Using the Nyquist plot, an electrical circuit is derived that reflects the physical processes that occur at the electrode/electrolyte interface [16]. The simplest of such an electrical circuit is the Randles circuit (RC), with one resistor in parallel with a capacitor and such a circuit will generate a semicircular shaped Nyquist plot. In general, a Nyquist plot may contain many semicircles, each of which gives the number of times charges cross an interface. For complicated systems, the Nyquist plot are studied by dividing the Nyquist plot into high frequency-, intermediate- and low-frequency regions, and the effect of each region is analyzed separately [9-11]. The Bode curve can have many frequency dependent elements with each frequency element having a particular slope [17].

The aim of this review is to explore the applicability of EIS for discrimination of the processes occurring at the SC/electrolyte interface of DSSC and PEC. Various processes like trap state formation, electron hole recombination, space charge capacitance that affects the rate of charge transport at the SC/electrolyte interface are analyzed. In the past [13, 14], the effect of trap capacitance has not been taken into consideration and instead, the authors generally take into account the space charge capacitance and Helmholtz capacitance for modeling of IS data. Bisquert [18] has used the effect of trap capacitance in EIS and has shown that the capacitance obtained at these states are volumetric capacitance referred to as the chemical capacitance [19]. The trap capacitance is an important parameter that helps in distinguishing the transfer of electrons either from valance band or conduction band and this will be elaborated later in the review [18, 20, 21].

2. EIS of DSSC

The EIS of DSSC has been explored by Gratzel et.al [22] and this involves four transport processes occurring in whole cell: transport of charges at FTO/TiO$_2$ interface, TiO$_2$/electrolyte interface, bulk transport of I$_3^-$/I$^-$ couple for regeneration of dye, regeneration of I$_3^-$/I$^-$ couple at the counter electrode. The transport of charges inside the TiO$_2$ electrode contribute to diffusional transport resistance R_w (impedance caused by R_w is denoted by Z_{w1}), and the recombination reaction at TiO$_2$/electrolyte interface gives recombination resistance R_{ct}. Two types of charge transport are considered, complete charge transport events and fractional charge transport events.

For the complete charge transfer at TiO$_2$/FTO interface, $R_{ct} \gg R_w$. There will be presence of diffusional impedance with recombination resistance R_{ct} in series and the high value of R_{ct} increases the electron life time. Large electron life time results in the appearance of conduction band capacitance at TiO$_2$, and this capacitance is in parallel with the diffusional resistance and recombination resistance R_{ct} as shown in Fig. 3(a). For fractional charge transport, a part of charge will be transfer to interface, hence $R_{ct} \ll R_w$, and in this case the effect of R_{ct} and R_w is combined with Gerischer-impedance as shown in Fig. 3(b). (there is no separation between R_{ct} and R_w, the combined effect of this is Z_{w1}). Other part of electrical circuit, like impedance at the FTO/TiO$_2$ interface, impedance at the counter electrode and impedance for regeneration of dye will also appear in electrical circuit as shown in Fig. 3(a) and (b).
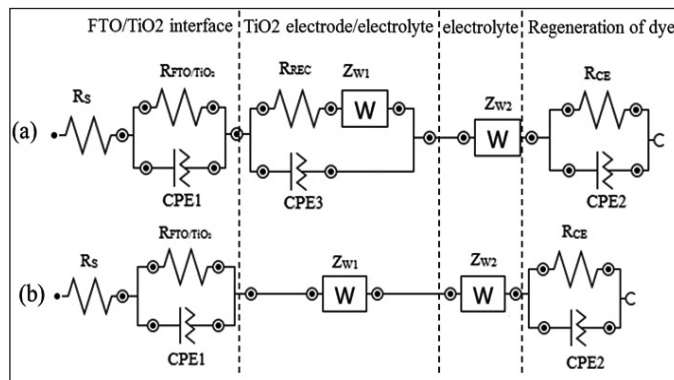

Fig.3: equivalent circuit of DSSC a) for complete transfer of charges under illumination, b) part of charges transferred. Adapted from Ref.12

Cao et. al.[10] demonstrated that the EIS at the SC/electrolyte interface shows two semicircles and interpreted that the low frequency region corresponds to charge transfer and high frequency region corresponds to adsorption. However, when EIS was conducted in dark, similar pattern of impedance was obtained, suggesting the presence of some another phenomena. They suggested that the high frequency semicircle is because of space charge and surface state charge transfer within the semiconductor, while the semicircle at low frequency is because of charges leaving the semiconductor. Takehito Mitate et.al[23] used the EIS response of the DSSC and the linear variation of interface resistance with potential indicated diode-like behavior. Bisquert et.al [11] studied the effect of diffusion and recombination inside the TiO$_2$ electrode by using EIS analysis with a transmission line analysis model. The thin film of TiO$_2$ electrode is in contact with electrolyte on one side and the other part in contact with the substrate (Fig. 4), with no electronic charges crossing the interface at the electrolyte side.
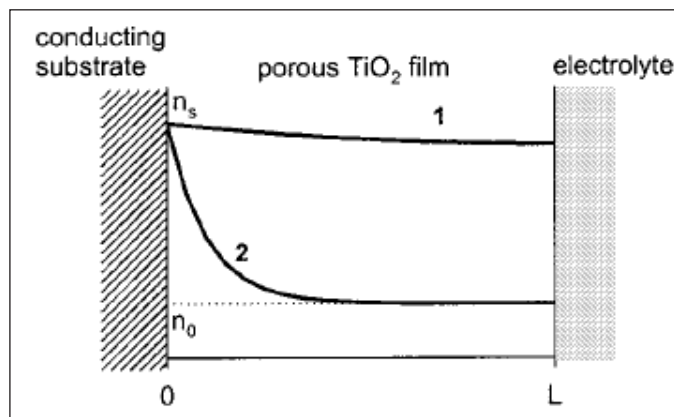

Fig.4: Porous TiO$_2$ electrode with 1) diffusion only, 2) diffusion with the recombination. Reprinted with permission from Ref 15. Copyright 2002 American Chemical Society

Transmission line representation with diffusion is depicted in Fig. 5(a), the corresponding impedance is obtained by balancing the charges inside the electrode (mode of transport of charges is diffusion only) given by,

$$Z = R_w(i\omega/\omega_d)^{-1/2} \coth[(i\omega/\omega_d)^{1/2}] \tag{1}$$

At high frequency,

$$Z = R_w(i\omega/\omega_d)^{-1/2} \tag{2}$$

Where ω_d is characteristic frequency for diffusion and equals to D/L^2, D is diffusion coefficient for electron transfer and L is the thickness of photoelectrode R_w, is the diffusional resistance and is dependent on the Fermi energy distribution. From Fig. 5(a), $R_w = L.r_m$, r_m, is the diffusional resistance per unit length. The above impedance at high frequency contains only the diffusional contribution and this response is valid till $\omega \gg \omega_d$ (ω is the frequency applied), and at low frequency i.e $\omega \ll \omega_d$, the response is capacitative as shown in the Nyquist plot (Fig.5(a)) which is given by,

$$Z = \frac{1}{3}R_w + \frac{1}{iC_f\omega} \tag{3}$$

C_f is the free charge capacitance, and it's given by,

$$C_f = \frac{1}{R_w.\omega_d} \tag{4}$$

For the case of diffusion with recombination inside the TiO$_2$ electrode, the mode of transport of charges contains recombination inside the TiO$_2$ electrode, the EIS response contains an additional term that takes into account the effect of the recombination resistance. The transmission line and the Nyquist plot is shown in Fig. 6(a), and it is given by,

$$Z = \left(\frac{R_wR_k}{1+i\omega/\omega_k}\right)^{1/2} \coth[(i\omega_k/\omega_d)^{1/2}(1+i\omega/\omega_k)] \tag{5}$$

Here ω_k is the characteristic frequency for recombination of charges and R_k is the total recombination resistance which is given by r_k/L, r_k, the fractional recombination resistance at surface. The EIS response in Fig. 6(b) contains two characteristic frequency i.e. ω_d and ω_k. In this case there are two subcases i.e. when $R_w \gg R_t$, i.e. when the diffusional resistance is higher than the recombination resistance (curve 1 and 2 in Nyquist plot of Fig.6 b) $R_t \gg R_w$ and recombination resistance is higher than the diffusional resistance (curve 3 of the Nyquist plot). when $R_t \gg R_w$, time for diffusion across the layer is lower than recombination time. i.e. $\omega_d \gg \omega_k$ for this case the high frequency part $\omega \gg \omega_d$ contains diffusional resistance (straight line 45° inclined) and its expression is as in equation 2.

The low frequency $\omega \ll \omega_d$, regime contains an extra term which shows the impedance due to the recombination (semi-circular part), and is given by,

$$Z = \frac{1}{3}R_w + \frac{R_k}{1+i\omega/\omega_k} \tag{6}$$

When $R_w \gg R_t$, i.e. the time for diffusion is larger than recombination time $\omega_k \gg \omega_d$, then the response is of Gerischer type, (i.e. diffusion in a semi-infinite region). This can be interpreted as the charges being consumed through the recombination reaction before reaching to other end of semiconductor electrode with the corresponding impedance given by,

$$Z = \left(\frac{R_kR_w}{1+i\omega/\omega_k}\right)^{1/2} \tag{7}$$

The effect of diffusion only and diffusion with recombination can be separated based on the impedance response at low frequency and high frequency regime.
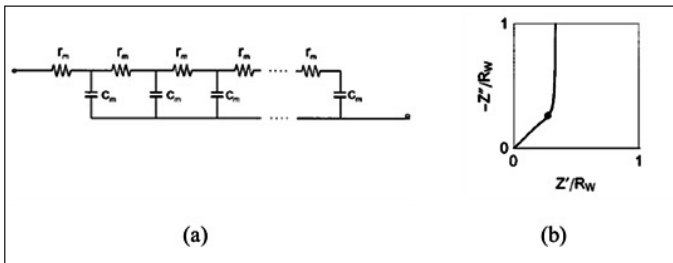

Fig.5: *(a) Transmission line representation of porous electrode with assumption that no charges are crossing the interface, (b) Nyquist plot representation of the TiO$_2$ porous electrode showing two distinguishable response. Reprinted with permission from Ref 15. Copyright 2002 American Chemical Society.*
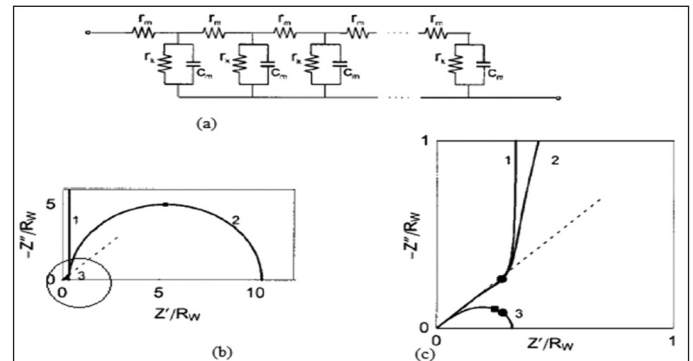

Fig. 6: *a) transmission line analysis of diffusion plus recombination in porous TiO$_2$ electrode, b) Nyquist plot of TiO$_2$ electrode, diffusion plus recombination of charges c) inside of circular part of fig (b). Reprinted with permission from Ref 15. Copyright 2002 American Chemical Society*

Further Bisquert et.al [24] used the above analysis to study the EIS of DSSC. In DSSC, the working electrode is TiO_2 and the counter electrode is Pt, the electrolyte is 0.5M LiI, 0.05M I_2 in 3-MPN (3-methoxypropionitrile). The EIS response of the whole DSSC set-up will contain the response from working electrode, counter electrode and the electrolyte. The transmission line representation of the DSSC working electrode is shown in Fig.7.
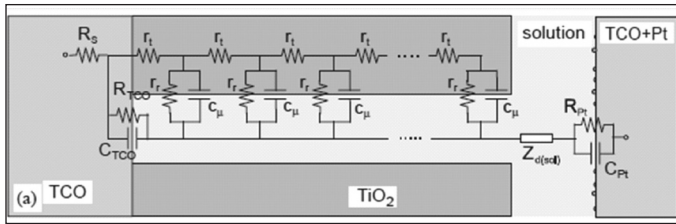

Fig.7: Transmission line representation of DSSC. Reprinted with permission from Ref 16. Copyright 2005 American Chemical Society

The Nyquist plot with potential variation is shown in Fig.8, and from these curves it is clear that up to potential 0.4, there is almost no change in shape of the Nyquist plot. Only one large semicircle is observed predominantly and the small semicircle at the high frequency (not clearly visible) in the Fig. 8(a-c) is due to the counter electrode reaction. In this zone, the TiO_2 working electrode acts as an insulator and charge transport occurs only in the part of substrate where TiO_2 has not been deposited (Fig.5 $R_{TCO}C_{TCO}$ part, R_{TCO} is recombination resistance at bare TCO surface and C_{TCO} is the corresponding capacitance). At higher potentials as shown in Fig. 8(d), the charges transport occurs through TiO_2 by diffusion and recombination mechanism. The Nyquist plot has 45° line at higher frequency, the high

frequency response is given by equation (2) that shows Warburg type of response (note that in equation. 2 R_w becomes $R_t = r_t/L$) low frequency is the semicircular part. If $\omega_d \gg \omega_k$, the diffusion time is smaller than the recombination time, the low frequency part is dominated by recombination reaction (from equation(6)). On the other hand, if $\omega_d \gg \omega_k$, then the low frequency response is of Gerischer type response, the low frequency part is due to the diffusion plus recombination reaction as described by equation (7). On further increase in the potential, (Fig. 8 e) the Nyquist plot contains clearly three regime, high frequency regime is due to the counter electrode reaction, intermediate frequency regime is due to the diffusion-recombination reaction and low frequency regime is due to the electrolyte decomposition.

3. EIS of PEC

In PEC system [5, 11-13, 19-21, 25], the SC electrode can be under DC potential bias as well as the irradiation. The OER reaction requires four holes from SC anode, these holes are created with help of irradiation and their energy levels are modified by external bias. The transport of charges through the interface (SC electrode/electrolyte) is being modeled here. On irradiation, there is generation of electron-hole pair, the electron can either go to the trap state or the conduction band, holes are in the valance band. Following are the generalized possibilities of transfer of holes from SC/electrolyte interface [25, 26]:

1. Hole can transfer from the trapped state with electron and hole recombination in bulk

2. Hole can transfer from the valance band with electron and hole recombination in bulk

3. Hole will not transfer from valance band or trapped state (only electron hole recombination takes place in bulk)

4. Hole can transfer from the trapped state without electron and hole recombination in bulk

5. Hole can transfer from the valance band without electron and hole recombination in bulk

If the SC electrode is very thin and of less than the space charge layer thickness then the recombination in bulk is neglected. For PEC water splitting the electrode thickness is kept less than space charge layer thickness. From the above case, case
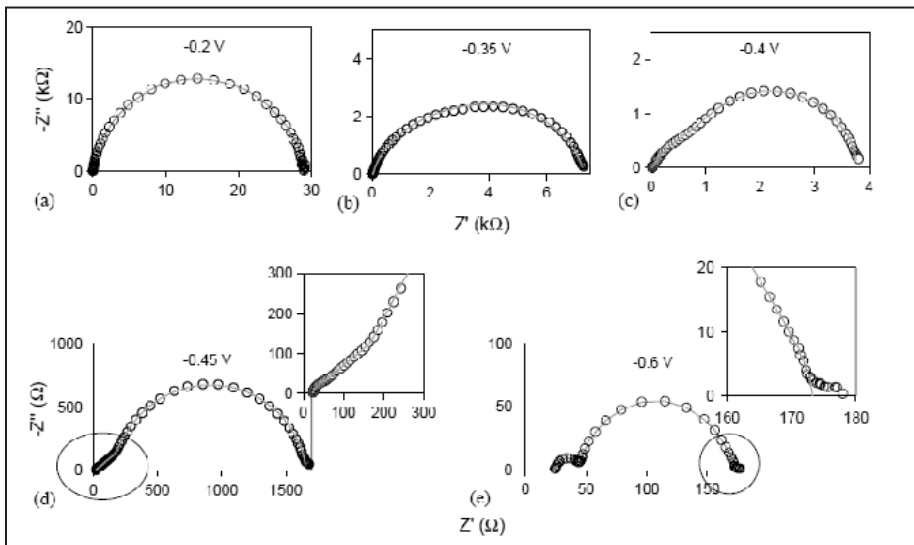

Fig.8: Impedance Spectra of DSSC at different potential (potential is shown inside the Nyquist plot). Reprinted with permission from Ref 16. Copyright 2005 American Chemical Society.
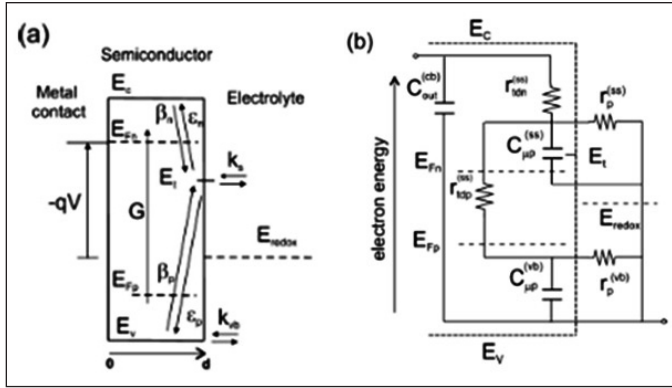
Fig. 9: a) energy levels at SC/electrolyte interface with steps involved in charge dynamics, b) the equivalent circuit of SC/electrolyte interface showing the various resistive and capacitive elements for trap state, valance band charge transport and conduction band charge transport. Reprinted with permission from Ref 9. Copyright 2012 American Chemical Society

4 and 5 represents the PEC water splitting mechanism and modeled by Bisquert et.al.[18]. The energy diagram and electrical equivalent circuit is shown in the following Fig.9.

The dynamics of electron density at SC side is given by,

$$\frac{\partial n}{\partial t} = -\frac{1}{q} \cdot \frac{\partial j_n}{\partial x} + G - \beta_n(1-f)n.N_t + \varepsilon_n f N_t \quad (9)$$

$$\frac{\partial p}{\partial t} = G - \beta_p f.p.N_t + \varepsilon_p.(1-f).N_t - k_{vb}(p-p_0) \quad (10)$$

$$\frac{\partial f}{\partial t} = \beta_n(1-f)n - \varepsilon_n f - \beta_p f.p + \varepsilon_p.(1-f) - k_s(f-f_0) \quad (11)$$

In above equation $n, p, G, \beta_n, \beta_p, \varepsilon_n, \varepsilon_p, k_{vb}, k_s, f, N_t$ are electron density in conduction band, hole density in valance band, charge generation rate, electron trapping from conduction band to trap state, hole trapping from valance band to trap state, electron detrapping from trap state to conduction band, hole detrapping from trap state to valance band, rate constant for electron transfer from valance band, rate constant from the trap state, probability that electron occupies the trap and number of traps. The steady state current analysis shows the effect of trapping, detrapping and charge transfer from valance band and trapped state. The trap state dynamics is described by comparing the detrapping of electrons and hole transfer from the interface. If the rate of detrapping of electrons is less than the rate of recombination of the holes through the interface ($\varepsilon_n \ll k_s$), then the onset voltage is lower compared to the case whereinthe rate of recombination is less than the rate of detrapping of electrons from the trap states ($\varepsilon_n \gg k_s$). This is due to the fact that at onset, holes

must increasingly cross the interface. If the trapping of holes are higher than the trapping of electrons then the onset voltage will be low.

With a small amplitude AC signal, the above three equations will provide the frequency and potential dependent impedance as,

$$Z^{-1} = \frac{j}{V} = j.\omega.C_\mu{}^{cb} + \left[r_{tdn}{}^{ss} + \cfrac{1}{j.\omega.C_{\mu p}{}^{ss}+(r_p{}^{ss})^{-1}+\cfrac{1}{r_{tdp}{}^{ss}+\cfrac{1}{j.\omega.C_{\mu p}{}^{vb}+(r_{tdn}{}^{ss})^{-1}}}}\right]^{-1}$$

(12)

The corresponding equivalent electrical circuit is shown in Fig. 9(b). The impedance of the given system contains three-time constants obtained by equation 12. The double layer capacitance, capacitance due to the depletion layer is taken into account by including it into the conduction band capacitance. In this case, authors [9] show a maximum of two semicircles. For the case of $\varepsilon_n \ll k_s$, the charge transport from the interface is high, therefore the low frequency semicircle is attributed to trap resistance and trap capacitance. When $\varepsilon_n \gg k_s$ then the trapping/detrapping process is faster than the charge transfer from the interface. If we take the electron hole recombination in bulk, i.e cases 1, 2 and 3. The equivalent electrical circuits will have one extra resistance known as bulk recombination resistance in parallel with trap impedance and bulk capacitance (the bulk capacitance is the combined effect of space charge , double layer and conduction band capacitance).

Bisquert et. al.[25] used the above hypothesis on the surface of photoelectrode Fe_2O_3 for OER reaction and demonstrated that the trap capacitance passes through the maxima with respect to the potential. This is due to the fact that the occupancy is the function of potential, up to half occupancy the charges are continuously stored in the trap states, beyond this they start crossing the interface via trapping/detrapping phenomenon, without trap capacitance decreasing with increase in potential. On higher potential, this trapping/ detrapping process becomes fast so that this trapping/detrapping resistance decreases, while trap resistance increases due to the fact less number of charges are flowing through it. The circuit corresponding to this analysis is shown in Fig. 10(a) and if recombination resistance is very high, then the electrical circuit will look like shown in Fig. 10(b). The capacitance C_T is the useful quantity to discriminate the transfer of charges either from trap state or valance band. While the trap state capacitance goes to maxima before decreasing, the valance band capacitance continues to increase with potential, hence
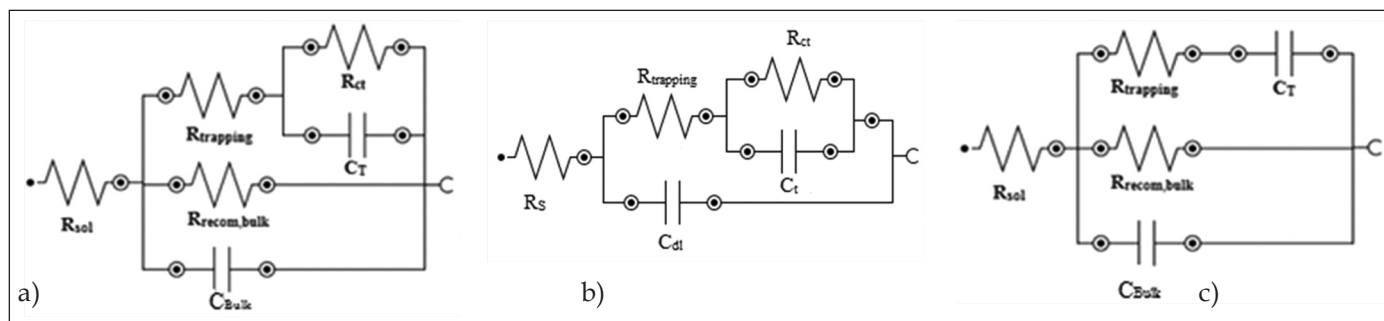
Fig. 10: *The equivalent circuit at SC/electrolyte interface for the case of transfer of electrons from Trap states or valance band, a) with recombination in bulk, b) without recombination in bulk, c) The equivalent circuit for no charges crossing the interface. Reprinted with permission from Ref 11. Copyright 2012 American Chemical Society*

C_T discriminates between the trap state or valance band charge transport mechanism [18].

4. Conclusion

EIS lends insight into the processes occurring at the interface of DSSC/electrolyte and PEC/electrolyte. For DSSC, diffusion-recombination model provides the information about the transport of charges from conduction band to electrolyte and counter electrode. The low frequency semicircle in Nyquist plot reveals the dependency of charge transport either on recombination reaction at interface or the combined effect of diffusion and recombination reaction. For PEC, the equivalent circuit shows the presence of three-time constants, these are due to transport of charges from conduction band i.e. trapping/detrapping, trap state and valance band. In real cases, there is presence of two semicircle or only one semicircle. Only one semicircle is due to the high trapping/detrapping rate as compared to charge transfer from the trap state ($\varepsilon_n >> k_s$), and discrimination between these two processes are difficult. The two semicircle is due to the trapping/detrapping and charge transfer either from trap state or from valance band. The behavior of C_T (low frequency capacitance) discriminates the charge transport either from trap state or valance band.

References

1. Shah, A., et al., *Photovoltaic technology: the case for thin-film solar cells.* science, 1999. **285**(5428): p. 692-698.

2. Hoffmann, M.R., et al., *Environmental applications of semiconductor photocatalysis.* Chemical reviews, 1995. **95**(1): p. 69-96.

3. Walter, M.G., et al., *Solar water splitting cells.* Chemical reviews. **110**(11): p. 6446-6473.

4. Lewis, N.S. and D.G. Nocera, *Powering the planet: Chemical challenges in solar energy utilization.* Proceedings of the National Academy of Sciences, 2006. **103**(43): p. 15729-15735.

5. Gratzel, M., *Photoelectrochemical cells.* nature, 2001. **414**(6861): p. 338.

6. De Jongh, P.E. and D. Vanmaekelbergh, *Trap-Limited Electronic Transport in Assemblies of Nanometer-Size Ti O 2 Particles.* Physical review letters, 1996. **77**(16): p. 3427.

7. Sze, S.M., *Semiconductor devices: physics and technology.* 2008: John Wiley & Sons.

8. O'Regan, B. and M. Grätzel, *A low-cost, high-efficiency solar cell based on dye-sensitized colloidal TiO 2 films.* nature, 1991. **353**(6346): p. 737-740.

9. Wang, Q., J.-E. Moser, and M. Grätzel, *Electrochemical impedance spectroscopic analysis of dye-sensitized solar cells.* The Journal of Physical Chemistry B, 2005. **109**(31): p. 14945-14953.

10. Leng, W.H., et al., *Investigation of the kinetics of a TiO2 photoelectrocatalytic reaction involving charge transfer and recombination through surface states by electrochemical impedance spectroscopy.* The Journal of Physical Chemistry B, 2005. **109**(31): p. 15008-15023.

11. Bisquert, J., *Theory of the impedance of electron diffusion and recombination in a thin layer.* The Journal of Physical Chemistry B, 2002. **106**(2): p. 325-333.

12. Fujishima, A. and K. Honda, *Electrochemical photolysis of water at a semiconductor electrode.* nature, 1972. **238**(5358): p. 37-38.

13. Steier, L., et al., *Understanding the role of underlayers and overlayers in thin film hematite photoanodes.* Advanced Functional Materials. **24**(48): p. 7681-7688.

14. Shimizu, K., A. Lasia, and J.-F.o. Boily, *Electrochemical impedance study of the hematite/water interface.* Langmuir. **28**(20): p. 7914-7920.

15. Orazem, M.E. and B. Tribollet, *Electrochemical impedance spectroscopy.* Vol. 48: John Wiley & Sons.

16. Lasia, A., *Electrochemical impedance spectroscopy and its applications*: Springer.

17. Park, S.-M. and J.-S. Yoo, *Peer reviewed: electrochemical impedance spectroscopy for better electrochemical measurements.* 2003, ACS Publications.

18. Bertoluzzi, L. and J. Bisquert, *Equivalent circuit of electrons and holes in thin semiconductor films for photoelectrochemical water splitting applications.* The journal of physical chemistry letters. **3**(17): p. 2517-2522.

19. Bisquert, J., *Chemical capacitance of nanostructured semiconductors: its origin and significance for nanocomposite solar cells.* Physical Chemistry Chemical Physics, 2003. **5**(24): p. 5360-5364.

20. Behara, D.K., et al., *Synchronization of charge carrier separation by tailoring the interface of Si–Au–TiO 2 heterostructures via click chemistry for PEC water splitting.* Chemical Engineering Science. **154**: p. 150-169.

21. Upadhyay, A.P., et al., *Fabricating Appropriate Band-Edge-Staggered Heterosemiconductors with Optically Activated Au Nanoparticles via Click Chemistry for Photoelectrochemical Water Splitting.* ACS Sustainable Chemistry & Engineering. **4**(9): p. 4511-4520.

22. Rossmeisl, J., A. Logadottir, and J.K. Nørskov, *Electrolysis of water on (oxidized) metal surfaces.* Chemical physics, 2005. **319**(1): p. 178-184.

23. Han, L., et al., *Modeling of an equivalent circuit for dye-sensitized solar cells.* Applied Physics Letters, 2004. **84**(13): p. 2433-2435.

24. Fabregat-Santiago, F., et al., *Influence of electrolyte in transport and recombination in dye-sensitized solar cells studied by impedance spectroscopy.* Solar Energy Materials and Solar Cells, 2005. **87**(1): p. 117-131.

25. Klahr, B., et al., *Water oxidation at hematite photoelectrodes: the role of surface states.* Journal of the American Chemical Society. **134**(9): p. 4294-4302.

26. Saha, S., et al., *Engineering Semiconductor Interfaces Via Non-Native Nanostructures to Facilitate Electron-Hole Separation.* ECS Transactions. 77(6): p. 85-94.

	Mr. Maurya Gyanprakash *Completed B.E. in Chemical Engineering from University of Mumbai and M.Tech. in Chemical Engineering from IIT Kharagpur. Currently, he is perusing Ph.D. from Department of Chemical Engineering at IIT Kanpur under the supervision of Dr. Raj Ganesh Pala. His current research area includes the understanding of electrocatalytic and photoelectrocataltic properties by using the Impedance method.*
	Raj Ganesh S. Pala *works in the broad area of electrochemical and reaction engineering with the current focus being electrocatalysis and photoelectrocatalysis of water splitting, chlorine evolution reaction and CO_2 reduction, models for crystal growth, selectivity in organic electrochemistry/heterogeneous catalysis, electrochemical sensors and electrode design for batteries. The research group aims to elucidate concepts that aid in designing functional materials and this often involves a semi-quantitative description of phenomena that span a wide range of length and time scales. In this context, analysis is performed via electrochemical and catalytic rate measurements, spectroscopy, quantum chemical density functional simulations and other computational techniques.*

Unique Non-Debye Relaxation Process and New Physical Insight for the Dielectric Loss

G. Govindaraj

Department of Physics, School of Physical, Chemical and Applied Sciences,
Pondicherry University, Puducherry 605 014, India
E-mail: ggdipole@gmail.com

Abstract

The dielectric response for a broad range of systems proves the existence of a remarkable features of frequency and time response which is basically incompatible with the variety of currently used time-honored (i) Cole-Cole (ii) Cole-Davidson (iii) Havriliak-Negami dielectric functions (iv) Kohlrausch-Williams-Watts stretched exponential function (v) Jonscher's universal dielectric response (vi) Ngai's coupling model and (vii) Dyre's random energy barrier model. The existing interpretations for these models/functions are: (a) distributions of relaxation times and (b) the energy criterion. Still, these empirical models and their theoretical interpretations are subject of debate in the literature and remain disjointed, and adapted to the individual materials. The purpose of paper is to present a novel concept of "Debye and fractional Debye type dipole" dielectric law of relaxation to the interpretation of the dielectric response of solids. The dielectric relaxation processes is based on Debye type dipole-dipole interaction initiated fractional Debye type dipoles in the wide range of materials, covering very diverse materials with physical processes-all of which show a remarkable features of the proposed relaxation behavior. The complex dielectric and relaxation functions, and their energy criterion in terms of the Debye and the fractional Debye dipole process provides a new physical insight for the α, β, γ, δ relaxations, excess wing and shoulder structure in the dielectric loss of glass formers, plastic crystals, drugs, polymers, *etc*. The model shows an excellent agreement with experimentally observed dielectric spectra of wide variety of materials.

1. Introduction

The dielectric response of most of the condensed matter system shows a remarkable degree of features in that its frequency dependence often follows deviation from classically expected Debye response, which in the time domain corresponds to exponential decay. The deviation of dielectric response from the Debye feature, in general, is referred as non-Debye relaxation (NDR) or many-body relaxation [1,2]. Their interpretation of temperature dependence is carried out using either individual or combination of time-honoured models like: (i) Cole-Cole (CC) [3-5] (ii) the Cole-Davidson (CD) [6] (iii) Havriliak-Negami (HN) [7] dielectric functions (iv) Kohlrausch-Williams-Watts (KWW) stretched exponential function [8,9] (v) Jonscher's universal dielectric response (UDR) [10-12] and (vi) Ngai's coupling model (CM) [2,13-15], (vii) Dyre's random energy barrier model [16-18]. Each function has different level of significance for the physical process of NDR and no consensus has been arrived so far. Therefore, there is a need of unique NDR function connecting time and frequency domains with generally acceptable microscopic physical process. In present work, we propose NDR model considering the intermolecular Debye type dipole-dipole interaction generated fractional Debye type dipole or non-Debye dipole in coupled form by considering energy criterion in the form of conservation of energy and moment.

The proposed concepts constitutes a "innovation" in thinking about dielectric relaxation and it moves away from the former interpretations which were depend on heavily on the concept of (a) distributions of relaxation times as used in CC, CD, HN, and KWW, (b) the energy criterion as used in Jonscher's UDR. The Debye-like processes supposed to be coexisting in CC, CD, HN, KWW models, whereas, Debye like process do not coexisting in the energy criterion based Jonscher's UDR and these models constitute a superficially plausible models. The existing distribution of relaxation time interpretation and energy criterion based models for the NDR do not stand up to critical examination and that a different approach is therefore essential. Our proposed model and new interpretation is based on the unique property of molecular level Debye type dipole and its interaction caused fractional Debye type dipole relaxation in coupled form of fractional Debye type dipole relaxation law in frequency that the ratio of the imaginary to the real parts of the complex dielectric is dependent on frequency, in sharp contrast to the Jonscher's UDR where this ratio is independent of wide range of frequency. Expressions for the complex dielectric and relaxation functions have been derived for the Debye and fractional Debye type dipole processes. Salient features of the proposed complex dielectric and relaxation functions

are described and compared with time-honoured models. There are controversial results reported and debated in the literature on the interpretation of α, β, γ, and δ relaxations, and excess wing of dielectric loss data of liquids, glass formers, polymers, drugs, plastic crystals *etc*. The proposed model certainly provide new physical insight for the NDR and expected to answer many issues related to the interpretation of α, β, γ, and δ relaxations, and clarify physical picture for excess wing.

2. Debye and non-Debye dielectric functions

Debye's original model of dipolar dielectric response consists of a set of identical non-interacting dipoles free to rotate against some viscous resistance in fluid-like medium by thermal excitation between two preferred orientations separated by a potential barrier, a situation more likely to be found in solids. In a log(frequency) vs log(dielectric loss) plot the Debye dielectric loss is symmetric with respect to loss peak having slope +1 below the loss peak and -1 above loss peak and has full width at half maximum (FWHM) 1.144 decades. Typical Debye type features of dipolar behaviour may be found in few polymers in which the dipole may be well characterized both in type and in density. However, the dielectric response in several polymers and other different system departs strongly from Debye features.

Cole and Cole [3] (CC) suggested the empirical dielectric function to account for the deviation from Debye features as:

$$\epsilon_{CC}^*(\omega) = \epsilon_\infty + \frac{\Delta\varepsilon_{CC}}{1+(i\omega\tau_{CC})^{1-\alpha_{CC}}} \qquad (1)$$

where $0\leq\alpha_{CC}<1$ is a CC parameter depends on material, temperature and pressure, and τ_{CC} is the CC type relaxation time, $\Delta\varepsilon_{CC}=\varepsilon_s-\varepsilon_\infty$, CC dielectric relaxation strength, ε_s and ε_∞ are respectively the high and low frequency limits. In a log(frequency) vs log(dielectric loss) plot the CC dielectric loss is symmetric with respect to loss peak, having slope $(1-\alpha_{CC})<1$ below the loss peak and $(1-\alpha_{CC})<-1$ above loss peak, and having FWHM greater than the Debye dielectric loss FWHM of 1.144 decades.

The dielectric loss data of many super-cooled mono-alcohols and poly-alcohols have shown asymmetry with respect to loss peak having long tail or excess wing. Cole and Davidson [6] (CD) suggested the empirical formula having asymmetric loss in the dielectric function:

$$\epsilon_{CD}^*(\omega) = \epsilon_\infty + \frac{\Delta\varepsilon_{CD}}{(1+i\omega\tau_{CD})^{\beta_{CD}}} \qquad (2)$$

where $0<\beta_{CD}\leq1$, is a CD parameters depends on material, temperature and pressure and τ_{CD} is the CD type relaxation time, $\Delta\varepsilon_{CD}=\varepsilon_s-\varepsilon_\infty$, CD dielectric relaxation strength, ε_s and ε_∞ are respectively the high and low frequency limits. In a log(ω) vs log(dielectric loss) plot the CD dielectric loss is asymmetric with respect to loss

peak having slope 1 below the loss peak and < -1 above loss peak.

Some super-cooled systems, polymers and plastic crystals and glasses have CC type spectra at low frequencies and CD type spectra at high frequencies. In work of Havriliak and Negami [7] proposed the following empirical form dielectric function:

$$\epsilon_{HN}^*(\omega) = \epsilon_\infty + \frac{\Delta\varepsilon_{HN}}{((1+(i\omega\tau_{HN})^{1-\alpha_{HN}})^{\beta_{HN}}} \qquad (3)$$

where $0\leq\alpha_{HN}<1$ and $0<\beta_{HN}\leq1$ are parameters depends on material, temperature and pressure and τ_{HN} is HN type relaxation time. In a log(frequency) vs log(dielectric loss) plot the HN dielectric loss is asymmetric with respect to loss peak having slope <1 below the loss peak and < -1 above loss peak and having FWHM greater than the Debye dielectric loss FWHM of 1.144 decades.

The inverse Laplace transform of Eqs. (1)-(3) into the time domain are *not* analytical functions. For the time dependence polarization current description KKW [8,9] empirical function:

$$i_{Kww}(t) \propto \phi_{KWW}(t) \propto \exp\left(-(t/\tau_{KWW})^{\beta_{KWW}}\right) \qquad (4)$$

is used, where $0<\beta_{KWW}\leq1$, the exponent β_{KWW} is a stretching parameter, and lower the β_{KWW} value the more stretching is the relaxation function and τ_{KWW} is the KKW relaxation time. The stretching can formally be explained by assuming a superposition of exponentials with distribution of relaxation times.

Jonscher has reviewed phenomenology of dielectric response in wide range materials. He has derived the so-called "universal dielectric response" by examining the dielectric loss in the frequency and time domains and tentatively modelled in terms partial charge screening process [10-12]. Jonscher found that the power law is a manifestation of a universal mechanism in which the energy loss per cycle to the energy stored per cycle is independent of frequency rather than being the result of superposition of Debye like loss with distribution of relaxation time as in CC, CD, HN and KWW. Jonscher's empirical form of dielectric loss is:

$$\varepsilon''(\omega) \propto [(\omega/\omega_2)^{-m}+(\omega/\omega_1)^{(1-n)}]^{-1} \qquad (5)$$

where m and (1-n) are both smaller than unity, ω_1, ω_2 and ω_p are thermally activated hopping parameters. In a log(frequency) vs log(dielectric loss) plot the UDR is asymmetric with respect to loss peak having slope m<1 below the loss peak and (1-n)< -1 above loss peak and having FWHM greater than the Debye dielectric loss FWHM of 1.144 decades, and normally m is greater than n. The empirical form for polarization current Eq. (5) is proposed as

$$i(t) \propto [(t\omega_p)^{1+m}+(t\omega_p)^n]^{-1}. \qquad (6)$$

A change in slope has been shown in double logarithmic time-domain plot with sum of two consecutive independent displacement current in the material medium. Jonscher's empirical form of dielectric function exponent's (n, m) are *not* related each other, and the exponents α_{CC}, β_{CC}, (α_{HN}, β_{HN}) and β_{KWW} and their use in dielectric loss data interpretation is still debatable in the literature.

3. Debye and fractional Debye type dipole dielectric functions

3.1 Debye and fractional Debye type dipole process

Let the condensed matter system consist of molecules with reorientation of dipolar entities with Debye type dipole moment G_0. In an electric field under a given thermodynamic condition, the instantaneous transfer of dipole moment G_0 is not possible for a given molecular process due to intermolecular Debye type dipole-dipole interactions. The fraction of Debye type dipole that has not been transferred instantaneously is defined as $\pm G=(1-g_d)G_0$, where $0<g_d<1$. The consequence of these interaction is the shift in the magnitude of Debye dipole moment G_0 by an equal magnitude of $\pm G=(1-g_d)G_0$ as illustrated in Fig.1. Debye type G_0 dipoles evolved with these interaction as fractional Debye type dipoles [19,20]:

$$G_+=G_0+G=(2-g_d)G_0, \text{ and } G_-=G_0-G=g_dG_0, \qquad (7)$$

where N number of Debye type G_0 per unit volume and becomes N/2 pairs of $G_\pm$, and dipole moment of G_+ and G_- is increased and decreased respectively by a factor of $(1-g_d)$ with respect to G_0. These type of dipole moment evolution in condensed matter systems lead to potential energy landscaping, a complicated dependence of energy on configuration, and a change in configurational entropy and a change in fragility, a measure of rapidity with which the liquid's properties like viscosity changes.

The average dipole moment is determined by using Langevin function for Debye type dipole and fractional Debye type dipole and it is found to be:

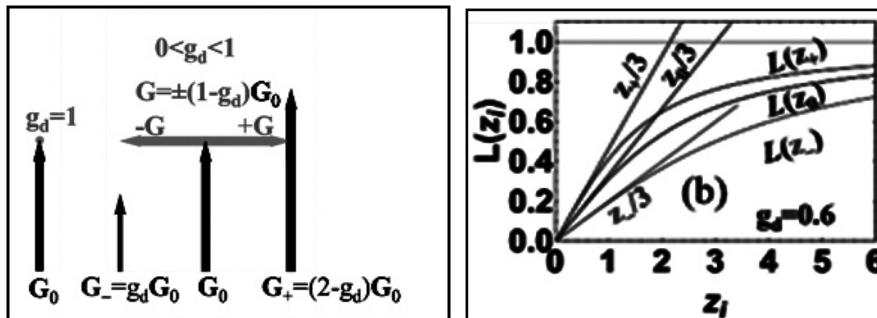$$<\mu_i>=\mu_iL(z_i), L(z_i)=coth(z_i)-1/z_i \qquad (8)$$

Fig. 1: Scheme showing Debye type dipole G_0 (black vector, $g_d=1$) and fractional Debye type dipole G_- (red vector) and G_+ (blue vector) on the left panel, $0<g_d<1$. Langevin functions for the Debye type dipole G_0 (black line, $g_d=1$) and fractional Debye type dipole G_- (red line) and G_+ (blue line) for $0<g_d<1$.

where $z_i=\mu_iE/(k_BT)$, E is external applied electric field, the symbols <> stand for ensemble average for the dipoles and μ_i stands for the dipoles G_0, G_+ and G_-. The statistical distribution of irreversible processes follows the Boltzmann factor $exp[-(U_i/k_BT)]$, $U_i=G_icos(\theta_i)E$, where the energy of G_0, is redistributed through, G_-, and G_+, such that total energy is conserved, and θ_i is angle between dipole moment and E. In **Fig.1**, in the right panel, for $z_i>>1$ the $L(z_i)=1-1/z_i$ and approaches to one, however, for low field limit $z_i<<1$, the linear regime $L(z_i)=(1/3)z_i$ and saturation *depends* on fractional Debye type dipole strength g_d. The energy and moment of the dipole G_- and G_+ is shifted with respect to G_0, in equal magnitude, and the total energy and moment of the system is conserved. Since, the energy of Debye dipole G_0 is redistributed through the fractional Debye type dipole pair $G_\pm$, the dielectric loss spectra of $G_\pm$ spreads with respect Debye type dipole G_0 dielectric loss spectra.

3.2 Dielectric and relaxation functions for Debye type dipole G_0

Debye type dipole dielectric function provides unique information pertaining to the molecular process of matter, structure, chemical composition. The Debye relaxation function and Debye dielectric function for the non-interacting Debye type dipole G_0 is the earliest known functions for the description of dielectric relaxation process and it can be obtained Laplace transform of negative derivative of dielectric relaxation function and it is found to be:

$$[i_d(t)]_{G_0} \propto [\phi_d(t)]_{G_0} \propto exp\left[-\left(\frac{t}{\tau_D}\right)\right] \propto exp\left[-\left(\frac{T}{\Gamma}\right)_{G_0}\right],$$

with $(T)_{G_0} = t$, $(\Gamma)_{G_0} = \tau_d=\tau_D$, for $g_d=1$ $\qquad$ (9a)

$$[\epsilon_d^*(\omega)]_{G_0} - \epsilon_\infty = \frac{(\Delta\epsilon)_{G_0}}{(1+i\omega\tau_D)}=\left(\frac{\Delta\epsilon}{1+S\Gamma}\right)_{G_0}, (s)_{G_0} = i\omega,$$

$(\Gamma)_{G_0} = \tau_D, g_d=1,$ $\qquad$ (9b)

$$(\Delta\epsilon)_{G_0} = (\epsilon_s - \epsilon_\infty)_{G_0} = N\frac{G_0^2}{3\epsilon_0k_BT} - \epsilon_\infty, \qquad (9c)$$

where $[\phi_d(t)]_{G_0}$ and $[\epsilon_d^*(\omega)]_{G_0}$ is the dielectric relaxation and complex dielectric functions for the Debye type dipole moment G_0, τ_D is the Debye dielectric relaxation time, $s=i\omega$ is Laplace transform parameter, ω is the frequency of an external applied electric field, i is the complex unit accounts for the energy loss mechanism in frequency domain, $(\Delta\epsilon)_{G_0}$ the dielectric strength for Debye mechanism, N is the density of dipoles, T is the temperature, ϵ_s and ϵ_∞ are respectively the high and low frequency

limits. The normalized Debye function Eq. (9a) has dielectric loss peak $\omega\tau_D = \tan(\pi/4) = 1$, which is symmetric on a log-log plot having slope 1 on the left side and -1 on the right side of loss peak respectively and has full width at half maximum (FWHM) of 1.144 decades [10].

3.3 Dielectric and relaxation functions for the fractional Debye type dipole G_

The complex dielectric function for the fractional Debye type dipole $G_- = g_d G_0$ is obtained by incorporating the consequence of $-G = (1-g_d)G_0$ on G_0, where $[\epsilon_d^*(\omega)]_{G_0}$ is the Debye type dipole complex dielectric function. The consequence of $-G$ on the Debye type dielectric function and complex dielectric function is shifting of the Debye type dipole relaxation term t/τ_d, and $i\omega\tau_d$ by a factor of $(t/\tau_d)^{1-g_d}$, $(i\omega\tau_d)^{1-g_d}$ and hence the Debye type dipole terms t/τ_d and $i\omega\tau_d$ become fractional Debye type dipole relaxation terms in the time domain as $(t/\tau_d)/(t/\tau_d)^{1-g_d} = (t/\tau_d)^{g_d}$ in the frequency domain as $i\omega\tau_d/(i\omega\tau_d)^{1-g_d} = (i\omega\tau_d)^{g_d}$. In terms of dipole energy, the Debye type dipole energy is *decreased* by a factor of $(1-g_d)$. The dielectric relaxation and complex dielectric functions are obtained for the fractional Debye type dipole $G_- = g_d G_0$ by changing the Laplace transform variables $t = (T)_{G_0}$ and $\tau_d = (\Gamma)_{G_0}$, $(s)_{G_0} = i\omega$ as

$$t^{g_d} = (T)_G, \quad \tau_d^{g_d} = (\Gamma)_G, \quad (s)_{G_-} = (s)_{G_0}/(s^{1-g_d})_{G_0}$$

$$[i_d(t)]_{G_-} \propto [\phi_d(t)]_{G_-} \propto exp\left[-\left(\frac{t}{\tau_d}\right)^{g_d}\right] \propto exp\left[-\left(\frac{T}{\Gamma}\right)_{G_-}\right],$$

$$[\epsilon_d^*(\omega)]_{G_-} - \epsilon_\infty = \frac{(\Delta\epsilon)_{G_-}}{1+(i\omega\tau_d)^{g_d}} = \left(\frac{\Delta\epsilon}{1+S\Gamma}\right)_{G_-}, (s)_{G_-} = \frac{s}{s^{1-g_d}}, \quad \text{i)}$$

$$(\Gamma)_{G_-} = \tau_d^{g_d}, \; s = i\omega, \tag{10b}$$

where

$$(\Delta\epsilon)_G = (\epsilon_s - \epsilon_\infty)_G = \frac{N}{2}\frac{G_-^2}{3\epsilon_0 k_B T} - \epsilon_\infty, \tag{10c}$$

is the dielectric strength of G_- which is differ from Debye type dielectric strength, ϵ_S and ϵ_∞ are the high and low external frequency dielectric limits respectively, N is G_- dipole density. This is similar to CC type complex dielectric function [3], however, $(\Delta\epsilon)_G$ is different from $(\Delta\epsilon)_{G_0}$ since number density N and average dipole strength are altered by the manifestation of 'many-particle' like intermolecular interaction mechanism. The fractional Debye type dipole strength indicate strength of interaction in terms of exponent when $0 < g_d < 1$, and for the Debye type dipole process, $g_d = 1$ and it is a manifestation of 'single-particle' like molecular interaction mechanism.

3.4 Dielectric and relaxation functions for the fractional Debye type dipole G_+.

The complex dielectric function for fractional Debye type dipole $G_+ = g_d G_0$ is obtained by incorporating the consequence of $+G = (1-g_d)G_0$ on G_0, where $[\epsilon_d^*(\omega)]_{G_0}$ is the Debye type dipole complex dielectric function. The consequence of G on the Debye type dielectric function and complex dielectric function is shifting of the Debye type dipole relaxation term t/τ_d and $i\omega\tau_d$ by a factor of $(t/\tau_d)^{-(1-g_d)}$, $((-i)\omega\tau_d)^{-(1-g_d)}$ and hence the Debye type dipole terms, t/τ_d and $i\omega\tau_d$ become fractional Debye type dipole relaxation terms in the time domain as $(t/\tau_d)/(t/\tau_d)^{-(1-g_d)} = (t/\tau_d)^{2-g_d}$, in the frequency domain as $i\omega\tau_d/((-i)\omega\tau_d)^{-(1-g_d)} = i^{g_d}(\omega\tau_d)^{2-g_d}$. In terms of dipole energy, the Debye type dipole energy is *increased* by a factor of $(1-g_d)$. The dielectric relaxation and complex dielectric functions are obtained for the fractional Debye type dipole $G_+ = (2-g_d)G_0$ by changing the Laplace transform variables $t = (T)_{G_0}$ and $\tau_d = (\Gamma)_{G_0}$

$$(s)_{G_0} = i\omega \quad \text{as} \; t^{2-g_d} = (T)_{G_+},$$

$$\tau_d^{2-g_d} = (\Gamma)_{G_+}, (s)_{G_+} = (s)_{G_0}/((-s)^{-(1-g_d)})_{G_0},$$

$$[i_d(t)]_{G_+} \propto [\phi_d(t)]_{G_+} \propto exp\left[-\left(\frac{t}{\tau_d}\right)^{2-g_d}\right] \propto exp\left[-\left(\frac{T}{\Gamma}\right)_{G_+}\right],$$

$$(T)_{G_+} = t^{2-g_d}, (\Gamma)_{G_-} = \tau_d^{2-g_d}, \; 0<g_d<1, \tag{11b}$$

$$[\epsilon_d^*(\omega)]_{G_+} = \frac{(\Delta\epsilon)_{G_+}}{1+i^{g_d}(\omega\tau_d)^{2-g_d}} = \left(\frac{\Delta\epsilon}{1+S\Gamma}\right)_{G_+},$$

$$(s)_{G_+} = \frac{(s)_{G_0}}{((-s)^{-(1-g_d)})_{G_0}}, (\Gamma)_{G_+} = \tau_d^{g_d}, \; s = i\omega, \tag{11b}$$

where

$$(\Delta\epsilon)_{G_+} = (\epsilon_s - \epsilon_\infty)_{G_+} = \frac{N}{2}\frac{G_+^2}{3\epsilon_0 k_B T} - \epsilon_\infty, \tag{11c}$$

is the dielectric strength of G_+ which is differ from dielectric strength of G_-, ϵ_S and ϵ_∞ are the high and low external frequency permittivity limits respectively, N is G_+ dipole density. Equation (11b) is completely different from CC type complex dielectric function and it is second consecutive secondary fractional Debye type dipole process dielectric function related to Debye type dipole dielectric relaxation process. The $(\Delta\epsilon)_{G_+}$ is different from , since number density N and average dipole strength are altered by the manifestation of 'many-particle' intermolecular interaction mechanism. The fractional Debye type dipole strength indicate strength of interaction in terms of exponent $0 < g_d < 1$.

3.5 Unique non-Debye relaxation and the energy criterion

We have shown unique NDR process in Eqs. (9)-(11) both in frequency-time domains consists of (a) primary Debye type dipole process dielectric response and and (b) two consecutive secondary fractional Debye type dipole processes dielectric response and , and and containing

the primary process in both the consecutive secondary processes, where total energy loss of Debye type dipole process and total Debye type dipole moments are conserved. Energy criterion for proposed model is shown in terms energy loss and energy storage of G_0, G_- and G_+. For the dipole density N of Debye type dipoles G_0 (absence of dipole-dipole interactions) the energy criterion is given by classical case of Debye dielectric response, and the ratio of energy loss and energy storage is obtained by Eq. (9a) as:

$$\left(\frac{\epsilon_d''(\omega)}{\epsilon_d'(\omega)}\right)_{G_0} = -(\omega\tau_D)_{G_0}, \text{ at } \omega=1/\tau_D, (\omega\tau_D)_{G_0} = \tan(\pi/4)=1, g_d=1, \quad (12)$$

where the real and imaginary parts of $[\epsilon_d^*(\omega)]_{G_0}$ are,

$$(\epsilon_d'(\omega) - i\epsilon_d''(\omega))_{G_0} \propto \left(\frac{1}{1+(\omega\tau_D)^2} - i\frac{\omega\tau_D}{1+(\omega\tau_D)^2}\right) \quad (13)$$

As explained earlier, Debye type dipole-dipole molecular interaction and their evolution transform the N dipoles into N/2 dipoles of G_- and N/2 dipoles of G_+ by distributing the Debye type dipole energy and moment, where the total Debye type dipole moment and energy is conserved in the processes. For the fractional type Debye type dipoles G_-, the energy criterion is similar to the classical case of Debye dielectric response result with a dispersion different from classical case of Debye dielectric response and the ratio of energy loss and energy storage is obtained by using Eq. (10b) as:

$$\left(\frac{\epsilon_d''(\omega)}{\epsilon_d'(\omega)}\right)_{G_-} = -\frac{(\omega\tau_d)^{g_d}\sin\left(\frac{g_d\pi}{2}\right)}{\left(1+(\omega\tau_d)^{g_d}\cos\left(\frac{g_d\pi}{2}\right)\right)}, \text{ at } \omega=1/\tau_d,$$

$$\frac{(\omega\tau_d)^{g_d}\sin\left(\frac{g_d\pi}{2}\right)}{\left(1+(\omega\tau_d)^{g_d}\cos\left(\frac{g_d\pi}{2}\right)\right)} = \tan\left(\frac{g_d\pi}{4}\right), 0<g_d<1, \quad (14)$$

where the real and imaginary parts of $[\epsilon_d^*(\omega)]_G$ are,

$$(\epsilon_d'(\omega) - i\epsilon_d''(\omega))_{G_-} \propto \left(\frac{1+(\omega\tau_d)^{g_d}\cos\left(\frac{g_d\pi}{2}\right)}{1+2(\omega\tau_d)^{g_d}\cos\left(\frac{g_d\pi}{2}\right)+(\omega\tau_d)^{2g_d}} - \right.$$

$$\left. i\frac{(\omega\tau_d)^{g_d}\sin\left(\frac{g_d\pi}{2}\right)}{1+2(\omega\tau_d)^{g_d}\cos\left(\frac{g_d\pi}{2}\right)+(\omega\tau_d)^{2g_d}}\right). \quad (15)$$

For the fractional type Debye type dipoles G_+, the energy criterion is again similar to the classical case of Debye dielectric response result with a dispersion different from classical case of Debye dielectric response and the ratio of energy loss and energy storage is obtained by using Eq. (11b) as:

$$\left(\frac{\epsilon_d''(\omega)}{\epsilon_d'(\omega)}\right)_{G_+} = -\frac{(\omega\tau_d)^{2-g_d}\sin\left(\frac{g_d\pi}{2}\right)}{\left(1+(\omega\tau_d)^{2-g_d}\cos\left(\frac{g_d\pi}{2}\right)\right)}, \text{ at } \omega=1/\tau_d, \quad (16)$$

$$\frac{(\omega\tau_d)^{2-g_d}\sin\left(\frac{g_d\pi}{2}\right)}{\left(1+(\omega\tau_d)^{2-g_d}\cos\left(\frac{g_d\pi}{2}\right)\right)} = \tan\left(\frac{g_d\pi}{4}\right), 0<g_d<1,$$

where the real and imaginary parts of $[\epsilon_d^*(\omega)]_{G_+}$ are ,

$$(\epsilon_d'(\omega) - i\epsilon_d''(\omega))_{G_+} \propto \left(\frac{1+(\omega\tau_d)^{2-g_d}\cos\left(\frac{g_d\pi}{2}\right)}{1+2(\omega\tau_d)^{2-g_d}\cos\left(\frac{g_d\pi}{2}\right)+(\omega\tau_d)^{2(2-g_d)}} - \right.$$

$$\left. i\frac{(\omega\tau_d)^{2-g_d}\sin\left(\frac{g_d\pi}{2}\right)}{1+2(\omega\tau_d)^{2-g_d}\cos\left(\frac{g_d\pi}{2}\right)+(\omega\tau_d)^{2(2-g_d)}}\right). \quad (17)$$

The proposed model is a coupled form Debye type dipole and fractional Debye type dipole processes and the primary relaxation time is Debye type dipole relaxation time and it is designated as τ_D, where the exponent $g_d=1$, and when $0<g_d<1$, the relaxation time is designated as τ_d.
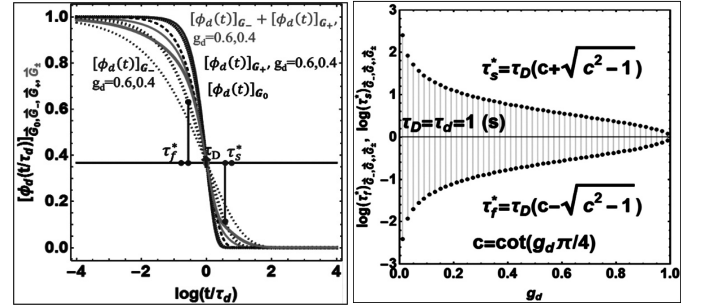

Fig. 2: Polarization relaxation function for the Debye type dipole G_0 polarization (dashed black line) and fractional Debye type dipole G_- (red small dotted line g_d=0.6), G_+ (blue bigger dotted line, g_d=0.4) and G_-+G_+ (green thick line g_d=0.4, thin line g_d=0.6) polarization (left panel). The red arrow indicates Debye relaxation time (1s), and the red dots indicate slow relaxation time τ_s^* and blue dots indicate fast relaxation time τ_f^* for g_d=0.6, 0.4 respectively. These time scales are defined as NDR times due to the fractional Debye type dipole processes and it is dynamically correlated to the Debye type dipole relaxation time τ_D. The right panel shows NDR times τ_s^* and τ_f^* as function interaction strength g_d based on Eqs. (18) & (19).

3.6 Slow and fast relaxation times in the fractional Debye type dipole process

According to the proposed model both Debye type and fractional Debye dipole processes have relaxation time $\tau_D=\tau_d$ and it is a primary relaxation time. Then, what is the relaxation time for the fractional Debye type dipole process? A careful analysis of Debye type dipole and the fractional Debye type dipole energy criterion provided two relaxation time scales correlated to primary relaxation time τ_D. By equating Debye type dipole process dielectric loss energy to fractional Debye type dipole process dielectric loss energy,

$[\epsilon_d''(\omega)]_{G_0} = [\epsilon_d''(\omega)]_{G_-}$ or $[\epsilon_d''(\omega)]_{G_0} = [\epsilon_d''(\omega)]_{G_+}$ or |

$[\epsilon_d''(\omega)]_{G_0} = [\epsilon_d''(\omega)]_{G_-} + [\epsilon_d''(\omega)]_{G_+}$

at the loss peak $\omega=1/\tau_{d'}$ we obtained slow and fast relaxation time with respect to primary relaxation time τ_D respectively as:

$$\tau_s^* = 1/\omega_s^* = \tau_D(c + \sqrt{c^2-1}), \ 0<g_d<1, \ \tau_s^*=\tau_D, \ g_d=1, \quad (18)$$

$$\tau_f^* = 1/\omega_f^* = \tau_D(c - \sqrt{c^2-1}), \ 0<g_d<1, \ \tau_f^*=\tau_D, \ g_d=1, \quad (19)$$

where $c=cot(g_d\pi/4)$ is the dielectric loss of $\mathbf{G_0}$ or $\mathbf{G_-}$ or $\mathbf{G_+}$ or $\mathbf{G_-}+\mathbf{G_+}$ at the loss peak $\omega=1/\tau_d$. The polarization relaxation for the Debye type dipole G_0 (dashed black) and fractional Debye type dipole G_- (red small dots g_d=0.6), G_+ (blue bigger dots, g_d=0.4) and G_-+G_+ (green thick line g_d=0.4, thin line g_d=0.6) dipoles (left panel) are shown in **Fig. 2**, based on Eqs. (9a)-(11a) respectively. The argument of Debye type dipole t/τ_D is shortened and lengthened by equal magnitudes above and below the Debye relaxation time in the fractional Debye type dipole representation by the exponents g_d and $(2-g_d)$. These arguments are represented as $(T/\Gamma)_{G_-}$ and $(T/\Gamma)_{G_+}$ in the fractional Debye type dipole polarization process. The shortened argument becomes $(T/\Gamma)_{G_-}$ stretched and lengthened argument $(T/\Gamma)_{G_+}$ becomes compressed in the Debye type exponential argument. These features are shown in Fig. 2, for g_d=0.6, and 0.4 as red dashed and blue dotted lines and green thick and thin lines are sum of fractional Debye type dipole polarization for g_d=0.6 and 0.4. Exactly similar features are observed in the frequency-domain dielectric response. The red arrow indicates Debye relaxation time (1s). The red dots indicate slow relaxation time τ_s^* and blue dots indicate fast relaxation time τ_f^* for g_d=0.6, and 0.4 respectively. These time scales are defined as NDR times due to the fractional Debye type dipole processes and it is dynamically correlated to the Debye type dipole relaxation time τ_D. The right panel shows NDR times τ_s^* and τ_f^* as function interaction strength g_d based on Eqs. (18) & (19).

The salient features of slow and fast relax on time scales are (a) the shift in Debye type relaxation time τ_D in equal magnitude on both side of Debye relaxation time (b) the magnitude of the shift in time scale depends on strength of fractional Debye type dipole in terms $0<g_d<1$, and smaller the magnitude $g_{d'}$ stronger is the interaction strength and larger is the shifts in slow and fast relaxation times. (c) In the frequency-domain, the slow and fast relaxation times belong to left side and right side of Debye loss peak respectively for given g_d and vice-versa in the

time-domain Debye type polarization. These are *novel* result on the relaxation dynamics of the proposed model.

When the dielectric loss spectra has more than one process loss peak contributions, like, high frequency loss peak β, in addition to low frequency loss peak α, then the similar fractional Debye type contribution process is considered for the loss peak β. If the dielectric loss spectra has 'n' number fractional Debye type dipole processes and if there is loss contribution due dc conductivity σ_{dc}, as observed in several glass forming alcohols, then the complex dielectric function and relaxation function become:

$$\epsilon_{GG}^*(\omega) = \sum_{m=1}^n ([\epsilon_d^*(\omega)]_{G_-} + [\epsilon_d^*(\omega)]_{G_+})_m + \sigma_{dc}/(i\omega\epsilon_0)$$

$$(20)$$

$$\phi_{GG}(t) \propto i_{GG}(t) \propto \sum_{m=1}^n ([\phi_d(t)]_{G_-} + [\phi_d(t)]_{G_+})_m \quad (21)$$

Here 'n' may be treated as number of subunit or subgroup or subunit of cluster of molecular level polarization processes contributing to the complex dielectric and polarization relaxation with their respective Debye type dipole and fractional Debye type dipole processes. In a nutshell, in a molecular level, for 'n' number of Debye type and their corresponding molecular level interaction initiated fractional Debye dipoles, the polarization mechanism and their dielectric function is found to be:

$$\left(\left(\frac{dP}{dT}\right)_{G_0,G_\pm} + \left(\frac{P}{\Gamma}\right)_{G_0,G_\pm}\right)_n = 0, \quad (22)$$

$$(P(T)_{G_0,G_\pm})_n \propto \left(exp\left[-\left(\frac{T}{\Gamma}\right)_{G_0,G_\pm}\right]\right)_n \quad (23)$$

$$([\epsilon_d^*(\omega)]_{G_0,G_\pm})_n \propto \left(\left(\frac{\Delta\varepsilon}{1+S\Gamma}\right)_{G_0,G_\pm}\right)_n, \quad (24)$$

where 'n' represents n number of unique NDR processes having n number of temporal and spatial scales due to the n number of Debye type dipole and their respective fractional Debye type polarization relaxation processes.

The relaxation time of glass formers shows a deviation from Arrhenius law and it is parameterized with Vogel-Fulcher-Tamman (VFT) equation [21]:

$$(\tau_d)_n=(\tau_0exp(A_0T_0/(T-T_0)))_{n'} \qquad \text{for } T > T_{g'} \quad (25)$$

where n=1, 2, ..., T_0 is the VFT approximation of the ideal glass transition temperature, A_0 is the strength

parameter, τ_0 is a pre-factor of the order inverse phonon frequency and further characterized based on fragility index [21],

$$m_p = log_{10}(e)(A_0(T_0/T_g)(1-T_0/T_g)^{-2})_{n'} \qquad (26)$$

where Arrhenius equation is

$$(\tau_d)_n = (\tau_0 exp(E_a/k_B T))_{n'} \qquad (27)$$

with E_α is activation energy. The relaxation parameters resulting from the fits are shown and the relaxation times are checked for Arrhenius or Vogel–Fulcher–Tammann (VFT) behavior.

3.7 Comparison with existing non-Debye relaxation

In **Fig. 3**, in the left panel, the existing NDR functions KWW (numerical Fourier transform for β_{KWW}=0.6), CC, CD, HN, UDR and proposed GG function are shown in double logarithmic plots. The empirical form of CC dielectric function has a slope $(1-\alpha_{CC})$ below the loss peak and $-(1-\alpha_{CC})$ above the loss peak and loss curve is symmetric about the loss peak.
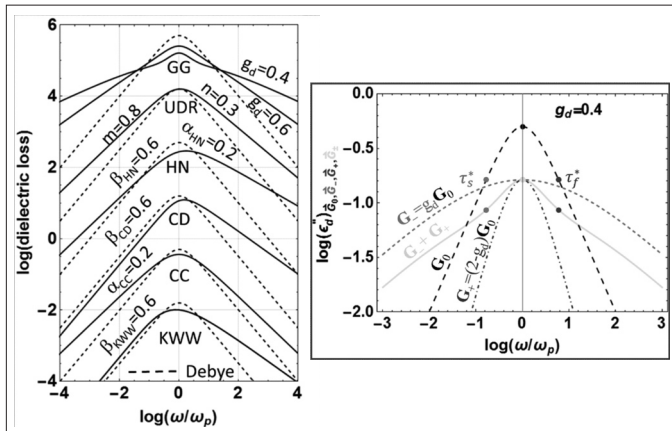

Fig. 3: In the left panel, a comparison of frequency domain double logarithm plots of proposed unique NDR function (n=1) with existing NDR functions KWW (numerical Fourier transform for β_{KWW}=0.6), CC, CD, HN, and UDR. The slope of lines to which peaks is asymptotic. Plots are vertically separated by 1.5 units for clarity. The dashed line is Debye type dielectric loss. The right panel shows further details of proposed dielectric loss contribution for Debye type dipole G_0 and the fractional Debye type dipoles G_-, G_+ and their sum G_-+G_+. The slopes varies from g_d to 2-g_d on left side of the loss peak and -g_d to -(2-g_d) on right side of the loss peak The red and blue dots on the lines show the slow and fast relaxation times for g_d=0.4.

The fractional exponent $(1-\alpha_{CC})$ is explained in terms equivalent circuit with impedance polarization "denoting the storage of energy in addition to dissipation energy in the mechanism of molecular interaction responsible for dispersion". The empirical function CD accounts for asymmetry in the dielectric loss observed several glass forming alcohols, however, the exponent β_{CD} is physically

uninterpreted quantity and slope of the dielectric loss below the loss peak is always one and above loss peak is $-\beta_{CD}$. The HN dielectric function was suggested when the slopes are different on both sides of dielectric loss peak, HN exponents $(1-\alpha_{HN})$ and β_{HN} are physically uninterpreted quantities. However, the exponents of KWW, CC, CD and HN are used to describe distribution relaxation in NDR process. In Jonscher's UDR, the exponents 0<m<1 and 0<n<1 change the slopes of the dielectric loss curve asymmetrically with respect to loss peak having sum of two processes with exponents m and n. The energy criterion has been given for process involving only the exponent n and it is tentatively modeled in terms of partial screening mechanism. The time domain polarization functions for these existing empirical form of NDR are still a mystery, however, power laws and KWW function are approximated as possible polarization functions. It is clear from left panel of Fig. 3, the slop of proposed GG dielectric function in double logarithmic plots have completely different features when compared with existing empirical form of dielectric functions. The dielectric loss slope of sum of fractional Debye type dipole process varies between g_d to 2-g_d below and above the loss peak and also depends on dielectric strength $(\Delta\epsilon)_{G_\pm}$. On the right panel in Fig. 3, Debye type dipole dielectric loss and fractional Debye type dielectric loss for g_d=0.4 are shown with Debye relaxation time (1s). The magnitudes of slow and fast relaxation times are 5.99 and 0.167(s) respectively and these shown as red and blue dots on the lines for g_d=0.4.

4. Dielectric loss data analysis

4.1 *1*-Cyanoadamantane

The dielectric loss data of *1*-cyanoadamantane ($C_{10}H_{15}CN$, *1*-CNA) are taken from Lunkenheimer's research group [22,23]. *1*-CNA is a simple prototypical plastic crystal with carbon atoms form a cage, the free bonds being saturated by hydrogen atoms and one cyano-group. Below the melting temperature (T_m=458 K) the plastic phase is formed and at *T*=280 K orientational order occurs. The dielectric loss data and schematic view of molecular structure as insets are shown on the top panel in **Fig. 4** for the plastic-crystalline phase of *1*-CNA. The data are shown as black dots. The data analysis covered on the plastic-crystalline phase having wide measured frequency range up to 20 GHz. Lunkenheimer's research group have performed numerical Fourier transform of KWW function for the temperature dependent data of loss data of *1*-CNA and found worse fit and hence they rejected KWW method. Further, the *1*-CNA loss data were analyzed using empirical form of CD dielectric functions. For all the temperatures, the loss data did not fit well around two decades at high frequency region.
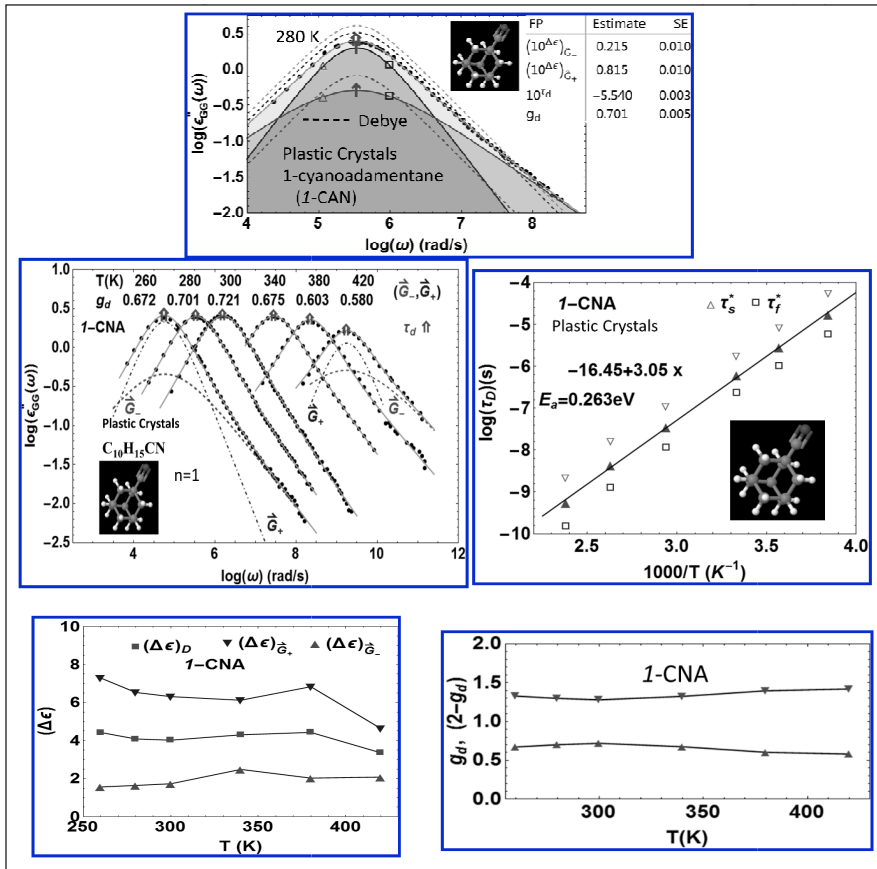
Fig. 4: Fit results of dielectric loss of a simple van der Waals system plastic crystal 1-cyanoadamentane (1-CNA) for T=280K shown on the top panel, where number of subunits of molecular process n contributed to dielectric loss is 1. The dashed red and blue lines are Debye type dipole dielectric loss G_0 and continuous red and blue lines and shades are fractional Debye type dipole G_- and G_+ dielectric loss and green line and shade is sum of dipoles $G_- + G_+$ dielectric loss. The estimates of fit parameters (FP) and standard error (SE) are shown as an attachment. The panel in the middle shows temperature dependent loss data of 1-CNA with interaction strength g_d. The G_- and G_+ dipole dielectric loss contributions are shown for T=260K and 420K. The double headed arrow indicates primary relaxation time. Arrhenius type temperature dependence Debye type relaxation time, slow and fast relaxation times are shown in right side of middle panel. The bottom panel shows dielectric strength and interaction strength as function of temperatures.

The fit result based on Eq. (20) is shown in Fig. 4 for *1*-CNA loss data, where $\sigma_{dc}=0$, and n is found to be one. The estimate of fit parameters (FP) and standard errors (SE) attached in Fig. 4 of to panel. With simple orientational order, the Debye type dipole $\mathbf{G}_0$ and the interaction originated fractional Debye type dipoles $\mathbf{G}_- = g_d\mathbf{G}_0$ and $\mathbf{G}_+ = (2-g_d)\mathbf{G}_0$, with $g_d=0.701$ and their respective dielectric strength shows excellent fitting. During the molecular motion, the instantaneous transfer of Debye type dipole of $\mathbf{G}_0$ of *1*-CNA molecule is incomplete by a factor $(1-g_d)$ $\mathbf{G}_0$, and hence the fractional Debye type dipoles $\mathbf{G}_-$ and $\mathbf{G}_+$ relaxation process initiated and fractional Debye type dipole takes over and resulting a spread in Debye type dipole dielectric spectra as shown in Fig. 4. The Debye type dipole are shown as dashed lines and the continuous lines and shades are fractional Debye type dipole relaxation process where $0 < g_d < 1$.

In Fig. 4, the middle panel, the temperature dependence data are further analyzed for wide range of frequency and temperature dependent dielectric loss peaks are shown in form of Arrhenius plot. The straight line fit equation, slope and attempt frequency $1/\tau_0$ are indicated in Fig. 4. The slow and fast relaxation times are shown with Debye type relaxation time. The bottom panel in Fig. 4 shows dielectric strengths $(\Delta\epsilon)_{G_+}$ and interaction strength g_d as a function of temperature. The proposed model shows excellent fit for the entire region of frequency and provides new physical insight for the molecular motion in terms dipole-dipole interaction with the concept of Debye type and fractional Debye type dipole polarization.

4.2 Dielectric loss data analysis of super-cooled glycerol

The dielectric loss data of super-cooled glycerol $(C_3H_5(OH)_3)$ are taken from Lunkenheimer's research group [24]. The dielectric spectra and schematic view of molecular structure as insets are shown in Fig. 5 for the super-cooled phase of glycerol on the top panel to demonstrate the typical analysis of dielectric loss data based on Eq. (20). The glass transition temperature of glycerol T_g is 184K. In glycerol system $\sigma_{dc}=0$, and the number of subunits n contributing to the dielectric loss is found to be 2. One of the challenging problems in the dielectric loss spectra is the excess wing in some of the glass forming systems and it is a common-feature without well resolved β relaxation. Lunkenheimer's research group performed high precision aging experiments lasting up to five weeks, and they have shown the equilibrium spectra below T_g, showing up excess wing (long tail above the α peak) as a second power law at high frequencies, developed into a shoulder. Their results strongly suggested that the excess wing, observed in a variety of glass formers, is the high-frequency flank of a β relaxation.

In the present work, we have analyzed the dielectric loss spectra of glass-forming glycerol at temperature above and below T_g based on the proposed model. Typical result
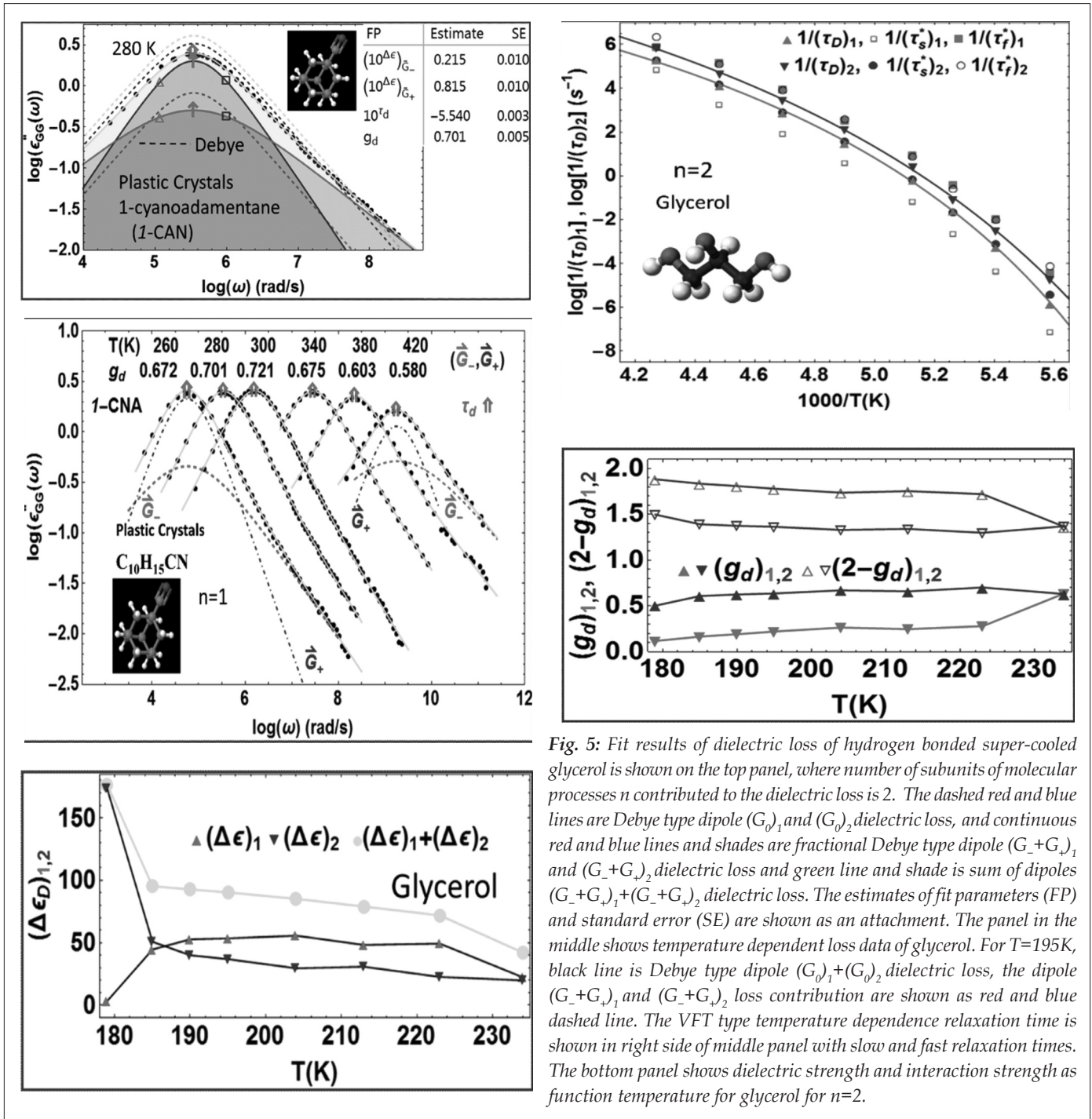
Fig. 5: *Fit results of dielectric loss of hydrogen bonded super-cooled glycerol is shown on the top panel, where number of subunits of molecular processes n contributed to the dielectric loss is 2. The dashed red and blue lines are Debye type dipole $(G_0)_1$ and $(G_0)_2$ dielectric loss, and continuous red and blue lines and shades are fractional Debye type dipole $(G_- + G_+)_1$ and $(G_- + G_+)_2$ dielectric loss and green line and shade is sum of dipoles $(G_- + G_+)_1 + (G_- + G_+)_2$ dielectric loss. The estimates of fit parameters (FP) and standard error (SE) are shown as an attachment. The panel in the middle shows temperature dependent loss data of glycerol. For T=195K, black line is Debye type dipole $(G_0)_1 + (G_0)_2$ dielectric loss, the dipole $(G_- + G_+)_1$ and $(G_- + G_+)_2$ loss contribution are shown as red and blue dashed line. The VFT type temperature dependence relaxation time is shown in right side of middle panel with slow and fast relaxation times. The bottom panel shows dielectric strength and interaction strength as function temperature for glycerol for n=2.*

of dielectric loss data of glycerol at 204K is shown in Fig. 5. The number of subunits n=2 is obtained for the dielectric loss data analysis and estimates of fit parameters (FP) and their standard errors (SE) are attached in Fig.5. Excellent fit parameters and fits are obtained for n=2, where there are two closely spaced times scales of motions are observed as two different Debye type dipole moments $(G_0)_1$ and $(G_0)_2$ with their corresponding fractional Debye type dipole moments $(g_d G_0)_1$ and $((2-g_d)G_0)_1$, $(g_d G_0)_2$ and $((2-g_d)G_0)_2$ where dipole-dipole interaction strengths are $(g_d)_1$=0.264

and $(g_d)_2$=0.670 and two different Debye type relaxation times are $(\tau_d)_1$=2.35x10^{-2}(s), $(\tau_d)_2$=7.94x10^{-3}(s). Both Debye type dipoles and fractional Debye type dipoles and their sums are shown as dashed lines and continuous lies. The proposed model predicts the existence of mysterious high frequency flank of a α relaxation, though it is not well resolved in the dielectric loss data explicitly.

Similar fitting procedure is followed for other temperatures [24] and result are reported in the middle panel of Fig. 5. The double arrow around loss peak indicates

position of relaxation time $(\tau_d)_1$ and $(\tau_d)_2$. The temperature dependence of $(\tau_d)_1$ and $(\tau_d)_2$ shows VFT features and the VFT fit parameters and fragility are obtained based on Eqs. (25)-(26) as:

$(\tau_0)_1 = 10^{-12.84 \pm 0.48}$, $(A_0)_1 = 11.64 \pm 1.09$, $(T_0)_1 = 140.79 \pm 2.12$, and the fragility $(m_p)_1 = 70.2$,

$(\tau_0)_2 = 10^{-14.53 \pm 0.54}$, $(A_0)_2 = 15.16 \pm 1.51$, $(T_0)_2 = 133.42 \pm 2.54$, and the fragility $(m_p)_2 = 63.2$.

The dielectric strength and interaction strength obtained based of fit results of dielectric loss data are shown in bottom panel in Fig.5 for n=1, and 2. The interaction strength for the subunit n=1 of the molecular process is found to be much stronger than n=2, and hence the excess wing or long tail in the dielectric loss is due the slow α process and it is clearly shown in Fig. 5, for T=195 as red dashed line in middle left panel. Figure 6 shows the compiled dielectric loss data of ten different molecular systems based on proposed model at different temperatures. These data were collected from literature and analysed based on the proposed dielectric Eq. (20) and results are shown in Fig. 6. The list below shows dielectric system, temperature in Kelvin, reference, number of
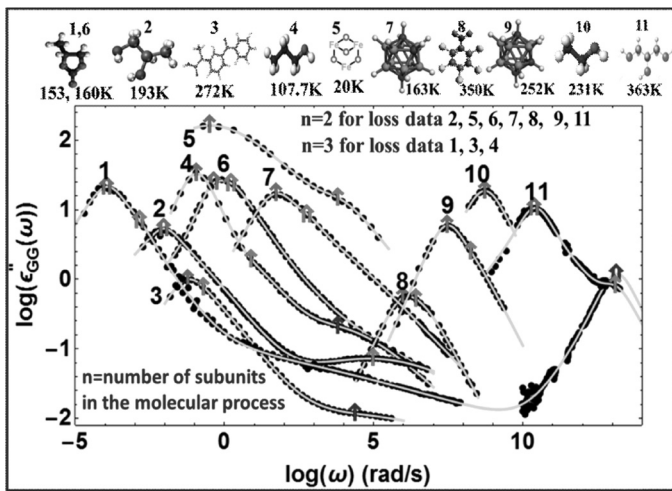
subunits n associated with molecular process contributing to dielectric loss, interaction strength and type of relaxation process:

(1) *Propylene carbonate*@153 [25], $(G_\pm)_1 + (G_\pm)_2 + (G_\pm)_3$, $(g_d)_1 = 0.674$, $(g_d)_2 = 0.132$, $(g_d)_3 = 0.654$, α, β and Boson peak (three pairs of $(G_\pm)$ loss show fifteen decades of frequency dependence!);

(2) *TriPGG*@193 [26], $(G_\pm)_1 + (G_-)_2$, $(g_d)_1 = 0.549$, $(g_d)_2 = 0.277$, α and β;

(3) *Ketoprofen*@272 [13], $(G_-)_1 + (G_-)_2 + (G_-)_3$, $(g_d)_1 = 0.631$, $(g_d)_2 = 0.893$, $(g_d)_3 = 0.204$, α, β and γ;

(4) *1-propanol*@107.7 [27], $(G_-)_1 + (G_-)_2 + (G_-)_3$, $(g_d)_1 = 0.997$, $(g_d)_2 = 0.617$, $(g_d)_3 = 0.411$, Debye, α and β;

(5) *Magnatite*@20 [28], $(G_-)_1 + (G_-)_2$, $(g_d)_1 = 0.433$, $(g_d)_2 = 0.698$, α and β. The real part of $\epsilon_{GG}^*(\omega)$ is shown as filled plot based on Eqs. (18) & (19).

(6) *Propylene carbonate*@160 [24], $(G_\pm)_1 + (G_\pm)_2$, $(g_d)_1 = 0.235$, $(g_d)_2 = 0.667$, α and β;

(7) *Ortho-carborane*@163 (*o*-CA) [23], $(G_-)_1 + (G_\pm)_2$, $(g_d)_1 = 0.882$, $(g_d)_2 = 0.450$, α and β;

(8) *Pentachlornitrobenzene*@350 [23] $(g_d)_1 = 1.0$, $(g_d)_2 = 0.805$, α and β;

(9) *Meta-carborane*@252 (*m*-CA) [23], $(G_-)_1 + (G_-)_2$, $(g_d)_1 = 1.0$, $(g_d)_2 = 0.787$, α and β;

(10) *Ethanol*@231 [29], $(G_-)_1$, $(g_d)_1 = 0.943$, α;

(11) *Glycerol*@363 [25], $(G_\pm)_1 + (G_-)_2$, $(g_d)_1 = 0.557$, $(g_d)_2 = 1.0$, α and β.

5. Summary and conclusions

The existing time-honoured NDR functions with their exponents, β_{KWW}, α_{CC}, β_{CD}, (α_{HN}, β_{HN}) and (m, n) were introduced 163, 76, 66, 50, and 43 years ago respectively. Still their use in dielectric loss analysis is piecemeal approach tailored to individual materials and often highly arbitrary. The proposed Eqs. (20)-(24) have polarization relaxation dynamics of Debye type dipole G_0 and fractional Debye type dipoles $\pm G$, and $G_\pm$, where $\pm G = (1-g_d)G_0$, $G_- = G_0 - (1-g_d)G_0 = g_d G_0$, $G_+ = G_0 + (1-g_d)G_0 = (2-g_d)G_0$ and these dipoles will open a window on one of Nature's best-kept secrets of NDR. The proposed model will heighten the understanding of NDR and physical insight for the dielectric loss of α, β and γ relaxations, excess wing, and closely related ac conductivity and mechanical relaxation. Hopefully, the proposed fractional Debye type model will be able to unify and encompass the existing NDR approach with an amendments. The universal Debye type dipole relaxation and its associated fractional Debye type dipole relaxation dynamics with redistribution and

Fig. 6: *A compilation of dielectric loss data range of ten materials is shown covering frequency range of 15 decades. The schematic structure of these molecules with serial numbers and temperature of loss data are shown. (1) Propylene carbonate@153 (2) TriPGG (3) Ketoprofen (4) 1-propanol (5) Magnatite (6) Propylene carbonate@160 (7) Ortho-carborane (8) Pentachloro-nitrobenzene (9) Meta-carborane (10) Ethanol (11) Glycerol. For each molecular system the number of subunits n of molecular processes contributing to the dielectric loss is indicated. The double headed arrow indicates dielectric loss contribution from both G_- and G_+, and single headed arrow indicates dielectric loss contribution from either G_- or G_+. Among G_- and G_+ the dielectric loss contributions, with respect to temperature variation, the dominant contribution is found to be G_- as shown in Langevin function Fig. 1.*

conservation of moment and energy in the storage and dissipation processes in the dielectric response are too striking and believed that one underlying principle of "molecular level many-body interactions between its constituent parts" governs the response of condensed matter to electromagnetic fields.

Acknowledgements

References

1. K. L. Ngai, *Relaxation and Diffusion in Complex Systems,* Springer: New York, 2011.

2. Jonscher, A. K. *Dielectric Relaxation*, Chelsea Dielectric Press, London, 1983.

3. K. S. Cole, R. H. Cole, *J. Chem. Phys.,* **1941**, 9, 341.

4. R. Murugaraj, G. Govindaraj, Solid State Ionics, **2005**, 176, 109.

5. N.S.K.Kumar, T.S. Shahid, G. Govindaraj, *Physica B: Condensed Matter*, **2016**, 488, 99.

6. D. W. Davidson, R.H. Cole, *J. Chem. Phys.,* **1951**,19, 1484.

7. S. Havriliak, S.A. Negami, *Polymer,* **1967**, 8, 161.

8. R. Kohlrausch, *Ann. Phys.* (Leipzig), **1854**, 167, 179.

9. G. Williams, D.C.Watts, *Trans. Faraday Soc.*, **1970**, 66, 80.

10. A. K. Jonscher, *Nature,* **1977**, 267, 191.

11. Lakshmi Vijayan, G. Govindaraj, *Journal of Physics and Chemistry of Solids,* **2011**, 72, 613.

12. Rajesh Cheruku, G. Govindaraj, Lakshmi Vijayan, *Materials Chemistry and Physics*, **2014**, 146, 389.

13. U. Sailaja, M. Shahin Thayyil, N.S. Krishna Kumar, G. Govindaraj, *European Journal of Pharmaceutical Sciences*, **2013**, 49, 333.

14. U.Sailaja, M.Shahin Thayyil, N.S.Krishna Kumar, G. Govindaraj, *Journal of Pharmaceutical Analysis,* **2016**, 6, 165.

15. U.Sailaja, M.Shahin Thayyil, N.S.Krishna Kumar, G. Govindaraj, K.L. Ngai, European Journal of Pharmaceutical Sciences, **2017**, 99, 147.

16. J.C. Dyre, J. Non-Cryst. Solids, **1991**, 135, 219.

17. J.C. Dyre, J. Appl. Phys., **1988**, 64, 2456.

18. R. Murugaraj, G. Govindaraj, Deepa George, Materials Letters, **2003**, 57, 1656.

19. G. Govindaraj, *AIP Conference Proceedings,* **2016**, 1731, 070025.

20. G. Govindaraj, **2016**, *arXiv:1608.05304*.

21. C. A. Angell, *Science*, **1995**, 267, 1924.

22. R. Brand, P. Lunkenheimer, U. Schneider, A. Loidl, *Phys. Rev. Lett.*, **1999** 82, 1951.

23. R. Brand, P. Lunkenheimer, A. Loidl, *J. Chem. Phys.*, **2002**, 116, 10386.

24. U. Schneider, R. Brand, P. Lunkenheimer, A. Loidl, Phys. Rev. Lett., **2000**, 84, 5560.

25. P. Lunkenheimer, U. Schneider, R. Brand, A. Loidl, *Contemporary Physics*, **2000**, 41, 15.

26. R. Casalini, C. M. Roland, *Phys. Rev. Lett.*, **2003**, 91, 15702.

27. P. Power, G. P. Johari, J. K. Vij, *J. Chem. Phys.*, **2002**,116, 4192.

28. F.Schrettle, F. S. Krohns, P. Lunkenheimer, V.A.M. Brabers, A. Loidl, *Phys. Rev. B.* **2011**, 83, 195109.

29. R. Brand, P. Lunkenheimer, P. U. Schneider, A. Loidl, *Phys. Rev. B.*, **2000**, 62, 8878.

G. Govindaraj, *received his Ph. D. from the University of Madras in 1987, after his M.Sc. Applied Sciences from PSG college of Technology in 1980. From 1988 to till date he has been working as faculty member in the Department of Physics, Pondicherry University (a central University). He has been working as Professor from 2002 onwards and at present he is a Dean, School of Physical, Chemical Applied Sciences, Pondicherry University. His research area is focussed on the subject of ac conductivity and dielectric relaxation. His current research areas interests are relaxation phenomena in glass-forming liquids, plastic crystals, polymers and electron/ion hopping conduction in condensed matter systems. On these subjects, he has completed 13 research projects, 6 PhDs were awarded under his guidance and published around 110 research papers in national, international journals and proceedings. He is instrumental for developing several major sophisticated analytical facilities including NavoControl Broadband Dielectric Spectrometer covering 3□Hz to 3GHz with temperature range 77K to 1100K for advanced research in Pondicherry University. He has visited number of countries like Poland, Italy, France, Germany, Japan, China, Africa, Singapore, Malaysia etc. for postdoctoral work and for international seminar/conference. He has become a Fellow of Academy Sciences, Chennai.*

SOCIETY FOR MATERIALS CHEMISTRY (SMC)
(Reg. No. - Maharashtra, Mumbai/1229/2008/GBBSD)
c/o Chemistry Division
Bhabha Atomic Research Centre, Mumbai 400 085

APPLICATION FOR MEMBERSHIP

Please enroll me as a Life member of the *Society for Materials Chemistry* (**SMC**). My particulars are as follows:

Name   :_____

Educational Qualifications   :_____

Field of Specialization   :_____

_____

Official Address   :_____

_____

Telephone No. (Off.)   :_____

Residential Address   :_____

_____

Telephone No. (Res.)   :_____

Address for Correspondence   :   Home/Office   (Please tick one of the options)

E-mail Address   :_____

Subscription Details
Mode of Payment   : Cheque/DD/Cash
                                  (Cheque/DD should be drawn in favor of "*Society for Materials Chemistry*" for Rs. 1000/- payable at Mumbai. For out-station *non-multi-city* cheques, please include Rs.50/- as additional charge for bank clearance.

Number   :
Dated   :
Drawn on Bank & Branch   :
Amount   :
Place:
Date: Signature

_____

Registration Number: _____   (To be allotted by SMC office)

In this issue